MR169 FR-890

FINAL REPORT

PARTICULATE EMISSIONS, PLUME RISE, AND DIFFUSION FROM A TALL STACK VOLUME 1. TECHNICAL REPORT

by

Brand L. Niemann

Margaret C. Day

Paul B. MacCready, Jr.

to

Meteorology Division
National Air Pollution Control Administration
U. S. Department of Health, Education, and Welfare
Durham, N. C.
Contract CPA 22-69-20

Meteorology Research, Inc.
464 West Woodbury Road
Altadena, California 91001

January 1970

Final Report

on

PARTICULATE EMISSIONS, PLUME RISE, AND DIFFUSION FROM A TALL STACK

VOLUME I. TECHNICAL REPORT

to

Meteorology Division
National Air Pollution Control Administration
U. S. Department of Health, Education, and Welfare
Durham, N. C.

Contract CPA 22-69-20

by

Brand L. Niemann
Margaret C. Day
Paul B. MacCready, Jr.

Meteorology Research, Inc.
464 West Woodbury Road
Altadena, California 91001

January 1970

MRI69 FR-890

FOREWORD

The work was carried out as part of the Large Power Plant Effluent Study (LAPPES) conducted by the National Air Pollution Control Administration. Sponsorship was by NAPCA under Contract CPA 22-69-20 and modifications.

We wish to acknowledge the help of NAPCA personnel in carrying out this program, specifically Mr. Frank Schiermeier, LAPPES Field Manager, and Mr. Larry Niemeyer and Mr. Charles Hosler of the Division of Meteorology.

Many MRI personnel have been involved in the work, in addition to the primary authors. Dr. Theodore B. Smith contributed to the evaluation and writeup. Mr. Robin Williamson was in charge of the flight operations and served as pilot. Mr. Alan Miller was flight observer and handled the instrumentation. Mr. David Leavengood was field project manager. Mrs. Ruby Wen and Mr. Gary Korell were responsible for the computer programming. Mr. William Green was very helpful in the particle analysis, as was Dr. Betty Behl.

SUMMARY

The primary MRI field role on the LAPPES I experiment at the Keystone Power Plant in Pennsylvania, October 1968, was to make airborne measurements of the environment and of plume characteristics. The special measurements were those of turbulence, taken with a Universal Indicated Turbulence System (UITS) and particles collected with a Moving Slide Impactor. In addition to the aircraft flights, MRI made sequential photographs of the plume from a camera on the ground.

The resulting data have been reduced and are presented in computer printout and computer plots in two extensive companion volumes. The data reduction techniques are described here, and samples of the data are given.

This volume also contains a brief evaluation of much of the data. The results of the particulate measurements are somewhat ambiguous. The environmental variability was large, and tended to obscure the superimposed plume characteristics. A scanning electron beam microscope gave the most definitive results.

The aircraft-derived data and photogrammetric data on plume rise and diffusion have been evaluated with two main aims in mind: (1) to ascertain the usefulness of the turbulence system for diffusion studies, and (2) to compare the observations with standard plume rise and diffusion theory. It must be recognized that on this brief and limited field program it was not possible to develop and apply rigorous techniques throughout and so the conclusions cannot be based on the desired statistical significance.

The UITS was very useful in delineating the height of the layer throughout which the environmental mixing would eventually spread the plume. This height was sometimes appreciably greater than might have been inferred merely from noting stable regimes from temperature soundings. The plume would usually rise still higher from its own buoyancy and momentum. The plume diffusion even into the area of fumigation appeared dominated by its own initial turbulent energy, rather than by environmental turbulence. The aircraft flights did not provide data in this early stage of plume growth, so there was no opportunity to relate this diffusion quantitatively to theory. For subsequent regions, the aircraft UITS data were evaluated to give effective vertical exchange coefficients by the technique of relating the exchange coefficient to the observed small-scale energy multiplied by the four-thirds power of a dominant eddy scale. On the cases available for photogrammetric evaluation in this fumigation region, which started at a

distance of about 1 km, the cloud generally filled the mixing layer and so rate information could not be ascertained for comparison with the exchange coefficients. The UITS data were also used to estimate surface shear and roughness; the technique shows promise, but requires the use of flight trajectories established specifically for this purpose if statistical significance is to be obtained.

The aircraft and photogrammetric data on plume rise were compared with standard prediction methods. It was found that the plume rise followed a power law with an exponent somewhat less than the 0.67 often suggested. The observations were fitted to a ground concentration prediction equation, and the resulting predictions of SO_2 concentration at the ground were compared with observations. The data available on this program were not suitable for quantitative study of the lateral spread of the cloud.

TABLE OF CONTENTS

LIST OF ILLUSTRATIONS

LIST OF ILLUSTRATIONS (continued)

I. INTRODUCTION

NAPCA has a strong interest in studying the usefulness of large stacks for minimizing high pollution levels. The Large Power Plant Effluent Study (LAPPES) is a coordinated program involving NAPCA personnel and contractors to study the subject, using for experimental purposes the plume from the 245-meter high stack at the Keystone Generating Station in western Pennsylvania. The particular goal of the program is to refine and verify the predictive models used to estimate pollutant concentrations from such high stacks. Present models have been tailored to data primarily from much lower stacks, and where complex terrain effects are not dominant. Thus one does not yet have sufficient background in prediction of concentrations from high stacks, especially in complex terrain, to have the desired confidence when justifying their great expense.

In 1968, the LAPPES program involved two field experimental periods. The MRI participation was during the second of these, October 15-24. The primary MRI field role was to make airborne measurements of the environment and of plume characteristics. One special measurement was of particles in the plume, to ascertain something about the concentration and size distribution for comparison with the concurrent lidar observations being conducted by SRI. The main other special measurement was of the turbulence intensity, within and outside of the plume, using the UITS (Universal Indicated Turbulence System). This gives a measure of ϵ, the turbulent energy dissipation rate, and the energy in the small-scale turbulent eddies; ϵ is an important input into certain forms of diffusion evaluations. There was very little time to prepare for the MRI field measurements, because of lateness of the start of the contract and due to prior commitments on the use of the airplane elsewhere immediately preceding the LAPPES operation. Nevertheless, on the whole the airborne measurements yielded useful data. The most significant problem was that the particle evaluations could not be made definitive with the techniques then available for data acquisition and evaluation. A scanning beam electron microscope became available only late in the program; it proved to be very helpful. Questions remain as to the size distributions and concentrations of the plume particles.

In addition to the aircraft observations, MRI operated a ground camera sequentially photographing the plumes from the side. These pictures have been reduced to provide plots of plume sizes and position for comparison with theoretical predictions of plume rise, and for comparison of the usefulness of the photographic technique with the lidar method. The MRI role also included a brief assessment of the applicability of various theories to these experimental data.

The SRI lidar study has already been reported on completely by Johnson and Uthe (1969). The Sign-X Laboratory results have been presented by Proudfit (1969). The total MRI report consists of three volumes. This one, Volume I, presents evaluations and summaries of the data. Volumes II and III are extensive data supplements, available in only limited supply from NAPCA or MRI. Volume II contains summary listings, codes, and maps, and then for each program day:

ESSA Weather Map
Selected Tracings of Plume Photographs and True Plume Profiles
Pibal Wind Profile Plots
MRI Aircraft Flight Track Maps
MRI Aircraft Data Plots

Volume III contains computer listings of aircraft data and smoke plume photogrammetry data.

II. FIELD PROGRAM DESIGN AND INSTRUMENTATION

The Overall Program

The October 1968 coordinated field observational program at the Keystone Electric Generating Plant, designated LAPPES I, involved personnel and equipment from NAPCA, SRI, Sign-X, and MRI. A brief summary of the total data-taking plan is given below:

Plant Engineer:

Hourly readings of plant parameters for calculation of (1) exit velocity, (2) heat emission, (3) SO_2 source strength, and (4) fly ash quantity and composition.

Meteorologists:

- Pilot balloon launch every 30 minutes, double theodolite tracking. Position read every 30 seconds.
- Continuous ground level recordings of temperature, barometric pressure, and relative humidity.
- Rabal sounding at airport at noon each test day.

Airborne Activities:

- Helicopter-mounted SO_2 sensor.
- MRI instrumented aircraft
  1. Universal Turbulence Indicator
  2. Moving Slide Impactor (samples particles up to 10 μm)
  3. Continuous Particle Collector (samples particles larger than 10 μm)
  4. Nephelometer (measures total light scattering of airborne particles and aerosols)
  5. Stationary nose-mount of 16 mm time-lapse camera set for exposure every 2 seconds
  6. 12-channel Brush oscillograph chart recorder for the following parameters:

digital clock time	heading
airspeed	temperature
altitude	ϵ (turbulence)

  7. Meteorologist-observer with voice recorder.

Ground Activities:

1. Stanford Research, Inc., van-mounted lidar (laser radar) recording plume cross sections.

2. 35-mm single camera color photos from ground sites nearly normal to plume path taken at 2-minute intervals.

Unfortunately, an electronic malfunction developed in the Nephelometer during its operation on the way to the site from California, and there was insufficient time to rectify the problem in the field. The lack of this device hampered the program by prohibiting us from making direct light scattering measurements for comparison with lidar backscattering, and by making it more difficult to delineate plume edges and cross-section characteristics.

Data on the MRI ground photography are given in Appendix A.

The MRI flights with the instrumented Aztec C are summarized in Table I. Appendix B goes into further detail, showing how the 110 distinct data acquisition portions of the flights are put into coded categories. Appendix C further explains the run labeling system and gives data on altitudes and turbulence.

The program was scheduled to take place in the fall to take advantage of the extreme stability that occurs during a stagnant high in that area at that time of the year. All trials were conducted from 15 to 22 October 1968.

Plant Description

A map showing the topography and locations in the Keystone vicinity is presented in Volume II. The topography around Keystone appears on maps comprising Figs. 2 through 8 in Appendix A of this report.

The Keystone Power Station is 10 miles WNW of Indiana, Pennsylvania. Its base is at 1010 ft MSL. The two adjacent tall stacks are 800 ft high, or 1810 ft MSL at the top. The two evaporative cooling towers which were in operation are 325 ft high. They are about 700 ft E of the tall stacks. The surrounding terrain is gently rolling farmland with trees and fields. Homer City Power Station is 8-1/2 miles S of Indiana. Ground elevation at its base is 1280 ft MSL with 800-ft high stacks. It is located on a hilltop with woods and fields surrounding it. The Conemaugh Power Station is 17 miles SSE of Indiana. Its base is at 1050 ft MSL in the narrow river valley of the Conemaugh River, with its stacks towering 1200 ft above ground. This valley runs roughly E-W at this point and the valley walls extend to over 2000 ft MSL. The local headquarters of the MRI operation were at Jimmy Stewart Airport just E of Indiana.

Table I

MRI DATA COLLECTING FLIGHTS

Date	Flight No. by Day	Flight of Entire Project		A/C Strip Charts Available
15 Oct 68	1	1	CPC and MSI Particle Collecting Flight	X
16 Oct 68	1	2	CPC and MSI Particle Collecting Flight	X
17 Oct 68	1	3	CPC and MSI Particle Collecting Flight, some rain	X
17 Oct 68	2	4	CPC and MSI Particle Collecting Flight, SRI cooperate	X
18 Oct 68	1	5	CPC and MSI Particle Collecting Flight, SRI cooperate	
	2	6	CPC and MSI Particle Collecting Flight, SRI cooperate	
20 Oct 68	1	7	Turbulence and Temperature Flight, CPC only	X
20 Oct 68	2	8	Field Mill and Turbulence Flight	
20 Oct 68	3	9	Field Mill and Turbulence Flight	
21 Oct 68	1	10	CPC and MSI Particle Collecting Flight, SRI cooperate	X
21 Oct 68	2	11	Turbulence run only	X
22 Oct 68	1	12	CPC and MSI Particle Collecting Flight, SRI cooperate	X
22 Oct 68	2	13	CPC and MSI Particle Collecting Flight, SRI cooperate	X

Aircraft and Its Instrumentation

Figure 1 shows the instrumented Aztec. This supercharged airplane has been used primarily in cloud physics studies. Such studies require particulate collections and turbulence measurements, which are important factors in air pollution work. Thus this aircraft which had just come from a cloud physics field program was ready, with slight modification, for the LAPPES program.

The main variables recorded on the Brush oscillograph were air temperature, pressure altitude, compass heading, turbulence intensity (UITS), plus timing marks and special event marks. The observer-operator

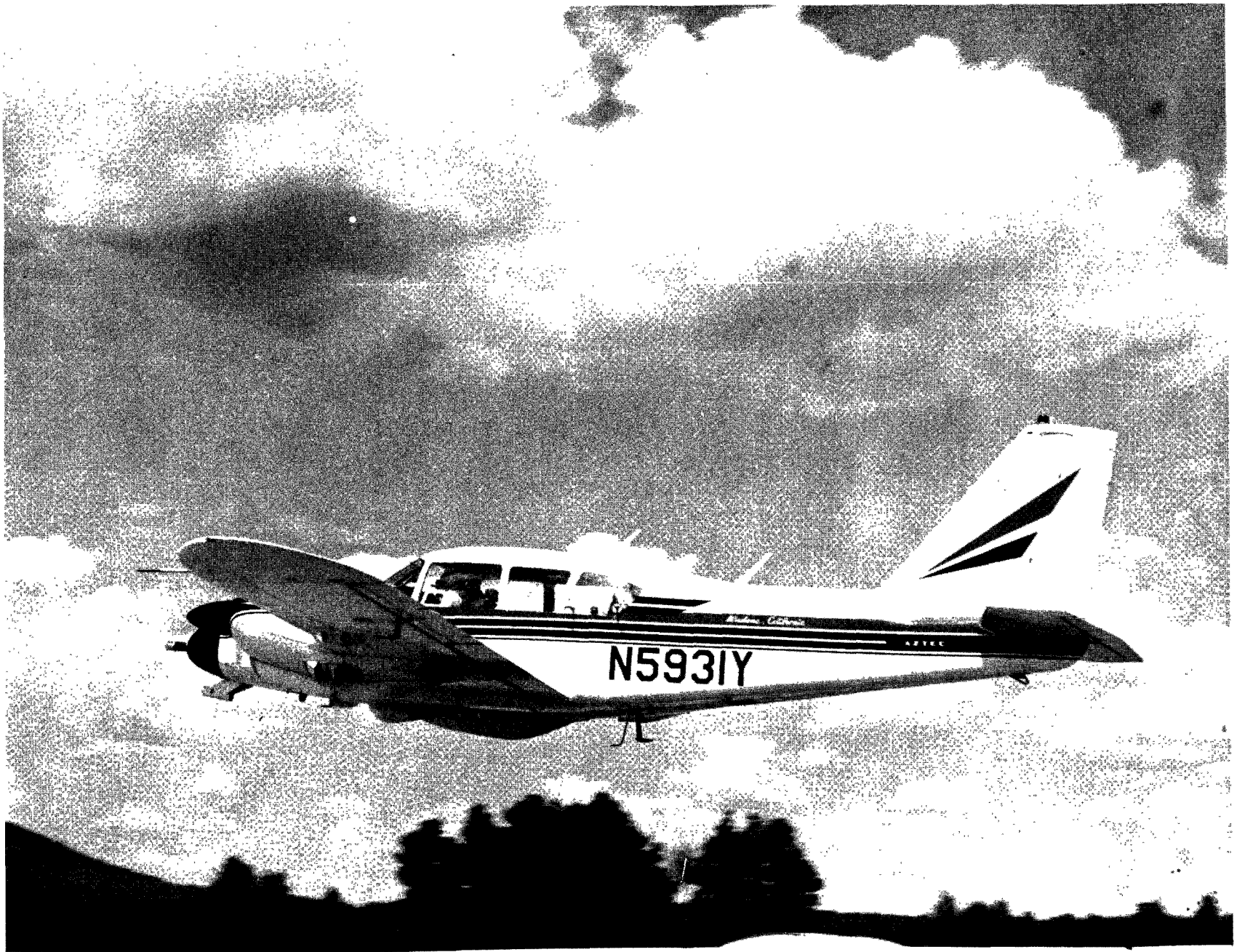

Fig. 1. INSTRUMENTED AZTEC C. The UITS turbulence probe extends out from the left wing. The cylindrical field mill is on the nose. A hydrometeor charge sampler, not used on the Keystone project, is under the nose. The air sample intakes for the MSI are on the rear left window.

recorded voice notes on a magnetic tape recorder as well as keeping some notes on a pad. The Integrating Nephelometer and potential gradient unit were installed but not operated during the program.

One particle sampling device was the Continuous Particle Collector (CPC). This is described in detail by MacCready and Todd (1964). A film coated with a liquid plastic is continuously moved past a slit exposed to the ambient air on an arm extending several feet outside the side of the nose of the aircraft. Particles impact on the film, and are encapsulated in the plastic which hardens in a matter of seconds. The deposit is then preserved for evaluation: for viewing by projecting in a standard 16-mm stop-motion movie projector, or for quantitative evaluation by taking photomicrographs which are examined on a semi-automated analog-digital converter. One great virtue of the technique is that the shape of the impacted particle is preserved as a casting, even though it may contain liquid which evaporates through the film. At typical flight speeds, some particles down to 2 μm diameter are collected, although questionable collection efficiencies in this size range make it difficult to give quantitative concentration results for particles below 4 or 5 μm diameter.

The main sampling device was the MRI Moving Slide Impactor (MSI). This device and the associated evaluation techniques are fully described by Goetz (1969). In this instrument, a deposit is continually impacted via a vacuum system onto a very smooth metal slide. The slide is steadily moved perpendicular to the impaction slit, yielding a time-varying deposit spread out along the slide. The slit design permits good impaction with low pressure drop, thereby disturbing the particles less than is the case with standard impactor slits, and the design features a very sharp deposition width, affording excellent time resolution on the slide. Evaluation was by standard photomicrograph techniques. Most of the evaluation was performed from pictures taken with dark field illumination; this permitted counting (but not sizing) of particles considerably smaller than the wavelength of light. For a few cases, a scanning electron beam microscope was employed to give very accurate data for all particle sizes. A light-scattering intensity meter was used for quick scans of the slides. With a stronger vacuum than was used here, the MSI collects particles down to about 0.1 μm diameter. For this project, the complete cutoff was at about 0.2 μm. Some particles larger than about 10 μm will tend to get deposited in the inlet and entrance tubing. Figure 2 shows the location of the MSI in the Aztec. The MSI had two slits depositing side by side on the slide. A flow of 5.2 liters/min was drawn through each slit. The air would take about 2 sec from the time it entered the tube until it passed through the impactor.

Turbulence was measured with the UITS described by MacCready (1964a, 1966). High frequency pressure (airspeed) fluctuations are

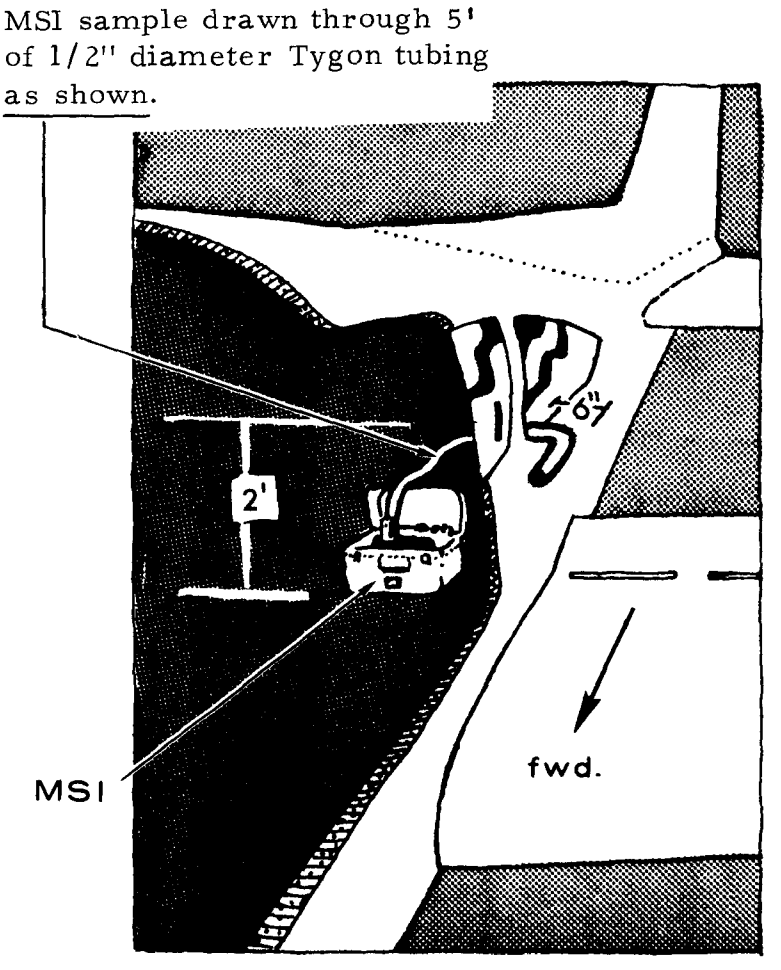

Fig. 2. MOUNTING OF THE MSI IN THE AZTEC

measured with a pitot-static pressure differential system, and the turbulent energy is found in a particular frequency range (the inertial subrange of eddy sizes) where the transducer response is good and where the aircraft provides a stable platform. The system automatically adjusts system gain as a function of mean indicated airspeed and as a result is able to yield an output which is a measure of turbulence intensity independent of speed or aircraft type. The intensity value output, R, is actually $(\epsilon\rho/\rho_0)^{1/3}$ where ρ is density, ρ_0 represents sea level conditions, and ϵ is the dissipation rate ($cm^2 sec^{-3}$). For the Keystone flights, the altitude was always low enough so that the density ratio ρ/ρ_0 could be assumed to be unity to the accuracy required of the measurements. The instrument time constant was set at 1 sec. Although the measurement technique for ϵ involves the inertial subrange of eddy sizes, and many applications of ϵ are made in the inertial subrange, knowledge of ϵ is also of considerable value in some processes involving far larger scales. Such is the case in some diffusion instances and in the estimating of surface factors from aircraft measurements, as are discussed later in this report.

Test Procedure

A general schedule was made up for the various participants of the program so everyone would have equal opportunity to complete their contractual commitments.

MRI was scheduled to fly in the area of the Power Plant and to 8 mi downwind of the stacks from 0850 to 1000 and 1135 until 1315 on a normal operating day without interfering with any of the other measurements that were being made. MRI could also operate in the plume at distances downwind of the stack greater than 8 mi at times other than the scheduled ones.

A typical flight is shown in Volume II. It went as follows:

1. Takeoff from Jimmy Stewart Airport and head west to the Power Plant.

2. Make an upward spiral sounding upwind of the power plant for meteorological conditions and background particle samples, from 1500 to 5000 ft MSL.

3. Proceed to 2 mi downwind - make five or six horizontal sampling traverses across the plume for particles and meteorological conditions. Sample at the center, top, and bottom of the plume to give a vertical profile of conditions. If possible sample at the same time as the lidar measurements.

4. Proceed to five miles downwind and repeat the above sampling crosswind traverses.

5. Proceed to 10 mi downwind and repeat the crosswind sampling traverses.

6. Make a spiral sounding at 10 mi downwind for particle sampling and meteorological measurements.

7. Fly an along-plume traverse from 10 mi downwind to the Power Plant, attempting to stay along the centerline of the plume.

8. Return to the Airport.

9. Repeat the preceding steps in the late morning-early afternoon scheduled period.

For some of the days of the program, the preceding flight plan was modified to provide some background data for the Homer City and Conemaugh Power Plant areas. After the along-the-plume sample was taken from 10 mi downwind to the Keystone Power Plant, the aircraft would proceed to Homer City. There another spiral sounding would be made for meteorological variables and background particles. After the sounding, a horizontal traverse downwind of the stack would be made for about 5 mi. The aircraft would fly to Conemaugh and repeat the foregoing procedure.

On a few of the flights, special particulate sampling runs were made as requested by SRI to enhance the potential correlation between the lidar and particle sampling.

III. ESTIMATING τ_0 AND z_0

The Basic Relationship

It is generally accepted that for neutral (adiabatic) stability, the turbulent kinetic energy equation for a given level can be written

$$\frac{\tau}{\rho} \frac{\partial U}{\partial z} = \epsilon \tag{1}$$

where τ is the shearing stress, ρ is density, U is the wind speed, z is altitude, and ϵ is the rate at which turbulent kinetic energy is dissipated into heat. For non-adiabatic cases, terms for the vertical flux of heat and kinetic energy would have to be added to (1). In adiabatic conditions over homogeneous terrain, the logarithmic wind profile is valid

$$\frac{\partial U}{\partial z} = \frac{\sqrt{\tau_0/\rho}}{kz} \tag{2}$$

where τ_0 is the shearing stress at the surface, and k is the von Karman constant. If we make the additional assumption that the shearing stress is invariant between the surface and the level where (1) is applied, then the two equations can be used to show

$$\tau_0 = \rho(kz\epsilon)^{2/3} \tag{3}$$

Thus, from a measurement only of ϵ at some known height, τ_0 can be found.

The logarithmic wind profile, in integrated form, is

$$U = \frac{\sqrt{\tau_0/\rho}}{k} (\ln z - \ln z_0) \tag{4}$$

Combining (4) with (3) gives

$$\ln z_0 = \ln z - \frac{k^{2/3} U}{z^{1/3} \epsilon^{1/3}} \tag{5}$$

Thus, z_0 can be estimated from measurements of ϵ and U at some known height.

Range of Usefulness

The above relationships should be valid for steady-state conditions, in neutral stability, over homogeneous terrain, throughout the layer

where τ is constant. In the real case, the conditions are not the idealized ones, but the validity of the concept may be adequate for at least qualitative estimates of τ_0 and z_0. The validity can be studied by examining the accuracy of (1) and (2).

Dr. Leonard Myrup (private communication) has pointed out that, concerning (1), Hess and Panofsky (1966) have presented strong evidence that under unstable conditions there is a strong tendency for energy produced by buoyancy to be exported aloft. That is, the omitted terms of (1) tend to balance even under rather unstable conditions. Thus the simplified equation may be valid over a wider range than originally thought.

As for (2), its accuracy depends on stability. One can use the more accurate exponential wind profile introduced by Swinbank (1964)

$$\frac{\partial U}{\partial z} = \frac{\sqrt{\tau_0/\rho}}{L}\left[1 - \exp\left(-\frac{z}{L}\right)\right]^{-1} \qquad (6)$$

where L is a measure of atmospheric stability which can be estimated from knowledge of wind speed and temperature gradient. This more accurate equation should be employed if the most accurate τ_0 measurements are desired, but it is much more complex than (2) and requires additional observational data. Over land, we estimate (2) will usually be accurate enough for altitudes of well above 30 meters for cases of moderate instability, and altitudes exceeding 100 meters for cases close to neutral stability.

As to the constancy of τ with height, in the practical case this should be a reasonable assumption for an atmospheric layer deeper than that for which (1) and (2) are valid.

The obvious approach to using airborne ϵ measurements and U observations for τ_0 and z_0 calculations is to take advantage of the cases where the relationships are most applicable. This would be in strong wind cases, in neutral or slightly unstable lapse rates. For stable cases, the method seems unfeasible.

Observations

Observational data to use with the above approach for τ_0 and z_0 estimates were obtained on the project on a low priority basis. The flight measurements and notes were primarily made for other purposes, but nevertheless can be used here to illustrate the technique.

For the calculation of τ_0 by (3), the best method from the standpoint of simplicity and statistical reliability is to fly at one constant,

low altitude z and measure the average ϵ. The existence of rolling terrain made this difficult, as did the requirement to concentrate flight observations at plume heights and also avoid lower elevations where helicopters were operating. On the first day of the project, we did such flights, since the helicopters were not operating, and there were several other instances during the program. In other cases, the best data are derived from sporadic vertical soundings at several locations, where data were obtained down to about 150 meters above the ground. Since individual $z\epsilon$ values have no statistical validity, average $z\epsilon$ values have to be used. For horizontal flight, the ϵ averages were obtained by eye. For the vertical soundings, the $z\epsilon$ averages throughout the lowest observed several hundred meters were used. For estimating these latter averages, overlays were prepared giving constant τ_o lines as a function of z and ϵ, for the scales used in the data presentation of Volume II, the Processed Data Supplement. Estimated values of τ_o were read off the computer plots of ϵ vs. z with the help of these overlays. There is great variability to the ϵ soundings, so the resulting, indicated τ_o values must be deemed crude estimates only. Soundings were used only if some suggestion of an inverse z - ϵ relationship existed in the plots. The results are given in Tables II and III.

Table II

SOUNDING DATA AND SURFACE ESTIMATES

Date 1968	Time	Case #	Location	Stability*	U** (m/sec)	τ_o (dynes/cm^2)	z_o (cm)
Oct. 16	1053	23	Homer City	Near neutral	2.7	5	3400
Oct. 16	1115	26	Upwind of Keystone	Near neutral	2.7	4	2800
Oct. 17	0839	36	Upwind of Keystone	Stable	5.7	0.7	1.5
Oct. 17	1007	53	10 Downwind of Keystone	Slightly stable	3.6	10	3700
Oct. 17	1104	54	Keystone to Homer City	Slightly stable	3.6	7	2750
Oct. 17	1132	56	Upwind of Keystone	Near neutral	5.7	5	525
Oct. 20	0918	74	Upwind of Keystone	Stable	7.2	1.0	6700
Oct. 20	1015	83	Homer City	Neutral	4.3	3	580
Oct. 20	1037	85	Conemaugh	Neutral	4.3	2	270
Oct. 21	0856	88	Homer City	Stable	5.9	4	310
Oct. 21	1040	92	Upwind of Keystone	Slightly stable	5.0	6	4450

* Stability estimated as a composite, for below stack top levels, from Vol. II, from the SRI final report, and from the Sign-X final report.

** U estimated from pibals at 180 meters above ground.

Table III

HORIZONTAL TRAVERSE DATA AND SURFACE ESTIMATES

Date 1969	Time	Case #	Height* z = (m)	Turbulence ϵ ($cm^2 sec^{-3}$)	Location	Stability	U** (m/s)	τ_o (dynes/cm^2)	z_o (cm)
Oct. 15	1407		110	50	Upwind Keystone	?	~4	4.4	760
Oct. 17	1210	58	160	70	5 Downw. Keystone	Neutral	4.6	7.0	1400
Oct. 20	0943	80	160	70	2 Downw. Keystone	Neutral	3.8	7.0	2150
Oct. 20	1003	81	110	0.4(1st $\frac{1}{2}$)	10 Downw. Keystone	Neutral	4.1	1.8	1500
				4.0(2nd $\frac{1}{2}$)				8.2	550
Oct. 20	1008	82	160	100	10 Downw. Keystone	Neutral	4.1	9.0	2350

* Height is above ground.

** U estimated from pibals at 180 m above ground.

The estimates of τ_o seem not unreasonable, most being in the range 2 to 8 dynes/cm^2. Putting this in terms of u^*, this means 41 to 82 cm/sec. The z_o values are far more erratic, varying over more than three orders of magnitude. It should be expected that the z_o computations would show far more scatter because of two factors. First, an additional variable, U, is required in their calculation, and the U is here derived from a spot measurement at a location which may not be representative of the region of the ϵ measurements. Second, the computation involves finding the small difference between two large quantities (5), and so errors in U, ϵ, and z produce large uncertainties in z_o. The calculated z_o values are mostly quite large. One might have expected values in the 30 to 300 cm range, from noting the generally rolling terrain, some trees, and the large power plant complexes themselves. In all these interpretations, the non-homogeneity of the turbulent regimes in time and space should add appreciably to the scatter. One clear example of this is the double case (#81) on Table III. For the first half of the horizontal run, ϵ was low, while for the second half it was high, hence yielding different τ_o and z_o values. In the z_o calculations, the extreme values came from two of the three "stable" cases, a not unexpected result since the air at the aircraft observational altitude is effectively decoupled from the ground.

This attempt at deriving τ_o and z_o from aircraft measurements must be deemed as introducing the concept, not trying to use the concept to obtain practical numbers. For proper exploitation of the method, the flights should be lower (say, 100 m or below), height should be accurately monitored (say, by radar altimeter in complex terrain situations), the

observations should extend over distances or times affording a chance for statistical significance, and cases should be chosen where the wind is strong and the lapse rate close to neutral. Obviously the most definitive tests would be over terrain where prior or present projects established the τ_0 and z_0 values for comparison.

Slade (1969) has derived z_0 information for "rough and inhomogeneous terrain" around an instrumented tower located in the northwestern section of Philadelphia. The data came from wind profiles in neutral conditions. For northerly winds, z_0 was about 270 cm; for southerly winds, it was considerably less than one meter. Data up to 175 meters proved useful for the calculation. The z_0 for northerly winds is comparable to some of the z_0 calculations of Tables II and III. Checks of the airborne instrument technique for deriving z_0 would be especially desirable at this tower location where z_0 data have already been established. The UITS should be helicopter-mounted for the required low flight over the urban area.

IV. THE DECAY OF THE TURBULENCE IN THE PLUME

The initial plume can be expected to contain strong turbulence. This will decrease in time until the plume turbulence is indistinguishable from the ambient turbulence. The distance, x^*, where the atmospheric turbulence begins to dominate entrainment, must be a function of the stack parameters, environmental stability, and environmental turbulence. The significant environmental turbulence factor should be ϵ, since the size scale involved is of the same order of magnitude as the inertial subrange. Briggs (1969) develops a formula for x^*:

$$x^* = 0.43\ F^{2/5}\ (\beta^{-3} U \epsilon^{-1})^{3/5} \tag{7}$$

where $$F = \frac{g Q_H}{\pi c_p \rho T},$$

with g = gravity, Q_H = heat emission of stack gases, c_p is specific heat of air at constant pressure, ρ is air density, and T is temperature. For normal conditions,

$$F = 3.7 \cdot 10^{-5} \left[\frac{m^4/sec^3}{cal/sec}\right] Q_H$$

β is a non-dimensional coefficient of order unity

U is the mean wind speed.

By finding $\beta = 1$ empirically, and noting ϵ vs. U and z empirical relationships, he further derives:

$$x^* = 0.52 \left[\frac{sec^{6/5}}{ft^{6/5}}\right] F^{2/5} h_s^{3/5} \qquad (h_s < 1000 \text{ ft}) \tag{8}$$

$$x^* = 33 \left[\frac{sec^{6/5}}{ft^{3/5}}\right] F^{2/5} \qquad (h_s > 1000 \text{ ft}) \tag{9}$$

where h_s denotes stack height.

On the present project, there were cases where the plume turbulence and environmental turbulence were sampled at 2, 5, and 10 miles. Thus there may be a chance to see if the predictions of (7) are consistent with the observations. Unfortunately, the data show extreme scatter -- especially, there are big variations in ϵ at different altitudes, all still at plume heights. The data are summarized in Table IV .

Table IV

TURBULENCE VS. DISTANCE

Date	Distance (mi)	No. of Traverses	$\overline{\epsilon}_{outside}$	$\overline{\epsilon}_{in\ plume}$	$\epsilon_{in}/\epsilon_{out}$
Oct. 15	2	5	17	68	4.0
	5	3	33	32	1.0
Oct. 16	2	3	8	20	2.5
	5	4	3	19	6
	10	1	2.3	11	5
Oct. 17	2	5	1.8	11	6
	5	8*	0.6	1.9	3
	10	2	1.9	15	8
Oct. 20	2	6	1.7	4.8	2.8
	10	1	9	114	13

*One strong turbulence traverse omitted.

Using (7) and a representative value of 30 cal/sec $\times 10^6$ for Q_H, one finds

$$x^* = 4100 \text{ m (2.6 miles) for } \epsilon = 1 \text{ cm}^2\text{sec}^{-3}$$

$$x^* = 533 \text{ m (0.3 mile) for } \epsilon = 30 \text{ cm}^2\text{sec}^{-3}$$

Comparing such numbers with the experimental data for October 17, where the ambient turbulence is approximately $\epsilon = 1 \text{ cm}^2\text{sec}^{-3}$, we see the prediction is decay to ambient in a bit over two miles, and the evidence could be deemed consistent with this if we eliminate the odd increase in the plume turbulence during one pass at 10 miles. Since there was also one strong turbulence traverse out of eight at 5 miles, perhaps the elimination of one data point at 10 miles is not improper. For October 16, with light turbulence, the data suggest the plume turbulence decays more slowly than (7) would have predicted. For October 15, with moderate turbulence, the experimental evidence suggests the plume turbulence is still present at 2 miles but the equation suggests the ambient turbulence would have taken over completely some time earlier. The October 20 data beyond 2 miles seem spurious; the existence of some excess turbulence at 2 miles is not inconsistent with (7).

Using (8), with $h_s = 245$ meters, gives $x^* = 237$ m (0.15 mile), much smaller than suggested by the data.

In summary, the data as analyzed show considerable scatter and so cannot be used to establish an equation's validity. However, acknowledging the scatter, they are at least not inconsistent with the thought that for weak turbulence (7) represents a good starting point but perhaps somewhat underestimates the distance for the plume turbulence to decay to the ambient value.

V. PARTICULATE MEASUREMENTS

The Three Methods

Particles were directly measured in three ways on the MRI program.

The first method involved the use of the Charlson Integrating Nephelometer (Charlson, Ahlquist, Selvidge, and MacCready, 1969). This was installed on the aircraft with the intention of making measurements on the ferry flight to and from Pennsylvania, as well as during the experiments at Keystone. The instrument was an airborne unit borrowed from Dr. Charlson at the University of Washington. It suffered an electronic failure on the initial ferry flight when about 800 miles from the West Coast and could not be repaired during the course of the field program. The program had been designed to be able to proceed without this instrument, but the equipment failure was certainly disappointing because, with its fast response time, this sensor would have clearly identified the plume position on the aircraft instrument chart records, and it also would have provided quantitative total scattering data for comparison with the SRI lidar. After the field program was completed, the instrument was quickly repaired and it has worked reliably since, as have other versions of the nephelometer which have been employed in mobile service in automobiles and aircraft.

The second two-particle measurement methods were aimed at collecting particles during aircraft traverses through the plume, primarily for comparison with the lidar observations. The methods involved collecting small particles (in the 0.2 to 10 μm range) with the Moving Slide Impactor (MSI), and collecting a larger range of particles (2 to 100 μm) with the Continuous Particle Collector (CPC). The samples were collected for subsequent evaluation in the laboratory. The overlap in the size ranges covered by the instruments was to afford an opportunity for cross calibrations. In spite of a considerable investment in evaluation effort, the CPC data were not of particular value to the program. The main light scattering was apparently from smaller particles than the CPC handles, and the few larger particles were difficult to identify on the film amidst a background of a small number of spurious particles.

The MSI collects particles appropriately over the 0.2 to 10 μm range, with perhaps some small loss of particles at the large end of this range due to removal in the tubing prior to the MSI, and a low collection efficiency at the lower end of the range. The main problem turned out to be evaluation, not sampling. It was anticipated that the mean particle size would be 2 or 3 μm, large enough for at least crude assessment by means of ordinary microscopy. However, from some preliminary looks

at the slides it appeared that the preponderance of particles from plume regions were smaller than this. Consequently, dark field illumination photomicroscopy was employed in the main evaluation. This technique permits counting of particles down to the minimum size being collected here, although the small particles cannot be sized. The apparent size depends on illumination -- and various amounts of illumination were employed so as to try to extract the best possible information from the technique. To obtain definitive information about the particulates, scanning electron microscope photos were made of a few slides. These photos only became available very late in the program. Details on these approaches are given later in this section.

The Fly Ash

We obtained a sample of the stack particulate through Mr. Schiermeier of NAPCA. Figure 3 shows this fly ash. Almost all of it has been fused into clear glassy spheres or globules. There is relatively little small material. The size distribution of this sample is given in Fig. 4. This distribution was obtained with normal microscope illumination, not dark field. Mr. Keller of the Keystone Plant stated the burner runs between 1650 to 1690°C. Almost all the expected minerals in the effluent melt before this temperature, which accounts for the fused appearance.

Evaluation of the MSI Samples

There were 84 MSI slide samples taken on this program. The MSI slides were moved during collection at rates which were varied for different slides depending on the anticipated density of deposit. There were six speeds available, from 12 to 384 seconds per slide traverse. During evaluation, each slide was divided into 18 increments covering the collection period. Size distributions were measured, and also relative light-scattering values. The impacted samples proved to be extremely stable, allowing the samples to be reprocessed as desired.

To obtain the size distributions, photomicrographs were made under dark field illumination and projected onto a Benson-Lehner OSCAR S-2, from which IBM cards were punched with a human operator. Initially, the particles were sized into 2.5 μm intervals, but when it became apparent that there was a preponderance of small particles, the evaluation technique was shifted to give 0.5 μm size intervals. Figure 4 shows an example: the size distribution for MSI sample Slide #4-18, a sample from the plume 10 miles downwind of Keystone. The left-most of the two adjacent curves

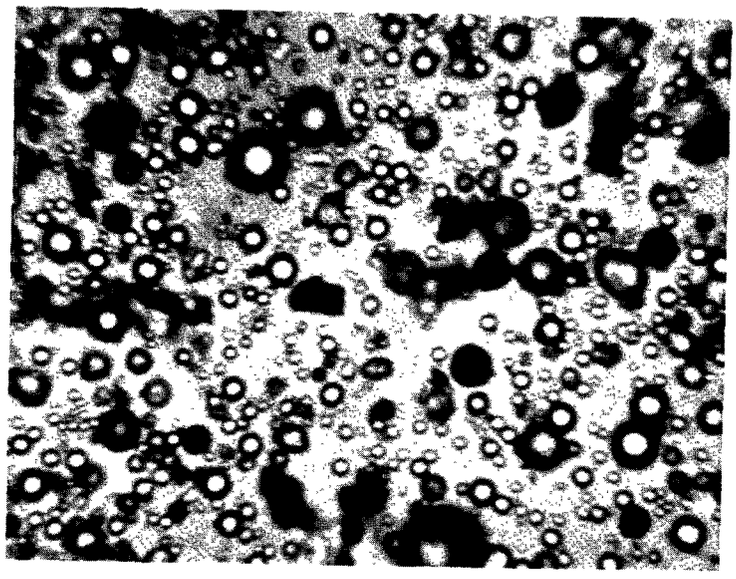

440 X

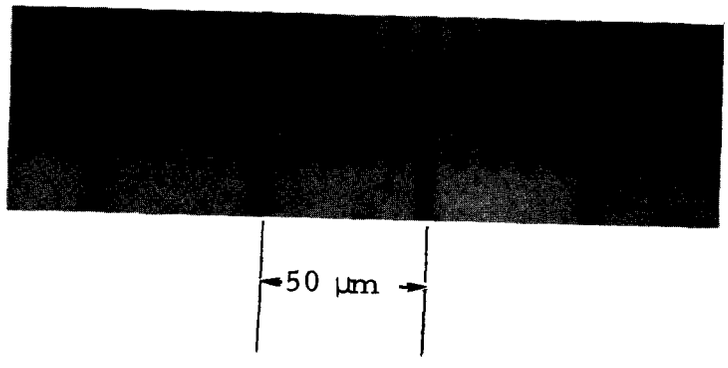

Fig. 3. STACK PRECIPITATE

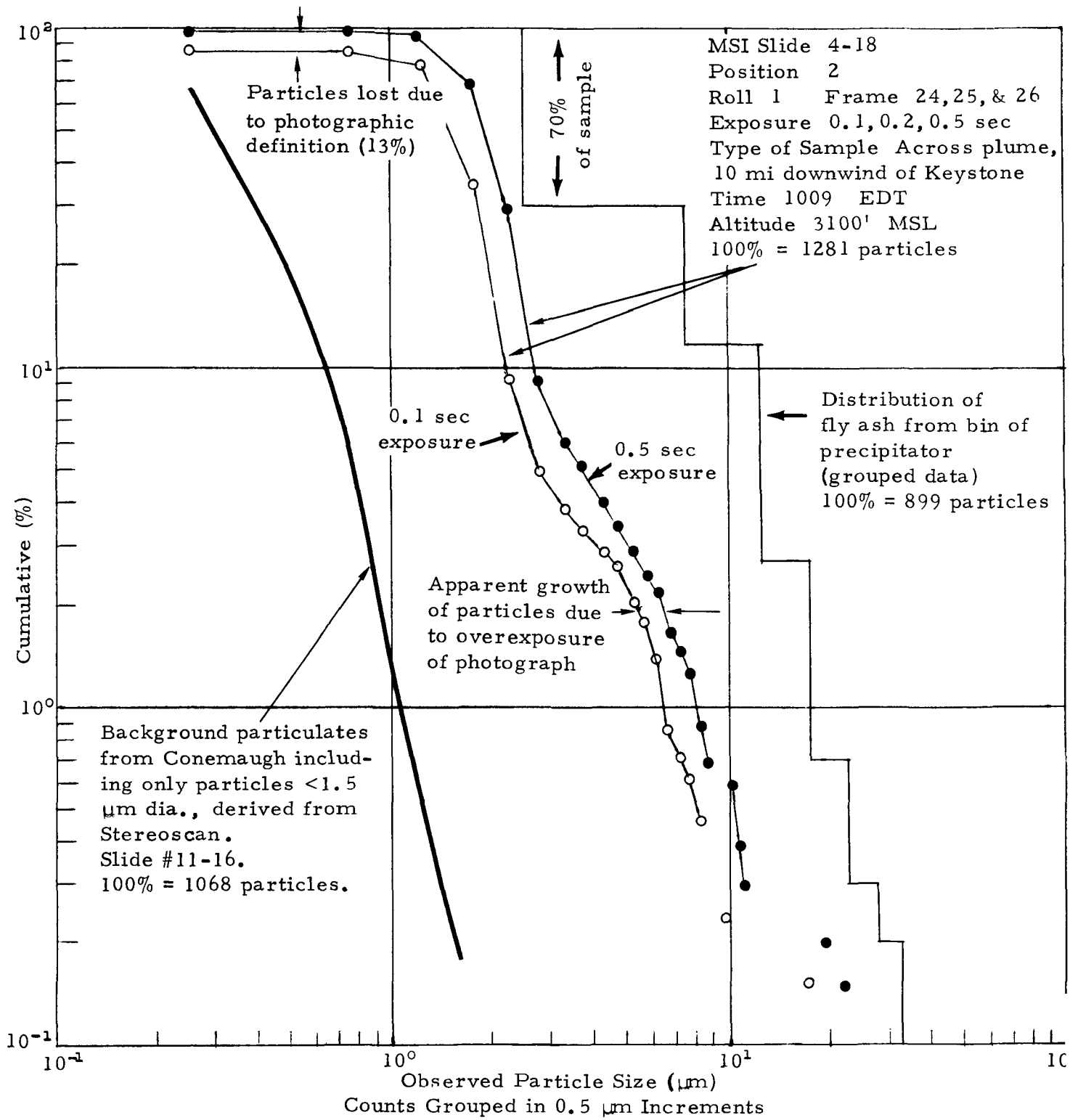

Fig. 4. DISTRIBUTION CURVES STACK PRECIPITATE, FLY ASH, AND THE ENVIRONMENT

is deemed the more correct since the shorter exposure decreases the halo effect on the film. This effect is described in greater detail later. As will also be described, the distributions handled this way still make the small particles appear larger than they really are. Thus the Slide #4-18 curves of Fig. 4 should not be considered accurate; a somewhat flatter slope should be closer to the truth. Twenty such size distribution compilations were made, but they are not presented here because they are considered misleading.

For a quicker assessment of the spatial variation of particle light scattering, light scattering of the MSI slide deposit was measured by the method of Goetz (1969). Figure 5 is an example of the resulting plots. All such plots are given in Vol. II, the Data Supplement. There is no absolute calibration available relating this to light scattering in the atmosphere. If the Integrating Nephelometer had been operable, a crude calibration would have been achievable. The calibration would vary somewhat with particle size distribution and material. Even without an absolute calibration, the light scattering plots are helpful in delineating the plume as long as particle concentrations are appreciably above the background noise. In a qualitative way, they should correlate reasonably with the lidar scattering observations.

The total numbers of particles, rather than the size distributions, are considered valid. Table V summarizes these concentration data.

Light Microscope Vs. the Scanning Electron Microscope

The two photographs, Fig. 6, are prints of original negatives of the sample of particulate on Slide #4-18 prepared by the dark field illumination method. One can clearly see the apparent growth of the particles as a function of film exposure; the "halo" caused by light scattering makes it impossible to size the smaller particles accurately. The photographs are suitable for determining the number of particles; just a few more are visible in the 1/2-second exposure than in the 1/10-second exposure.

The series of photographs on Fig. 7 are pictures of exactly the same particle sample (but a slightly different portion) taken through the Engis Stereoscan Electron Microscope through the courtesy of Mr. John Devaney of the Cal Tech Jet Propulsion Laboratory. The second photo in this sequence has the same magnification (525 X) as the photos on Fig. 6. The crude "C" shown on the first Stereoscan picture was etched into the sample on the slide to allow return to the area of interest if desired. The picture at 525 X still does not answer the question as to the exact size of the smallest particles. Therefore, magnification was increased geometrically to 5,250 X until these smallest particles could be measured with high confidence. From Fig. 7 it can be observed that the

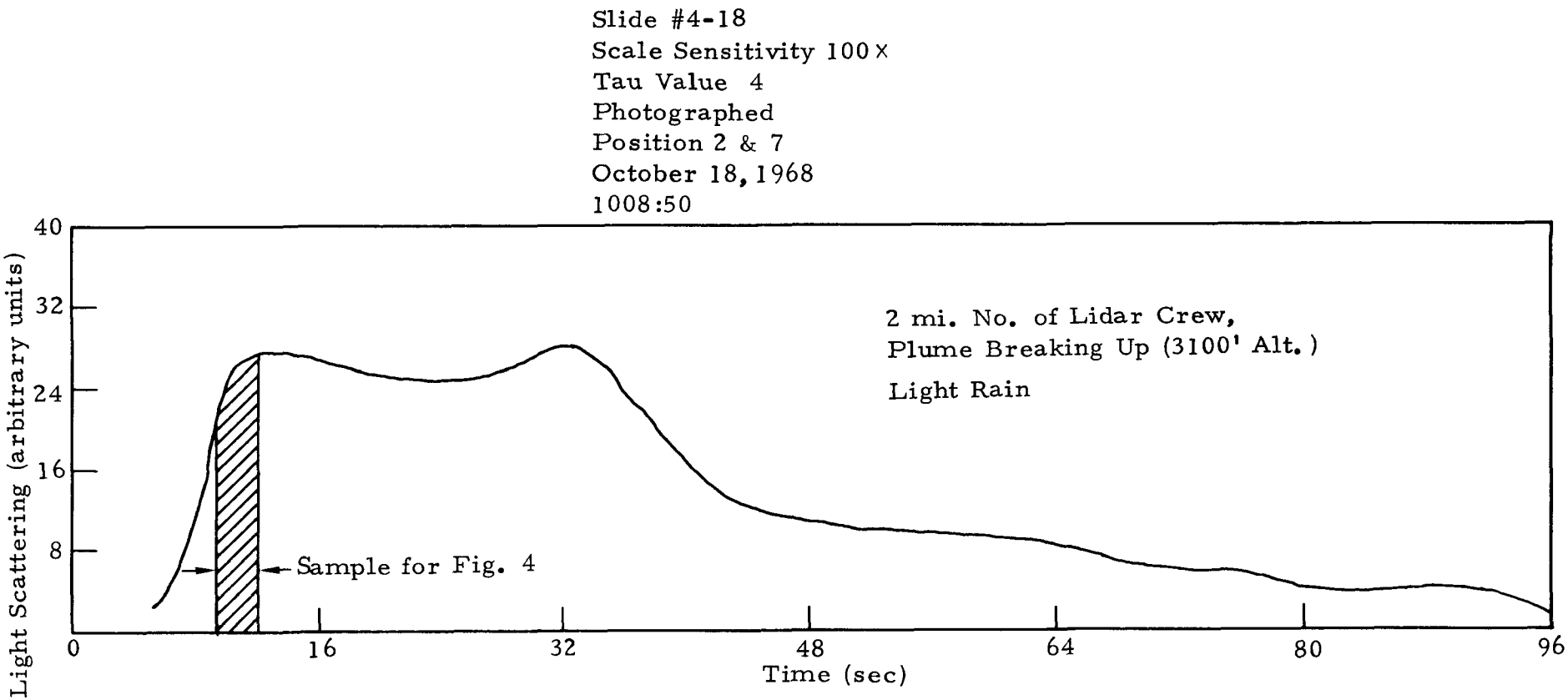

Fig. 5. LIGHT SCATTERING PLOT

Table V

PARTICLE CONCENTRATIONS

Slide #	Increment	Sample Code	Concentration (particles/cc)
5-16	2	01	740
2-17	4	01	495
16-17	10	03	433
22-17	17	02	86
23-17	2	02	102
	12	02	163
24-17	5	02	193
	8	02	146
	17	02	93
26-17	5	19	2,815
1-18	3	03	107
4-18	2	03	252
	7	03	293
6-18	5	09	137
1-21	10	01	95
4-22	18	01	36
6-22	13	01	105
7-22	13	01	95
8-22	2	01	80
12-22	7	30	615

See Volume III for key relating Slide Number to specific time and location.

Abbreviated Sample Code Key

01	2 mi downwind
02	5 mi downwind
03	10 mi downwind
09	Ascending spiral upwind
19	In knee of plume
30	In plume over lidar

Film Exposure 1/2 sec

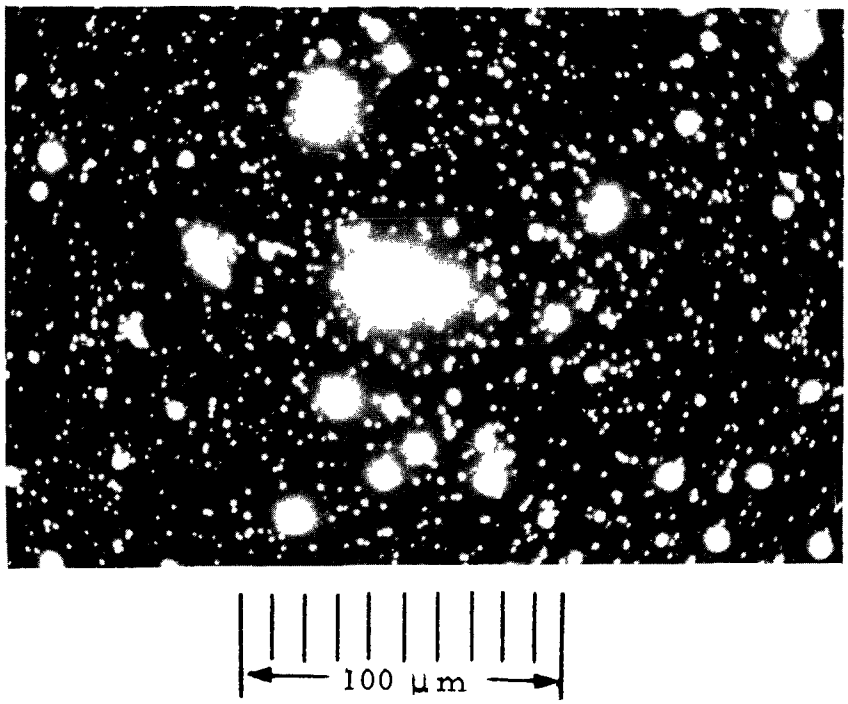

Film Exposure 1/10 sec

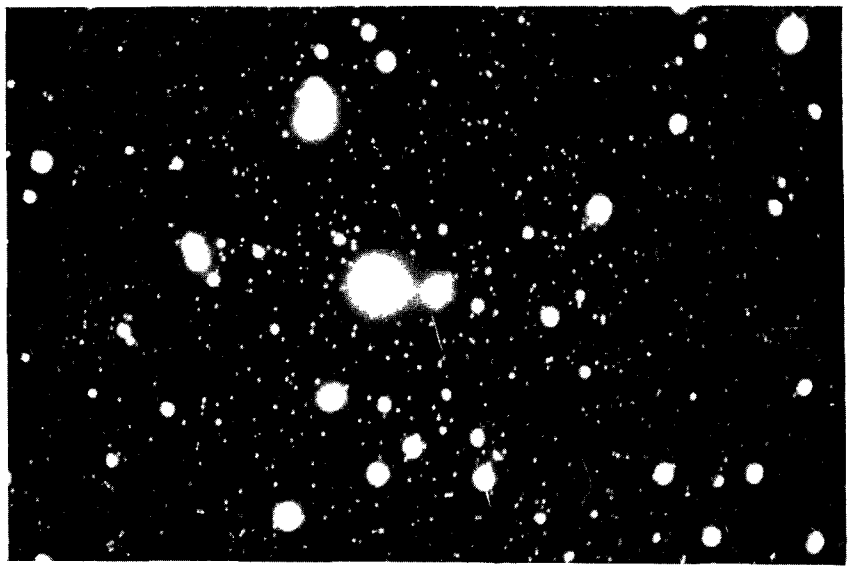

Fig. 6. SLIDE #4-18, BLACK FIELD PHOTOMICROGRAPHY
Representative sample of the effluent 10 mi. downwind of Keystone.

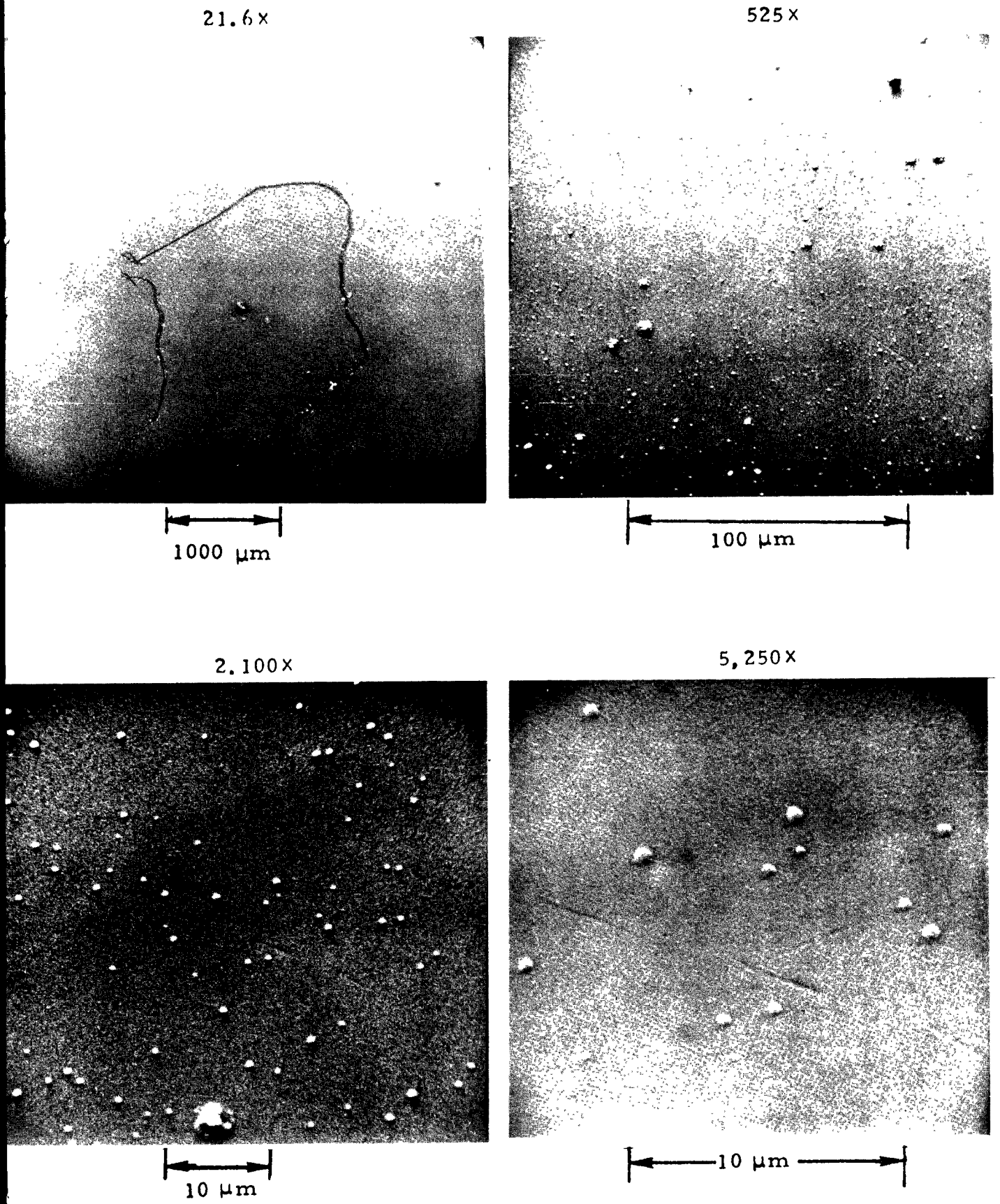

Fig. 7. SLIDE #4-18, STEREOSCAN ELECTRON MICROSCOPE

smallest particles in the sample are of the order of 0.3 μm in diameter, and the sample contains a large percent of particles well below 1 μm.

Figure 8 is an equivalent series of electron microscope photographs of Slide #11-16. This sample was taken during a spiral sounding over Conemaugh, more than 50 miles from Keystone. It represents a typical Pennsylvania background environment. The MSI slide movement was slower in taking this sample than it was for the sample in Fig. 7. To compare the 525× magnification photos on Figs. 7 and 8, the Fig. 8 deposit should be decreased by a factor of 16. Even taking this into account, it can be seen that the background environment may constitute a considerable percentage of the small particles in the plumes shown in Fig. 7. The approximate particle size distribution derived from Fig. 8 is indicated on Fig. 4. Particles larger than 1.5μm diameter were not counted for the Fig. 4 size distribution, but in any case they represented only a small percentage of the number.

The Stereoscan photographs of Fig. 9 are included for subjective inspection. They are also from Slide #4-18, in the plume. Of special importance is the lower left photo. It distinctly shows that the particle was large and probably liquid when it impacted, and then subsequently evaporated to the final form.

Figure 8 shows what might be impaction patterns around the larger particles. These may be indicative of impaction of larger liquid droplets and subsequent evaporation, or, less likely, they may be a polarization phenomenon whereby electrical forces help orient particles. The late Dr. Alexander Goetz and his staff examined the photo and felt that no definitive conclusion could be drawn solely from the present evidence. The satellite patterns around the larger particles resemble those sometimes observed with sulfate particles.

It is to be noted that the photos of Figs. 7, 8, and 9 show a fairly distinct cutoff below 0.2 or 0.3 μm. It seems probable that this is caused by collection efficiency characteristics of the MSI. This small end of the particle size spectrum is not of particular importance here because it contributes in only a minor way to light scattering.

Further Comments

The CPC operated appropriately throughout the program, and much effort was devoted to evaluating the 6334 feet of film obtained. Nevertheless, no quantitative data were obtained from it. Fly ash smaller than 5 μm could be observed, but the less common larger fly ash could not be definitely established. One problem is that the CPC film tends to pick up spurious dust particles during evaluation which confuses the evaluation. This causes no particular problem when the CPC is used for its original role, collecting cloud droplets which exist in high concentrations, or

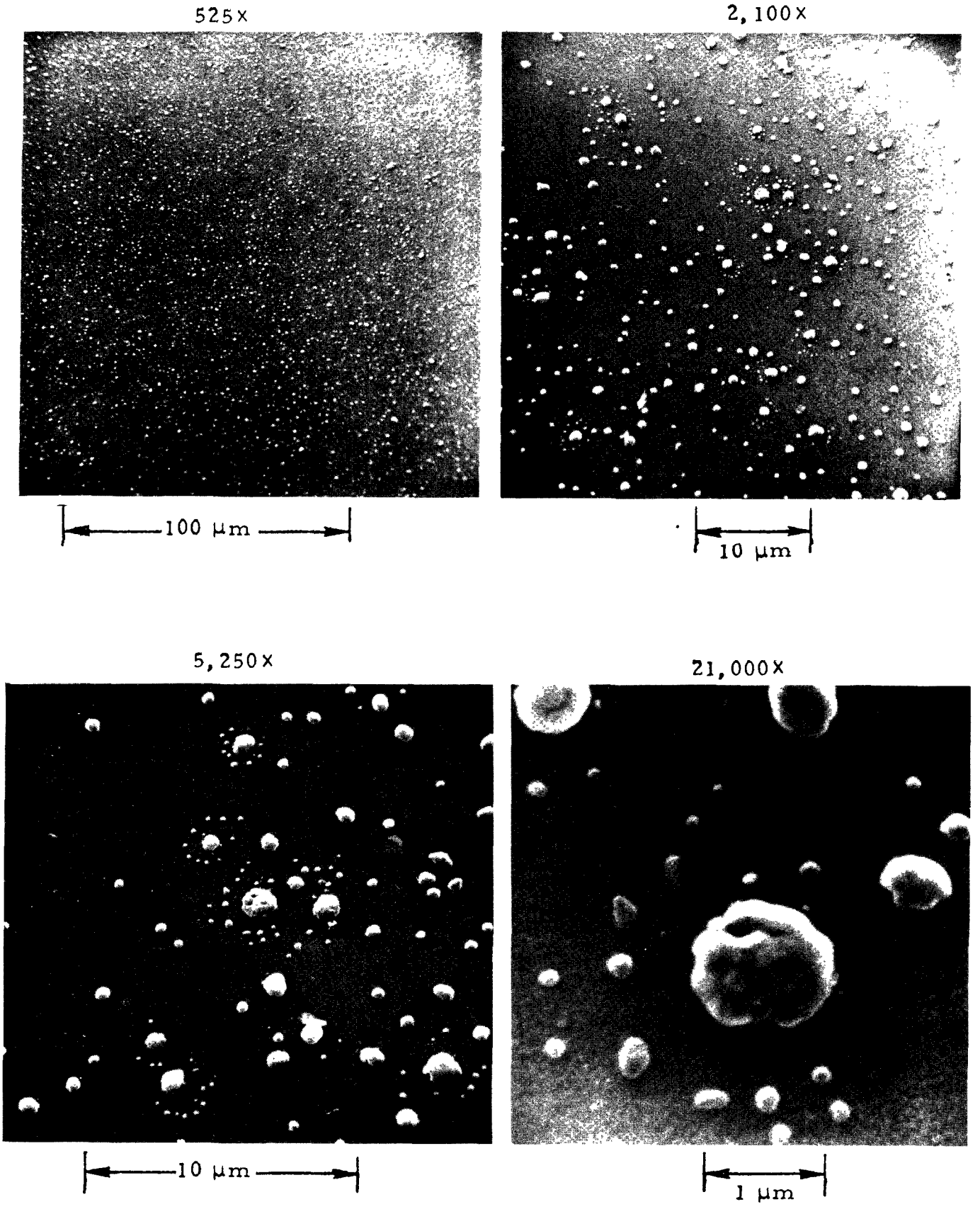

Fig. 8. SLIDE #11-16, STEREOSCAN OF AMBIENT AIR

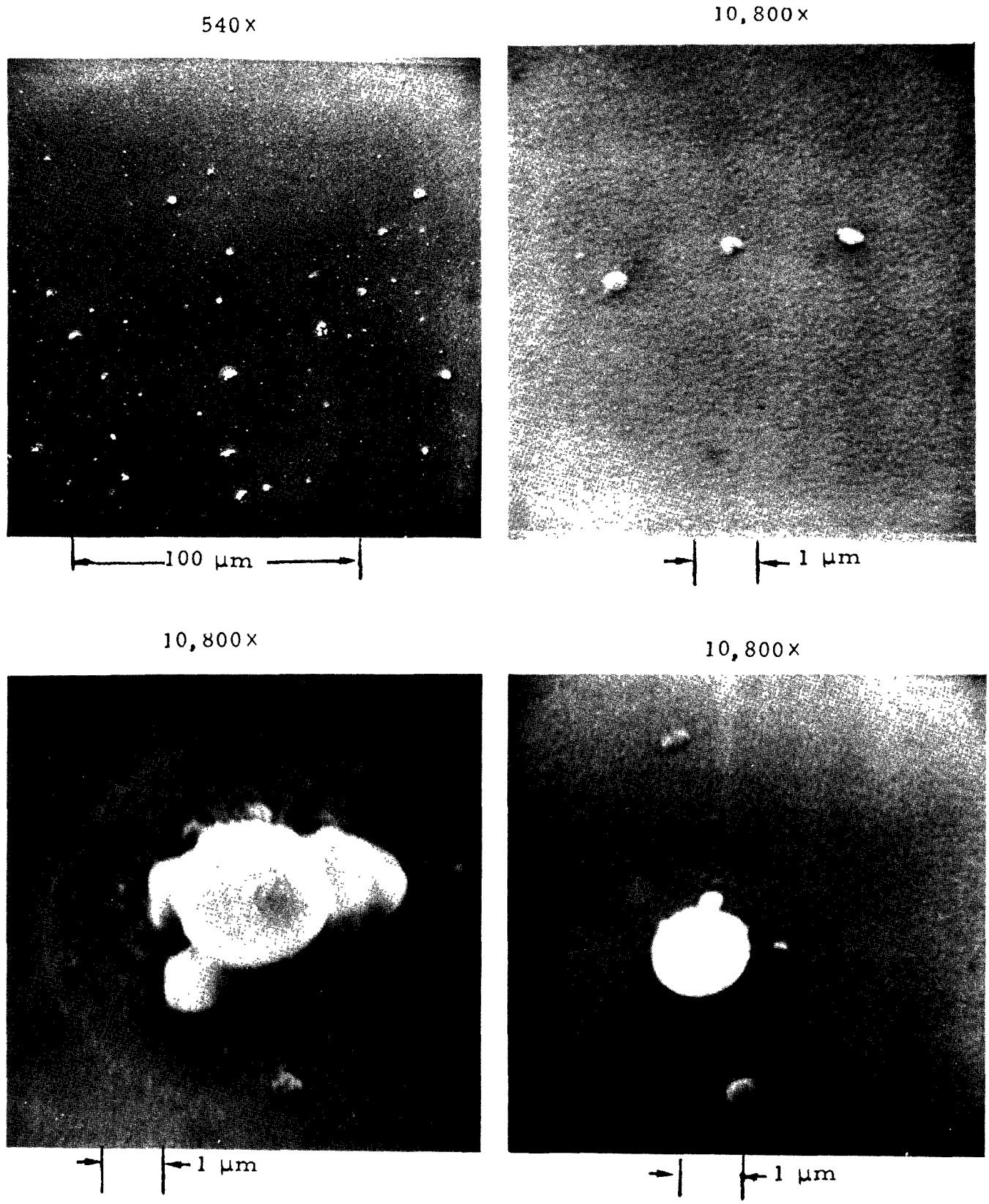

Fig. 9. SLIDE #4-18, ADDITIONAL STEREOSCAN PHOTOS

collecting ice crystals which are larger and distinctly shaped. It did cause a problem in the present study.

Things would be simple if one could say there is a particular concentration and size distribution of particles representing the background air, and an additional particular size distribution of particles representative of the stack effluent which can be superimposed on the background in amounts depending on the dilution. Unfortunately, reality is far more complex.

Concerning the fly ash size distribution, the distribution found for the precipitator (Fig. 4) analyzed from microscopy with standard illumination, gives some hint of the particles being mostly large. However, these are what are precipitated, and the distribution may not be representative of what is emitted when some precipitators are shut down as was the case in our airborne sampling. The best evidence should be from the sample taken in a strong portion of the plume. Slide No. 26-17 (see Table V) was taken in a "zip through the knee of the plume" and had an order of magnitude higher concentration than the other samples, so it should show the true fly ash spectrum. As analyzed with dark field illumination, with a correction for light intensity, half the particles were under 1.0 μm and 85 percent under 1.5 μm. The number of large particles, say 10-20 μm, was very small. Other samples from areas where the plume was less dense gave lower counts and a preponderance of somewhat larger sizes--but the distributions would be mostly representative of ambient conditions, and not shed light on the plume particulates. The plume was slightly colored, but this would be expected even with particles this small.

Concerning the background particles, Table V shows many cases of low concentrations in the plume at all distances (down to 36/cc) meaning the background would be as low or lower. There were also higher counts (615, 740/cc). The airplane observer in some instances noted strong systematic variations, in the vertical, of the haziness of the atmosphere. In summary, large background variations are to be expected, as a function of both space and time.

As to measurements specifically in non-plume regions, Table V shows Slide No. 6-18 to have 137 particles/cc. The "corrected" dark field size spectrum put 80 percent of the particles between 0.5 and 2.5 μm, with the maximum around 1.3 μm. For the ambient case near Conemaugh evaluated by the stereoscan electron microscope, the photos are on Fig. 8 and the size distribution for particles below 1.5 μm is given in Fig. 4.

In trying to put all of the above together, one must realize that there were various evaluation methods and various data from atmospheric cases with high variability. One must conclude that the dark field illumination technique, as applied, probably indicated particles at all sizes to be somewhat larger than actual, although perhaps total counts of all deposited

particles may be fairly accurate and relative sizes between samples should be valid. The size distribution of the airborne fly ash is in doubt. One conclusion is quite evident: systematic evaluation of all slide samples with the stereoscan electron microscope would have answered most of the questions in a definitive manner.

It was beyond the scope of this project to consider relative humidity effects. A large portion of the natural aerosols are typically hygroscopic, so the increased water vapor in the plume can result in a visible cloud, an increase in light scattering, even if no particles were being emitted. Such particles would evaporate on the sampler slide, so only the solid residue would be measured. The same effect would be true if the effluent particles were hygroscopic. The large ones are probably not. Thus one must conclude that the best correlation of airborne measurements with lidar would derive from light scattering measurement devices on the aircraft, such as the Integrating Nephelometer, not from particulate collections for subsequent laboratory assessment.

VI. METEOROLOGICAL ENVIRONMENT OF THE TALL STACK PLUME

The topics of interest in a consideration of the tall stack plume meteorological environment are the magnitude and directional wind shears, the height and frequency of occurrence of inversion transitions at plume altitude, the variation of turbulent mixing in the vertical as a function of meteorological and topographical conditions, and the variation in vertical mixing along the plume trajectory over complex topography. A definitive study of each or all of these topics is beyond the scope of this program; however, the field program was designed to obtain some data on each of the above aspects, and subsequent analyses did reveal interesting results as will be described in this and subsequent sections by drawing sample cases from Volume II.

The meteorological environment of the tall stack-large power plant plume is really that of the so-called planetary boundary layer of the atmosphere whose depth is on the order of one kilometer under near-neutral conditions of stability and one to three kilometers under conditions of strong instability. The depth of the planetary boundary layer under stable and inversion conditions is more difficult to define and is presently a subject of active research as is the planetary boundary layer problem in general. The tall physical height of the stack itself plus the large amount of effluent with a considerable exit velocity and excess temperature cause the plume to be at altitudes between about 300 meters and 1000 meters. This is a region considerably above that for which the large amount of research to date on the meteorological environment of plume rise and diffusion on conventional stacks has been done.

The distribution of the wind in the planetary boundary layer is undoubtedly the subject which has received the most study to date. In this regard, our best quantitative understanding is still confined to conditions of neutral stability and flat, uniform terrain. There exists some qualitative understanding of the effects of non-neutral stability and terrain roughness on the characteristics of the "Ekman spiral" type wind distribution. The situation of a strongly stable planetary boundary layer, however, in which adjacent layers become decoupled in their behavior from one another, so to speak, or where single or multiple inversion layers may exist, and where large terrain inhomogeneities or artificial roughness elements, like large power plant stations themselves, are present is indeed beyond all but our most meager qualitative understanding. At present it appears the problem area in greatest need of good observations under neutral and non-neutral stability conditions is over complex terrain. Fortunately, in the program under consideration, efforts were made by NAPCA to document the wind distribution affecting plume transport and diffusion by taking double theodolite pibal observations every half hour in the vicinity of the

Keystone Power Station. Examples of these observations which document some of the complexities alluded to above are presented in Figs. 10 to 12 All of the pibal data are also given in Volume II. Figs. 10 to 12 show the considerable changes in the magnitude and direction of the mean wind from the ground to plume top and the wind shears which exist over the time period of interest (early morning to mid-afternoon) relative to predicting ground level particulate and sulfur dioxide concentrations. It may be noted in these figures as well as similar ones for the other days in the October 1968 series that the time and vertical extent of inversion break-up transition from strongly stable conditions to near-neutral in the lower layers can be determined fairly easily from the directional wind shear characteristics. In this case on 17 October, the transition occurs about 1000-1030 EDT to at least 600 meters (MSL). This altitude, obtained from changes in directional wind shear characteristics, is consistent with that determined from directly measured vertical profiles of turbulence, before, during, and after transition which will be shown later in this section. It should also be noted in Fig. 12 that by 1200 the magnitude wind shears have been almost completely eliminated by the strong vertical exchange from convective processes.

From a consideration of the position of the mean plume altitude in the planetary boundary layer as well as the preceding examples of directly measured pibal wind profiles it is evident that the directional wind shear should have a significant influence on plume rise and horizontal diffusion. In addition, the magnitude wind shear which is normally rather small in this region appears to be rather large under certain conditions at Keystone, probably due to local terrain effects with certain mean wind directions. The complexities of wind directional shear on plume rise and horizontal diffusion have generally been ignored for conventional stack-concentration prediction problems and correctly so since the plume diffusion is occurring in a region of smaller or zero directional shear except under very special topographical conditions. The complexity of magnitude wind shear has generally been handled by adopting the convention of using the wind at stack top or vertically averaged over the plume depth. The wind directional shear values and characteristics are summarized in Table VI for the MRI photo periods in the October 1968 series. It may be noted that the difference in wind direction is typically large and reflects local topographical effects in the immediate vicinity of the Keystone Power Station. In order to aid in visualization of the transport and diffusion meteorology of the plume environment, Figs. 13 to 18 are presented. In these figures, the directional wind shear over the range of plume altitudes is shown along with the temperature profile from MRI aircraft observations and the vertical-time average of the wind speed. Plume dimensions derived photographically are also shown.

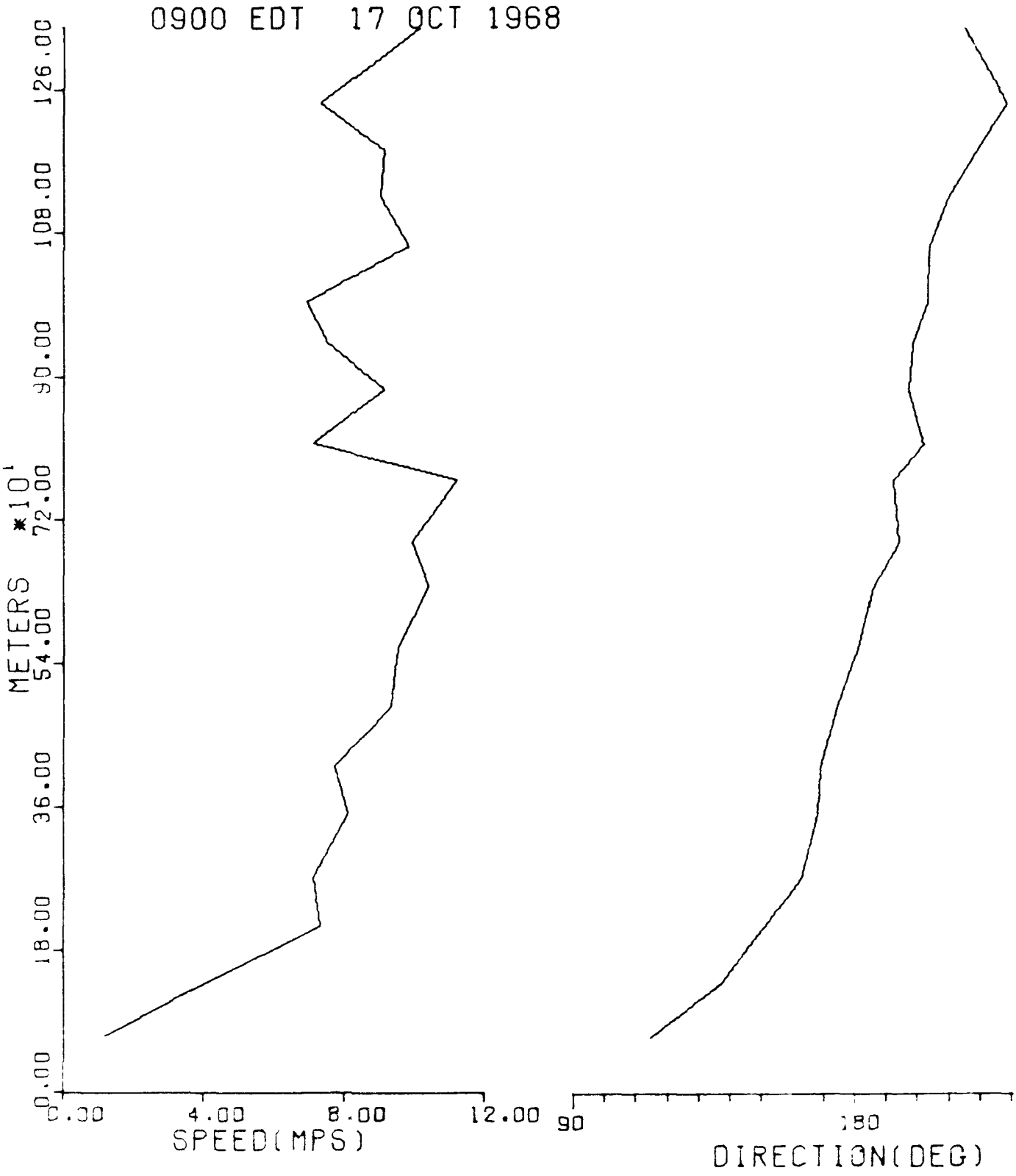

Fig. 10. NAPCA PIBAL WIND PROFILE AT KEYSTONE POWER STATION (0900 EDT - 17 Oct 1968)

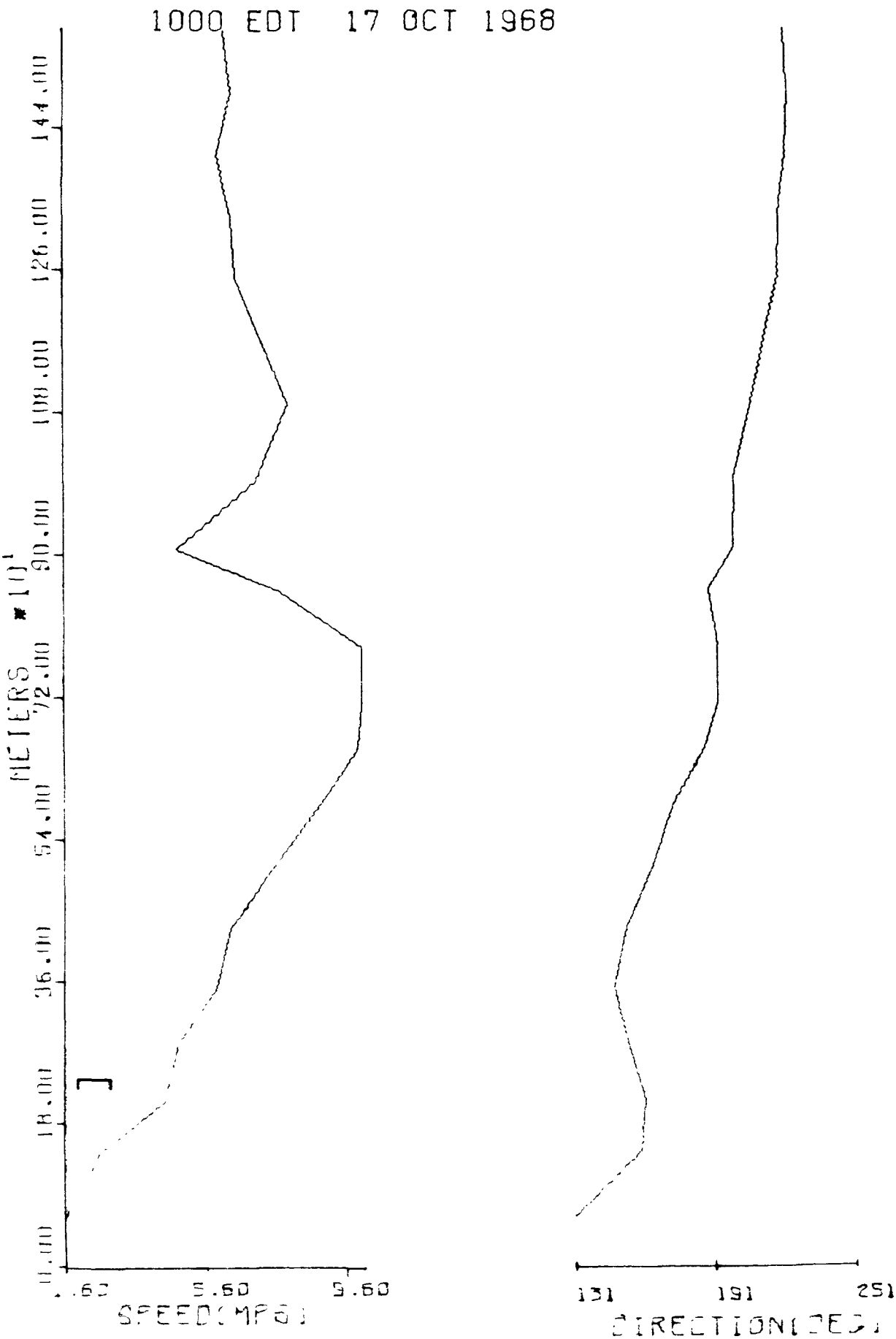

Fig. 11. NAPCA PIBAL WIND PROFILE AT KEYSTONE POWER STATION (1000 EDT - 17 Oct 1968)

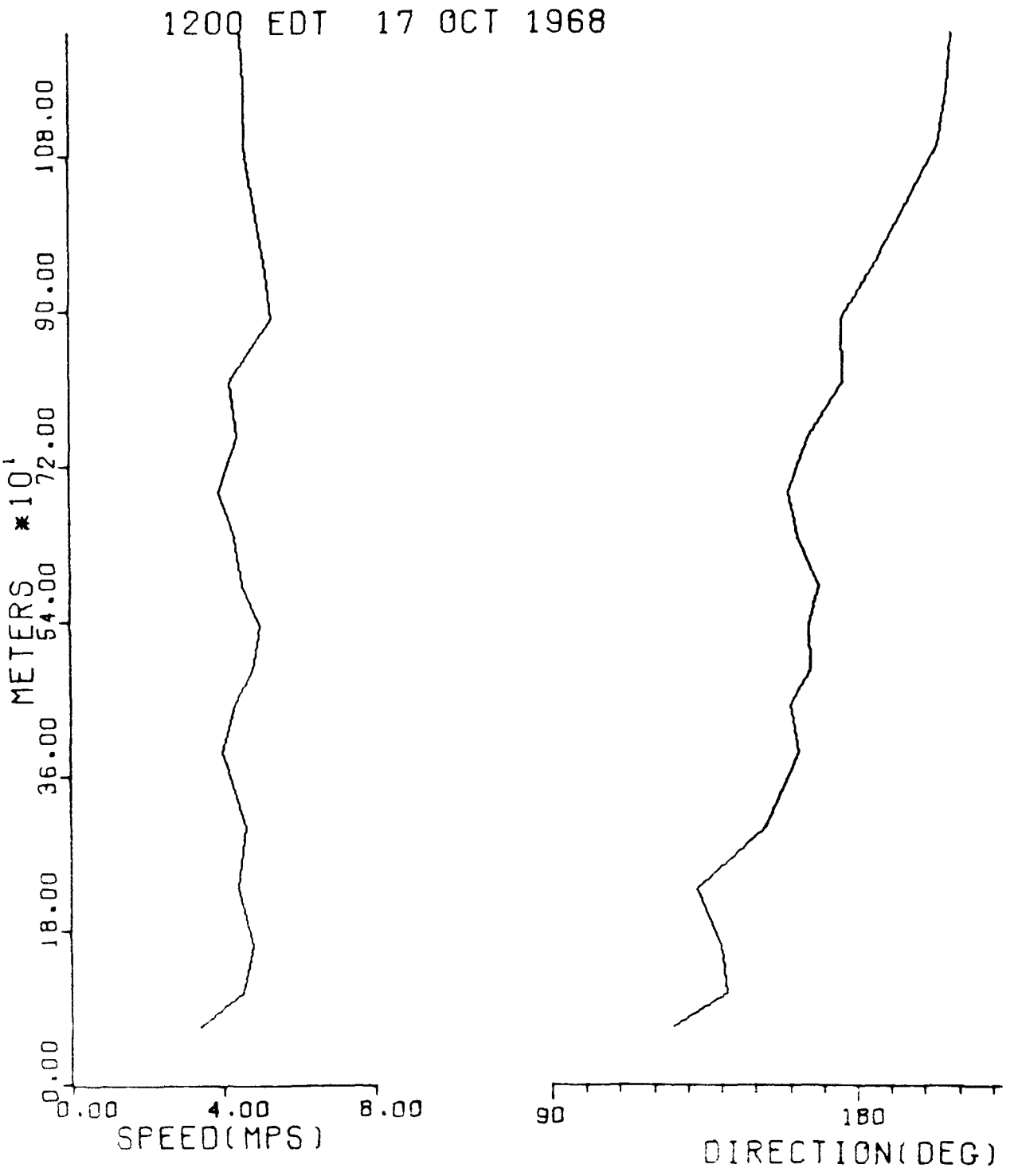

Fig. 12. NAPCA PIBAL WIND PROFILE AT KEYSTONE POWER STATION (1200 EDT - 17 Oct 1968)

Table VI

DIRECTIONAL SHEAR VALUES AND
CHARACTERISTICS FROM GROUND TO PLUME ALTITUDE

Photo Period	Date	Time Period	$\Delta\theta$ (in degrees)	Depth of Layer (in meters MSL)	Characteristics
1	10/16	1000-1110	100	----	sharp veering to 850m; then sharp backing aloft
2	10/16	1110-1130	30	----	backing to 650m; then slow veering
3	10/17	0930-1030	70	1100	veering
4	10/17	1200-1400	50	1600	veering
5	10/18	0840-0945	70	850	veering
6	10/20	1300-1400	50	2100	sharp backing to 600m; then veering
7	10/21	0840-0945	40	950	veering

Note: Altitudes are references to MSL and the stack base is 308 meters MSL

Photo Periods 1 & 2, October 16, 1968, 1000-1130 EDT

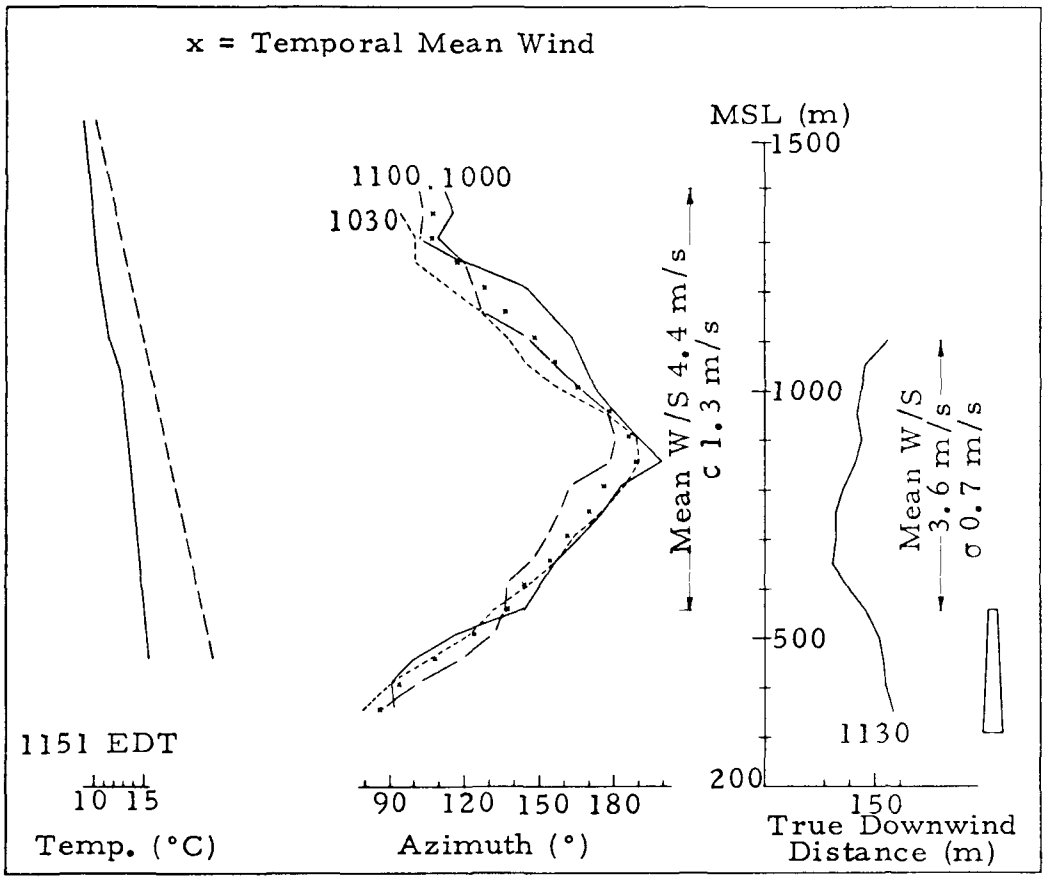

Plume Profile
Not Calculated

Fig. 13. METEOROLOGICAL ENVIRONMENT FOR PHOTO PERIODS 1 AND 2

Photo Period 3, October 17, 1968, 0930-1030 EDT, Camera Site East

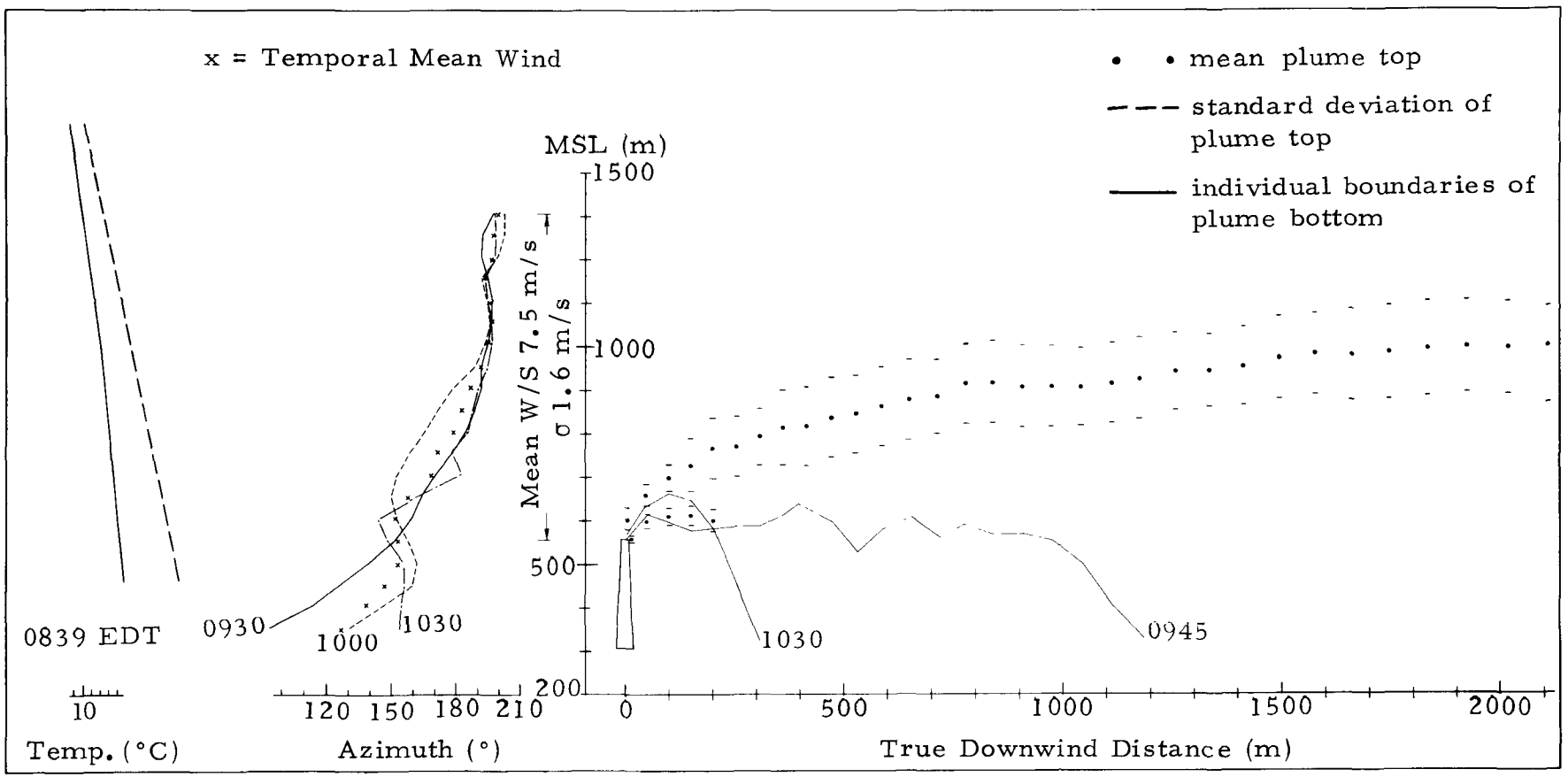

Fig. 14 METEOROLOGICAL ENVIRONMENT FOR PHOTO PERIOD 3

Photo Period 4, October 17, 1968, 1200-1230 EDT, Camera Site East, page 1

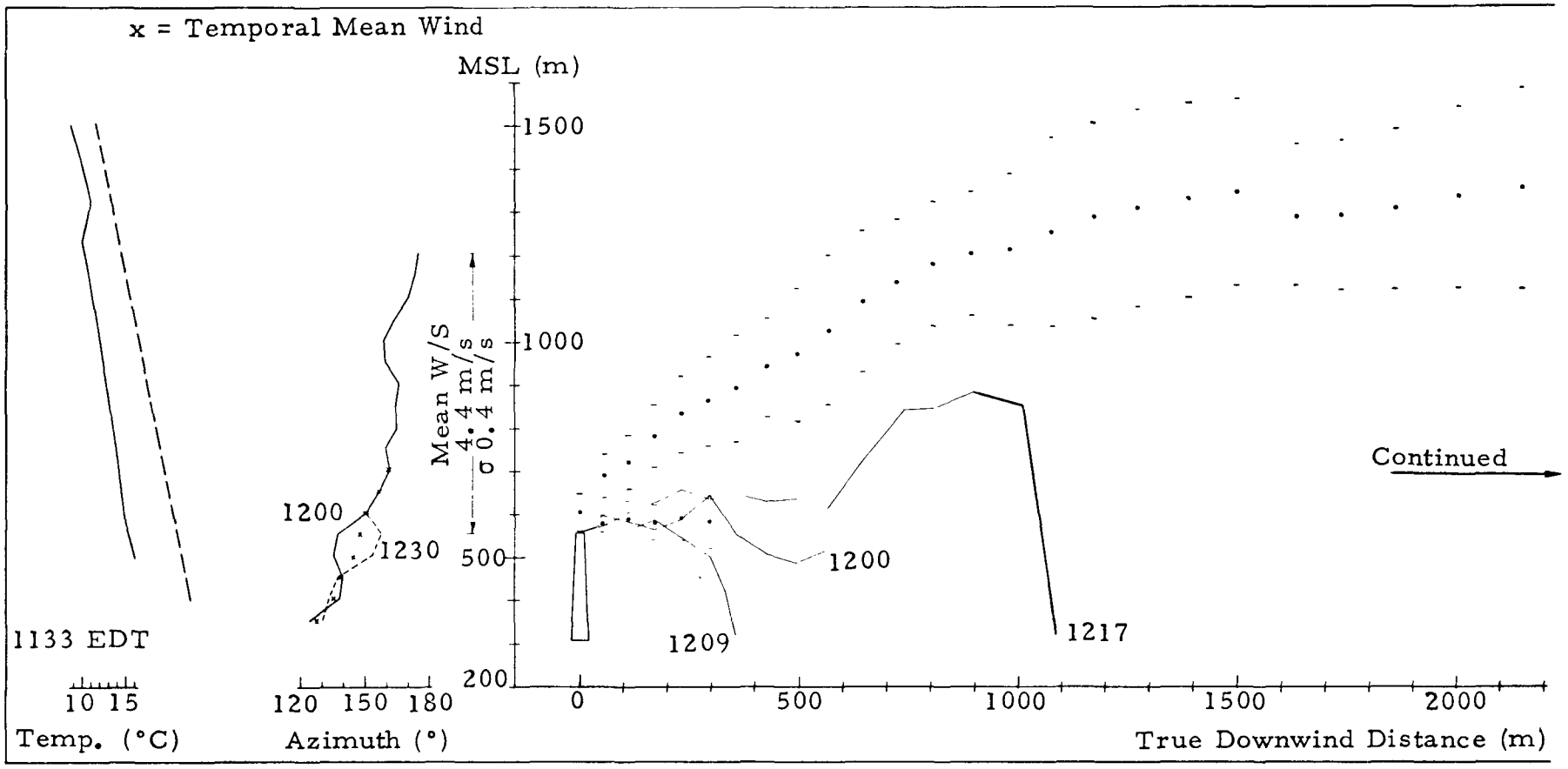

Fig. 15 METEOROLOGICAL ENVIRONMENT FOR PHOTO PERIOD 4

Photo Period 4, October 17, 1968, 1200-1230 EDT, Camera Site East, page 2

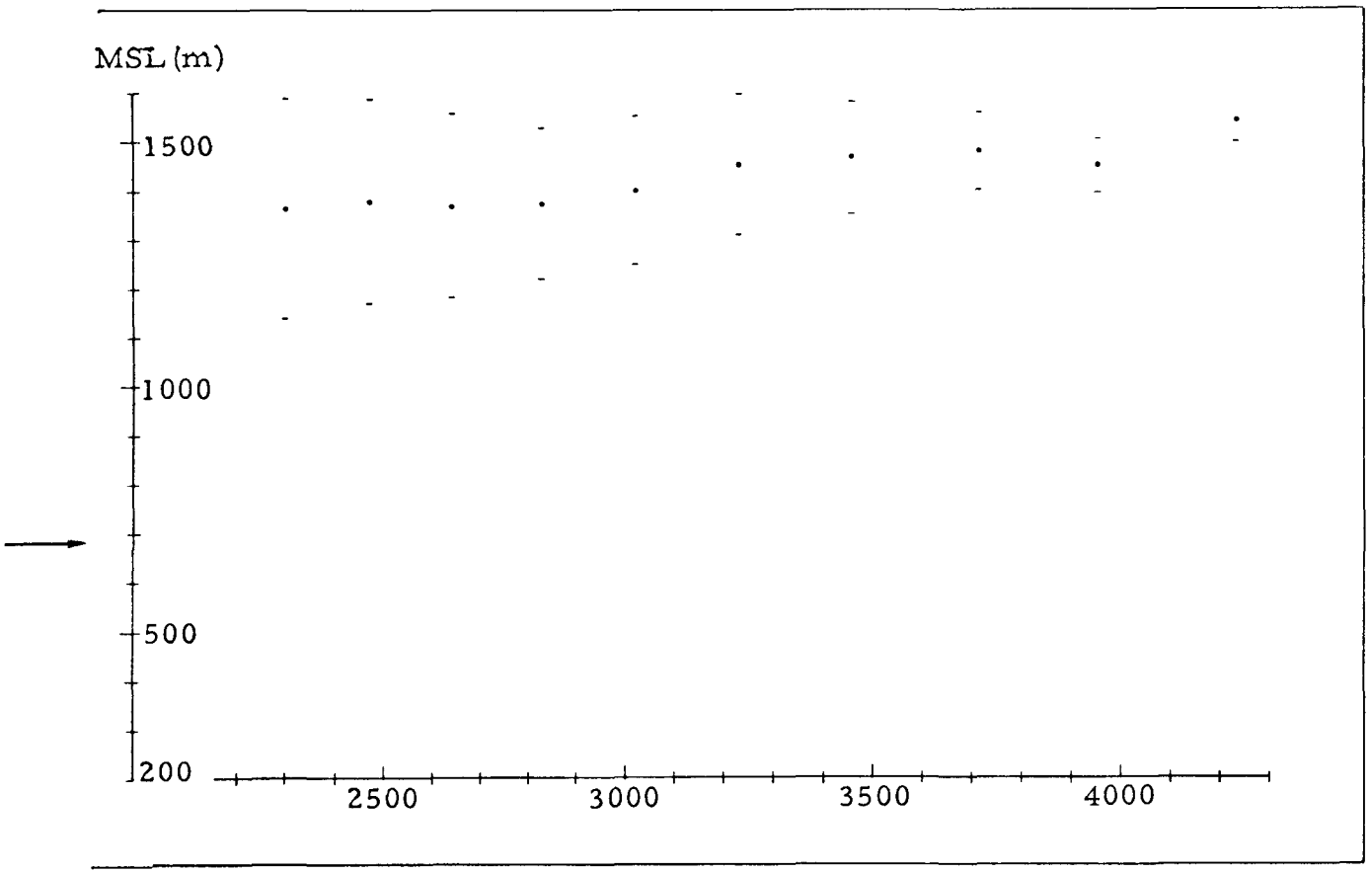

Fig. 15. (continued)

No Temperature
Profile Available

Photo Period 5, October 18, 1968, 0840-0945 EDT, Camera Site East

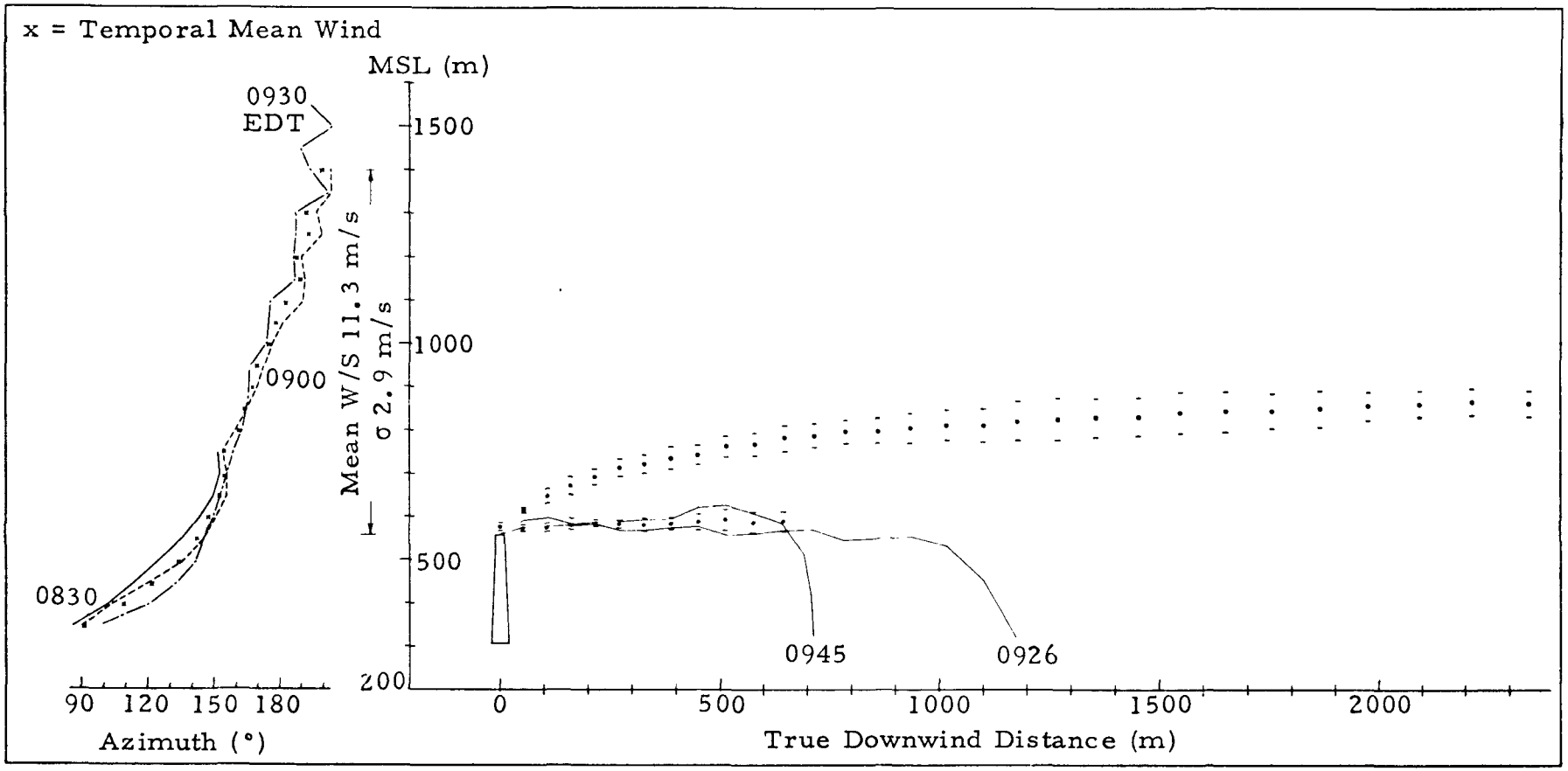

Fig. 16 METEOROLOGICAL ENVIRONMENT FOR PHOTO PERIOD 5

Photo Period 6, October 20, 1968, 1300-1400 EDT, Camera Site South, page 1

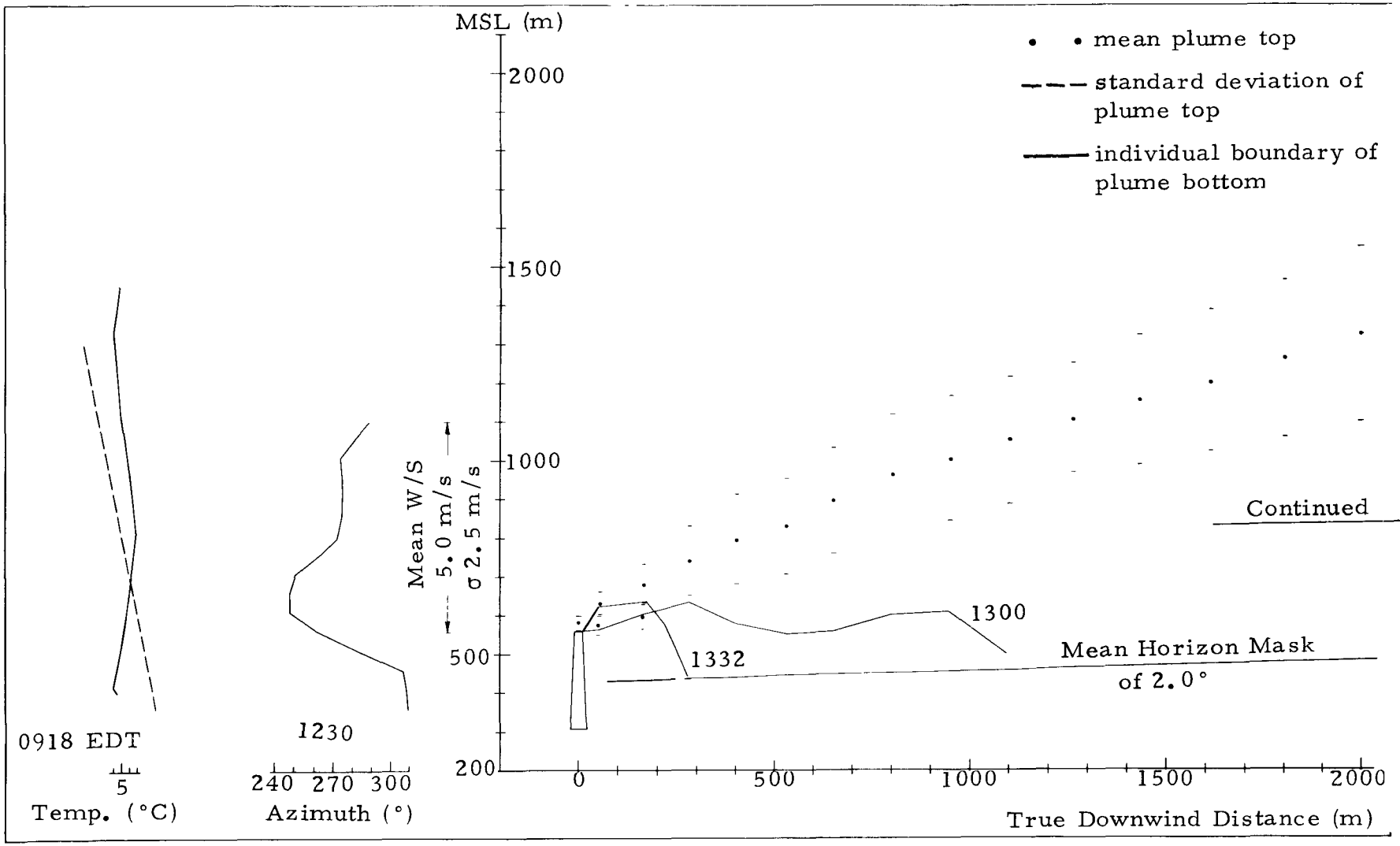

Fig. 17 METEOROLOGICAL ENVIRONMENT FOR PHOTO PERIOD 6

Photo Period 6, October 20, 1968, 1300-1400 EDT, Camera Site South, page 2

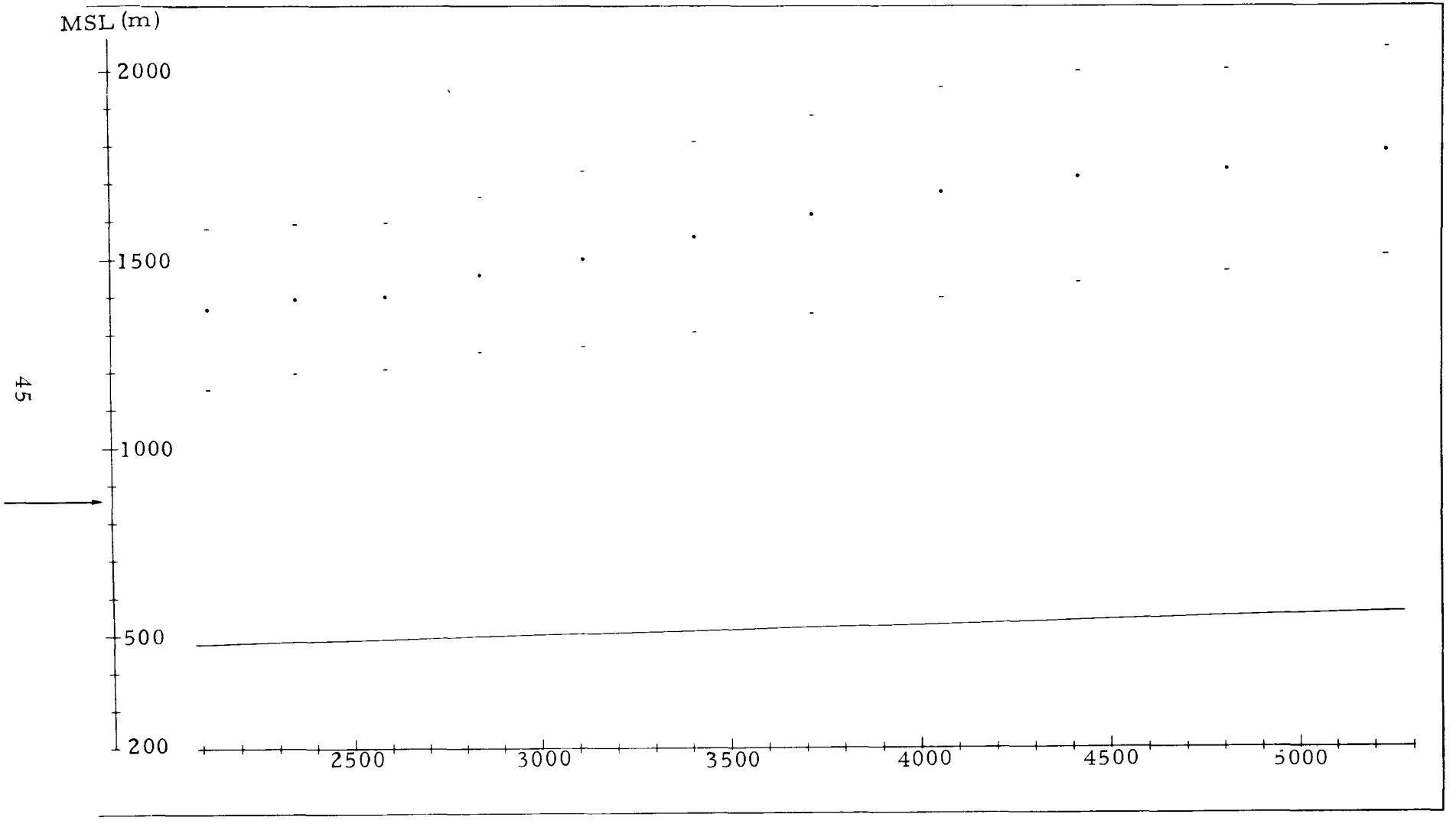

Fig. 17 (Continued)

Photo Period 7, October 21, 1968, 0840-0945 EDT, Camera Site South

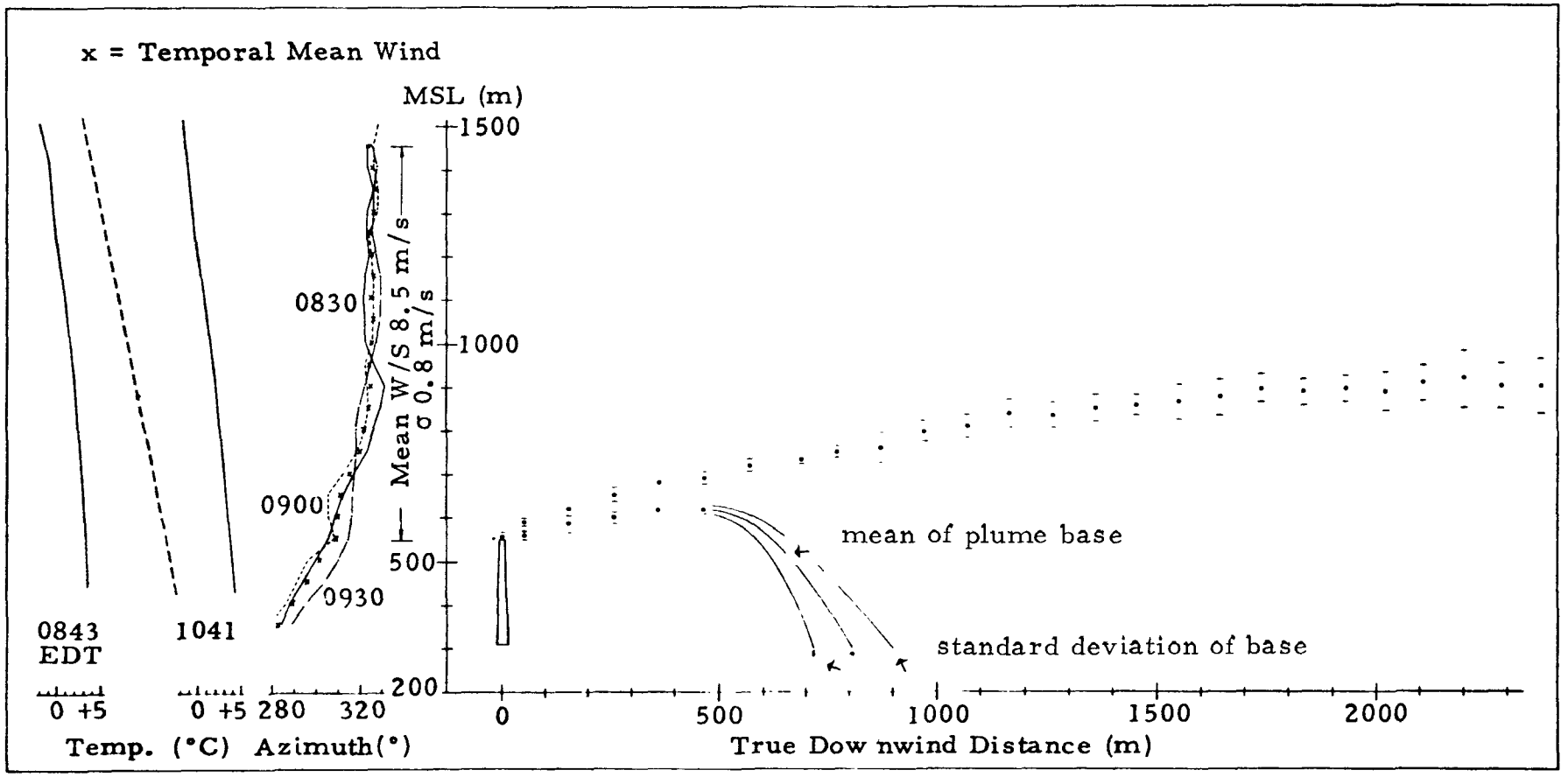

Fig. 18 METEOROLOGICAL ENVIRONMENT FOR PHOTO PERIOD 7

The variation of turbulent mixing in the vertical as a function of meteorological and topographical conditions is difficult to evaluate quantitatively in a simple, inexpensive manner for the large vertical depths and horizontal area of interest in planetary boundary layer diffusion problems. In this program, the horizontal area of interest included not only that in a 20-mile radius of the Keystone Power Station depending on wind direction, but also the nearby Homer City and Conemaugh Power Station sites which will become operational within the next few years. The MRI airborne turbulence unit, UITS, was used here to obtain a preliminary turbulence climatology of the three plant locations.

One hour prior to Photo Period 3 on October 17, there was very low turbulence in the lower layers below 1300 m MSL, corresponding to the observed strong temperature stability. Turbulence increased above 1300 m, which was above the region of principal interest. As time of day increased (e.g. Fig. 14), the stability in the lower levels decreased to more closely approximate the dry adiabatic lapse rate. Correspondingly, the turbulence values increased first in the lower levels and finally up to about 1200 m just before Photo Period 4.

At 9 a.m. on October 20, there was a strong temperature inversion ($\sim$1°C/50 m) which extended above the top of the stack to 800 m. The turbulence increased with height within the inversion, reaching a maximum at a level well below the top of the inversion. This maximum corresponded to the level of a wind velocity maximum of about 8 m/s. Wind shear below this level produced significant turbulence in spite of the strong temperature stability. Above the level of the wind maximum, the turbulence decreased again to a relatively low value.

In the morning of October 21, Photo Period 7, there was strong stability in the lower layers. A strong wind shear existed to a level of about 570 m MSL at 0830 EDT. Both above and below this level the turbulence was highly variable with altitude. This structure is typical of a stratified environment with turbulence occurring in layers intermixed with layers with almost no turbulence. By 1040 EDT, the turbulence had increased in the lower layers due to surface heating and showed a less erratic profile as might be expected in a well-mixed layer. Above 800 m, the turbulence continued to show the variable characteristics previously seen.

In areas of complex terrain, measurements of environmental conditions at one location may not be representative of the plume environment a few miles downwind. Figure 19 is an example of a 10-mile terrain-following flight made by the MRI aircraft on 20 October. The principal terrain feature was Laurel Hill, downwind of the Conemaugh

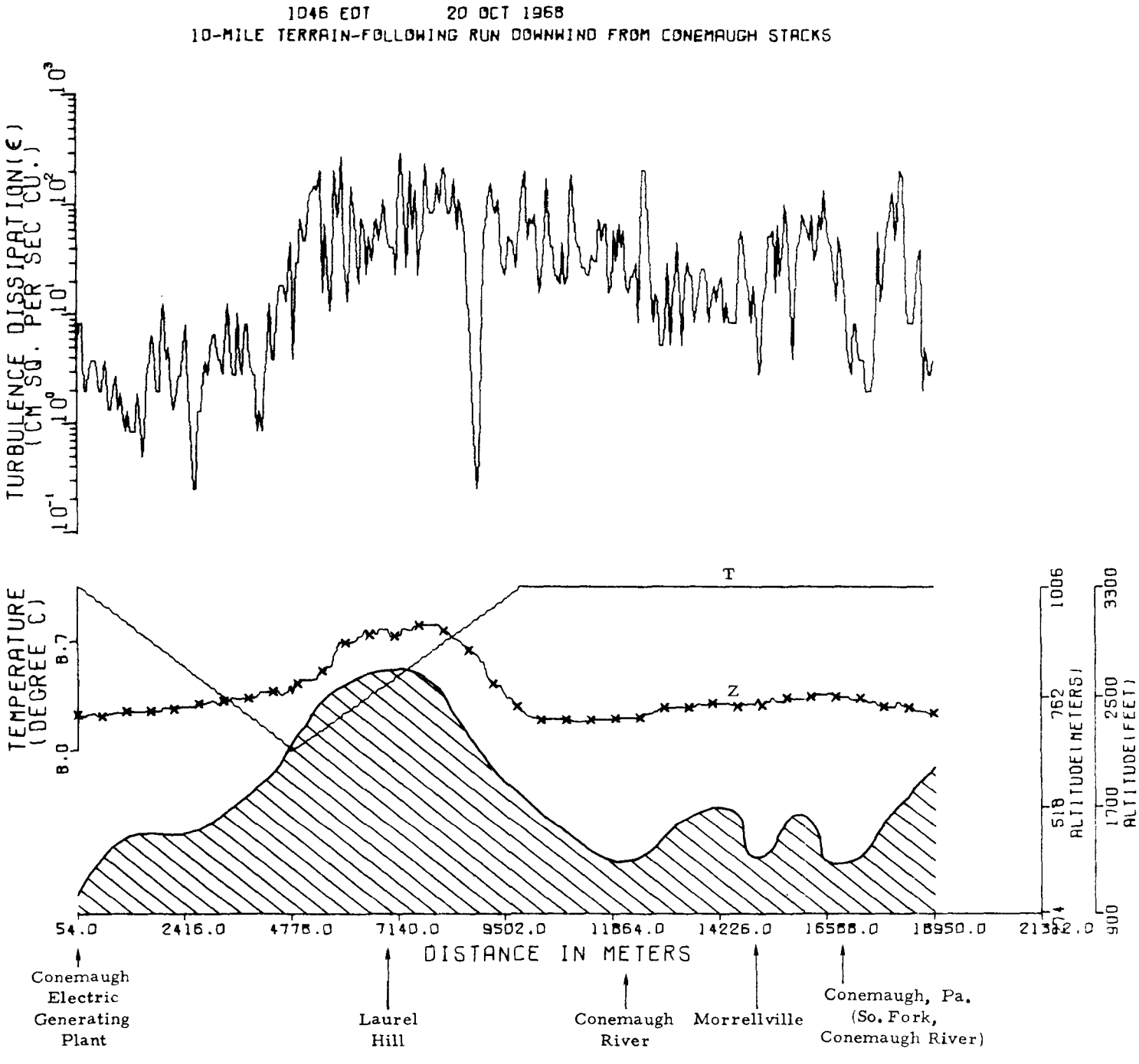

Fig. 19. 10-MILE TERRAIN - FOLLOWING RUN DOWNWIND FROM CONEMAUGH STACKS

plant. The flight path, together with temperature and ϵ values, are shown in the figure. Turbulence values increased in passing over Laurel Hill and did not return to their original values in the lee of the hill even though the windward and leeward flight altitudes were the same. It is indicated by the data that turbulence is generated by the hill and transported downwind in a slowly decaying manner.

It has been possible, on a very limited basis, to compare turbulence environments at each of the power station locations. This has been accomplished by the use of aircraft soundings made at nearly comparable times. Although unknown variations in space and time interfere with an accurate comparison, the data in Table VII suggest certain relations between stations. These data were determined as averages over 100-200 m depth of the recorded ϵ values.

Table VII

COMPARISON OF TURBULENCE VALUES (ϵ in $cm^2 sec^{-3}$)

Date	Elev.	Homer City	Conemaugh	Keystone
16 Oct	500 m	52 (1053 EDT)	45 (1115 EDT)	30 (1150 EDT)
	750	24	27	18
	1000	5	6	3.5
	1250	-	5	2.6
20 Oct	500 m	35 (1015 EDT)	4.5 (1037 EDT)	7.5 (0918 EDT)
	750	1.5	3.5	0.2
	1000	0.1	0.1	0.2
	1250	0.1	0.1	0.2
22 Oct	500 m	28 (0856 EDT)		5.5 (0843 EDT)
	750	0.4		0.6
	1000	0.2		0.2
	1250	0.2		0.2

In spite of the limited data, it would appear that turbulence at Homer City exceeds that at Keystone at least to a level of 500 m and occasionally beyond. At higher levels, there is little difference between the two sites. Conemaugh appears to be comparable to Keystone in turbulence characteristics and probably exhibits somewhat lower values in the low levels than Homer City. Data for Conemaugh were unavailable for the 22 October case.

VII. PLUME RISE AND DIFFUSION

Numerous plume rise theories exist, based primarily on empirical data. A recent review by Briggs (1969) has summarized the current state of this field. Since prior observational data have come from smaller stack heights than at the Keystone Power Station, the current program affords a unique opportunity to extend the previous work. The program also involves complex terrain, and includes cases with strong magnitude and directional shear -- all of which provide interesting but complicating aspects to the study.

The data obtained were not adequate for a comprehensive treatment of this complex subject. The program design was such that the data could only be expected to answer certain limited questions. The turbulence data did cover the appropriate air volume to some extent, but there were two important deficiencies. First, the plume turbulence was not measured really close to the stack, which is the place where the turbulence would be expected to relate most directly to plume diffusion. Second, the traverses at various altitudes and locations were not so numerous that an environmental summary could be prepared with the desired statistical significance for a particular period. In the region where fumigation was operating, turbulence data were available; but the other half of the problem, i. e. the diffusion rates and concentrations, was not covered thoroughly.

The primary diffusion data derived on this program came from the photogrammetric analysis of the time lapse pictures of the plume. These do seem quite useful. Sequences of 35-mm photos were obtained by MRI on seven days of the program. Photogrammetric analyses were carried out for five of these days, using the techniques described in Appendix A. The results are presented pictorially in Figs. 14-18, and numerically as well as pictorially in the data supplement. In the written evaluation, each photograph was treated individually so that a time sequence of the plume behavior would be obtained. Plume dimensions were then averaged over groups of photos on the basis of similarity in meteorological conditions and plume behavior. This permitted the identification of downwind regions where fumigation occurred and provided details of the transitional stages leading to fumigation.

The field program was conducted so that plume altitude data could be obtained from aircraft observations. It was therefore possible to verify the accuracy of a portion of the photogrammetric data and to extend the plume rise data much farther downwind than is usually possible with photographic observations. The aircraft data used in the plume analyses were those cases when the aircraft was approaching the plume from the right-hand side (looking downwind) and when the aircraft observer reported

a good penetration of the centerline of the plume. Aircraft data plotted in subsequent figures are the mean of two or three successive traverses.

Figures 20-24 show plotted plume data for the three photo periods which have been analyzed. Top and mean centerline of the plume are given in the figures. Vertical and downwind distances have been plotted in terms of the non-dimensional expressions x/ℓ and z/ℓ where:

$$\ell = \frac{F}{u^3} \tag{10}$$

with u = wind speed and F = "flux of buoyancy" in units $m^4\ sec^{-3}$.

$$F = W_o\ R^2\ g\ \frac{T_g - T_A}{T_A} \tag{11}$$

and is related to the stack parameters by the terms:

W_o = stack exit velocity
R = radius of stack
g = acceleration of gravity
T_g = temperature of the exit gas
T_A = temperature of the ambient air.

This type of normalization is discussed by Briggs (1969) who was able to coalesce a variety of experimental cases together rather effectively by this method.

It is possible in Figs. 20-24 to identify three distinct downwind regions of plume behavior: (a) no fumigation, (b) intermittent, and (c) continuous fumigation. The distinguishing feature of region (b) is that the downwind distance to the intersection of the cloud and the ground varies with time.

The plume rises are first examined here without regard to the meteorological environment, except to the extent the environment is involved in the normalizing procedure of Eqs. (10) and (11). The non-fumigation regime is considered initially.

It has been customary to express the rise in the mean height of the plume in terms of a power law:

$$\frac{\Delta h}{\ell} = a\left(\frac{x}{\ell}\right)^n \tag{12}$$

October 17, 1968

z_T and $\bar{z}$ are referenced to stack base

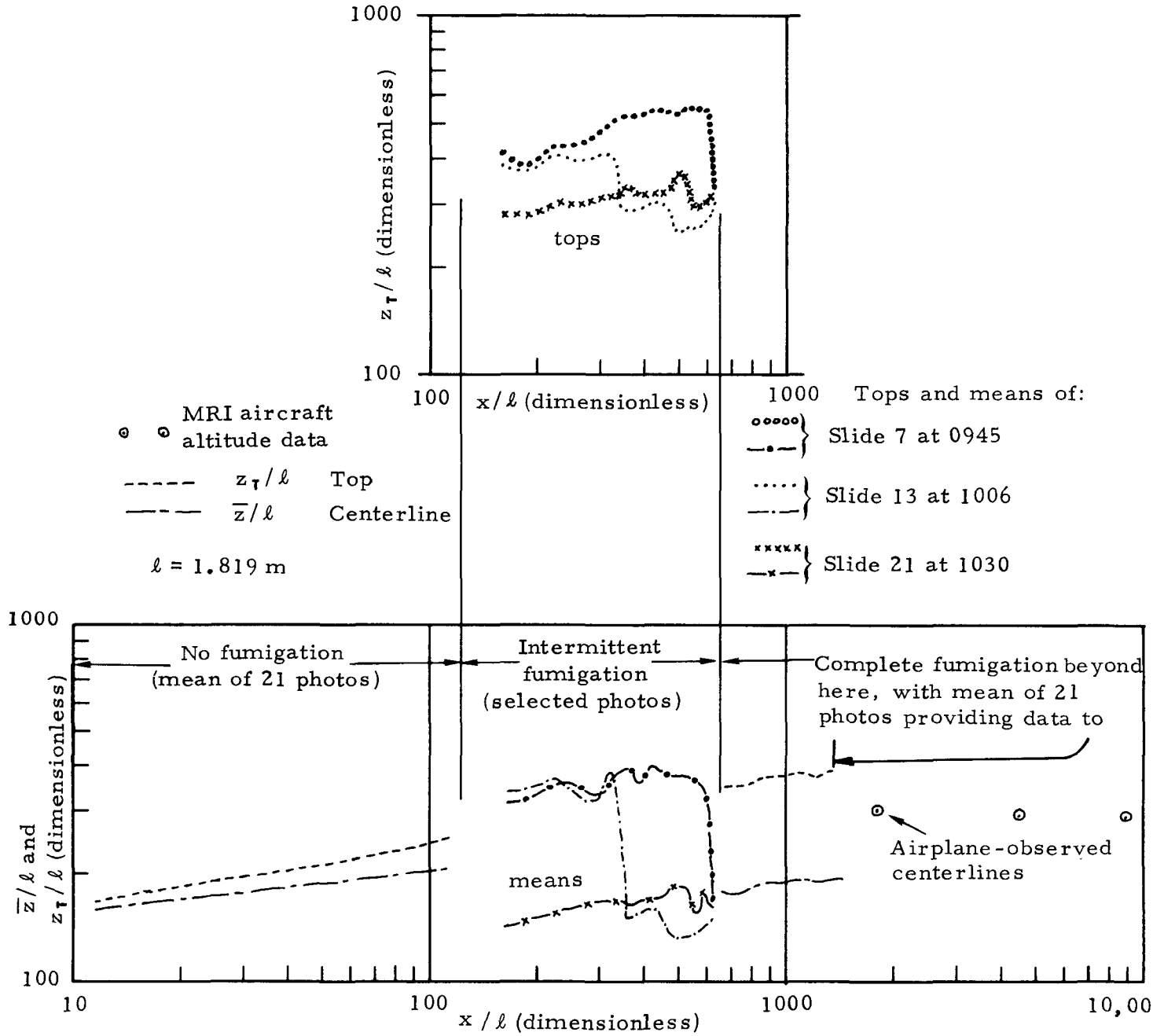

Fig. 20. NON-DIMENSIONAL PLUME RISE (TOP AND MEAN CENTERLINE) FOR PHOTO PERIOD NUMBER 3

October 17, 1968

z_T and $\bar{z}$ are referenced to stack base

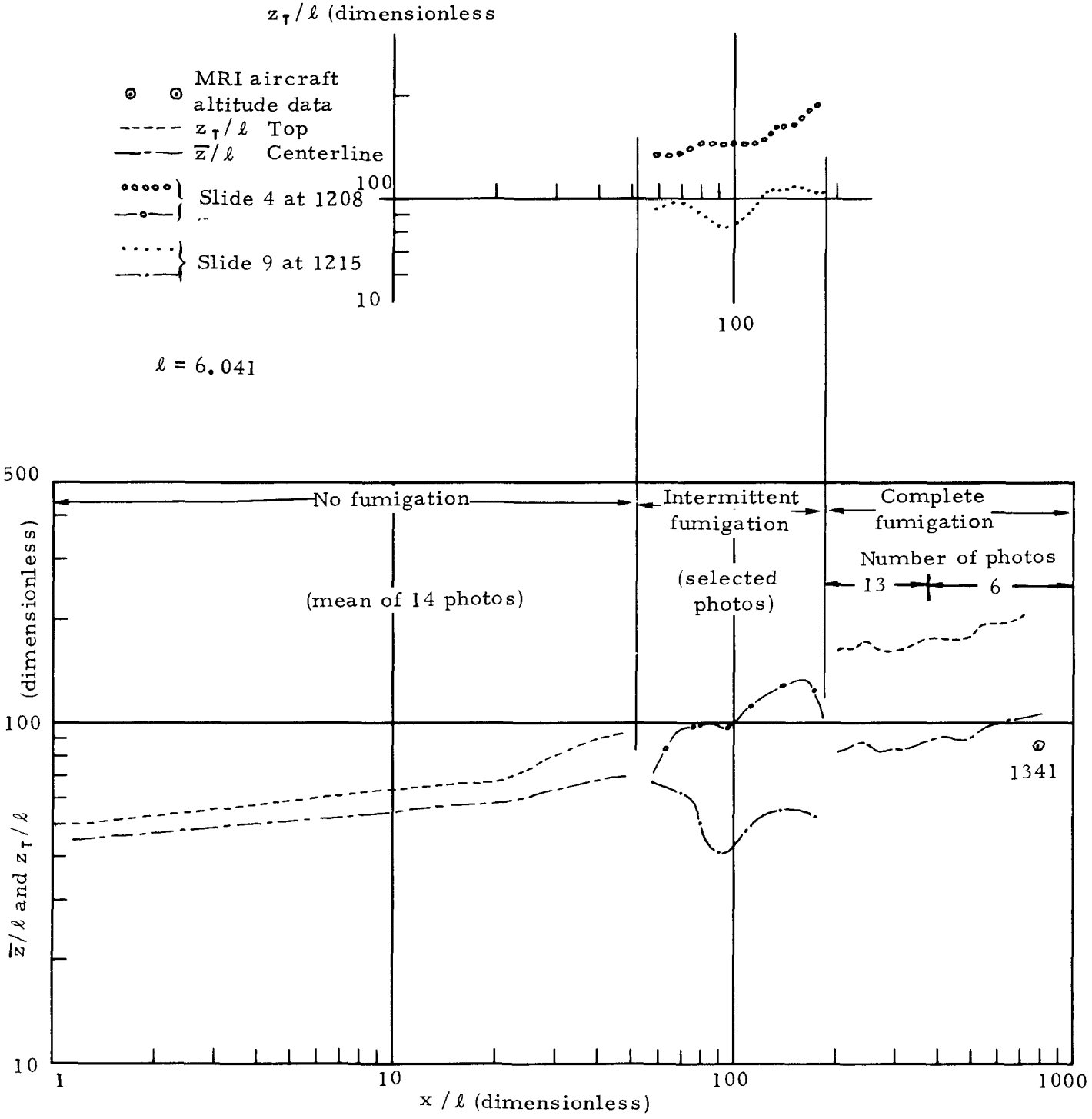

Fig. 21. NON-DIMENSIONAL PLUME RISE (TOP AND MEAN CENTERLINE) FOR PHOTO PERIOD NUMBER 4

October 18, 1968

z_T and $\bar{z}$ are referenced to stack base

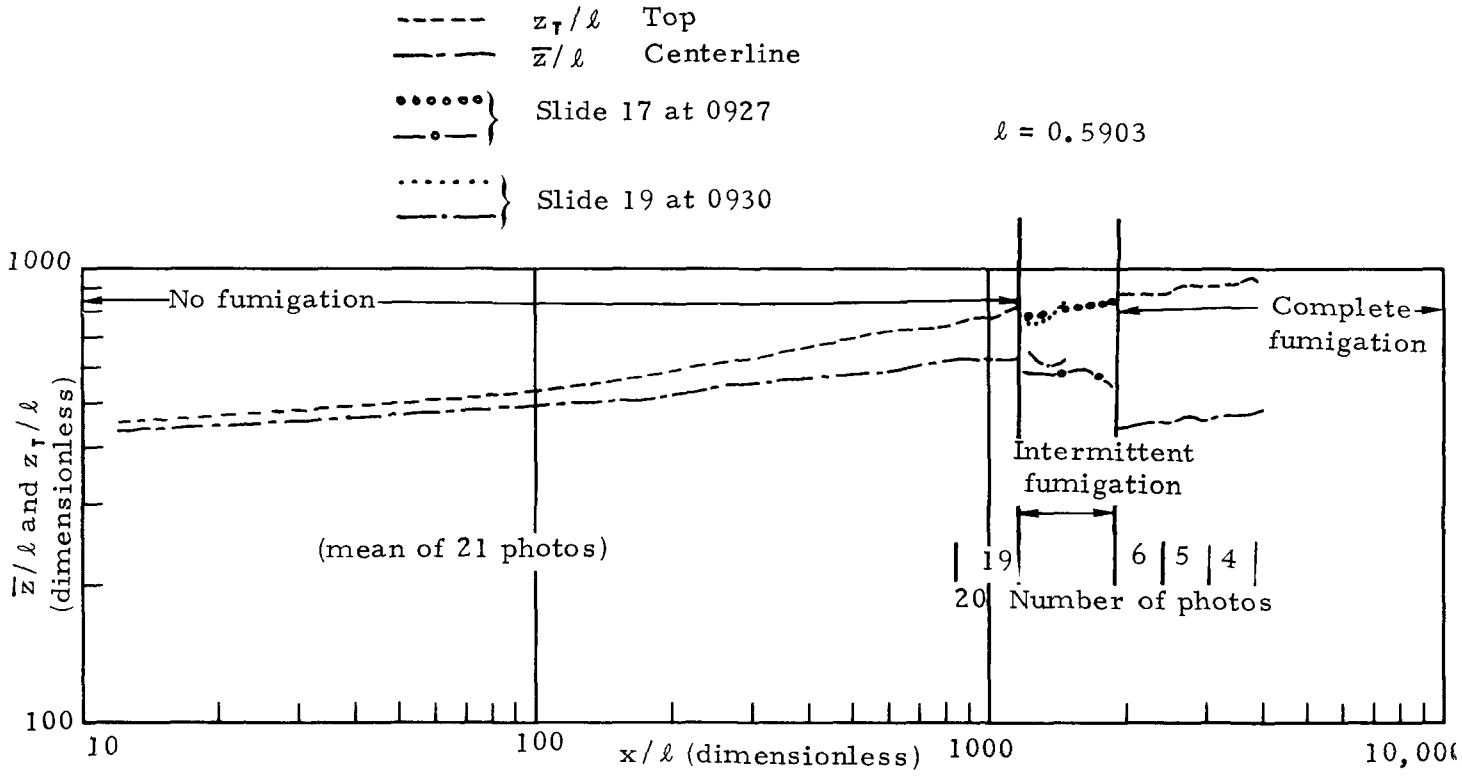

Fig. 22. NON-DIMENSIONAL PLUME RISE (TOP AND MEAN CENTERLINE) FOR PHOTO PERIOD NUMBER 5

October 20, 1968

z_T and $\bar{z}$ are referenced to stack base

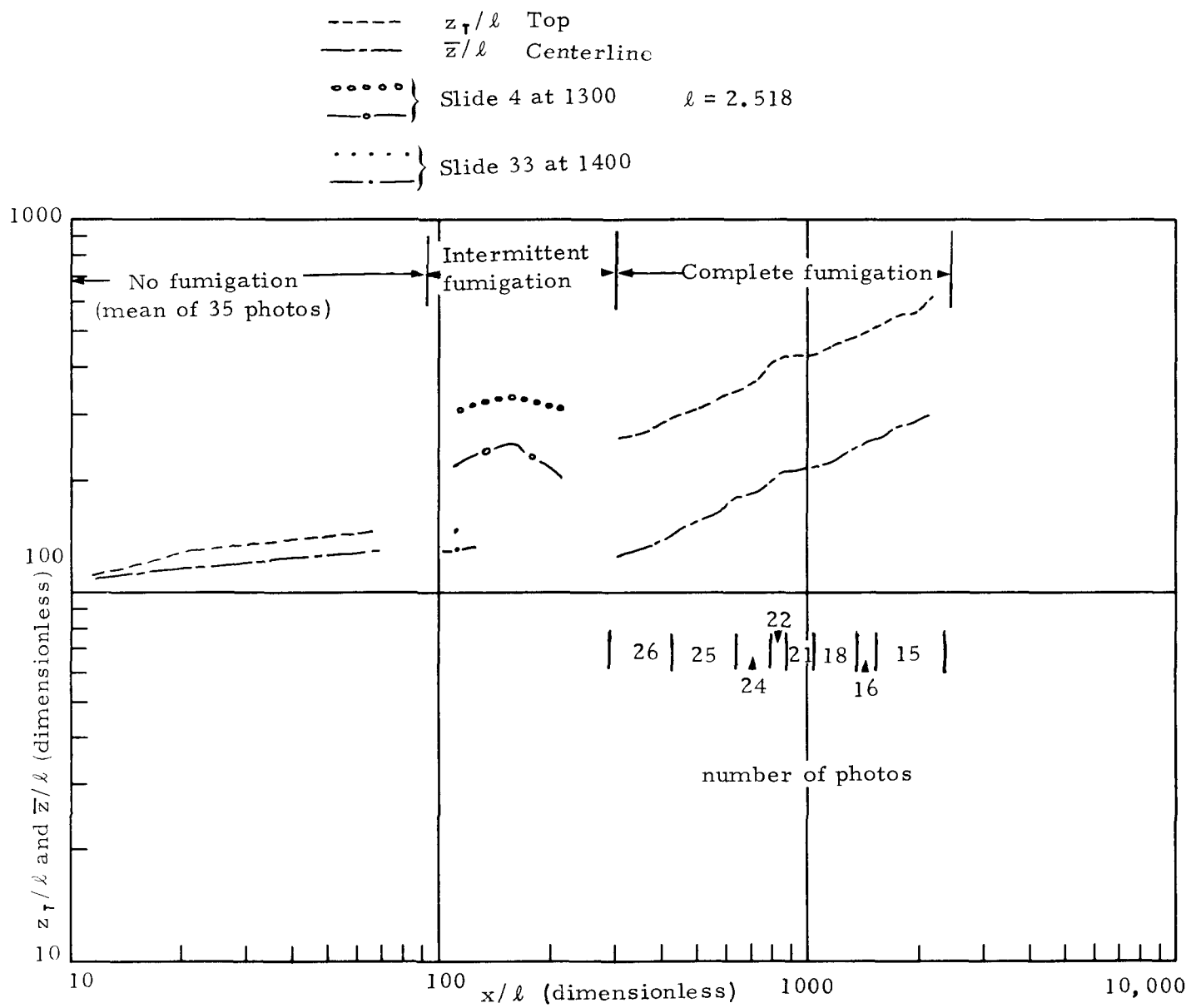

Fig. 23. NON-DIMENSIONAL PLUME RISE (TOP AND MEAN CENTERLINE) FOR PHOTO PERIOD NUMBER 6

October 21, 1968

z_T and $\bar{z}$ are referenced to stack base

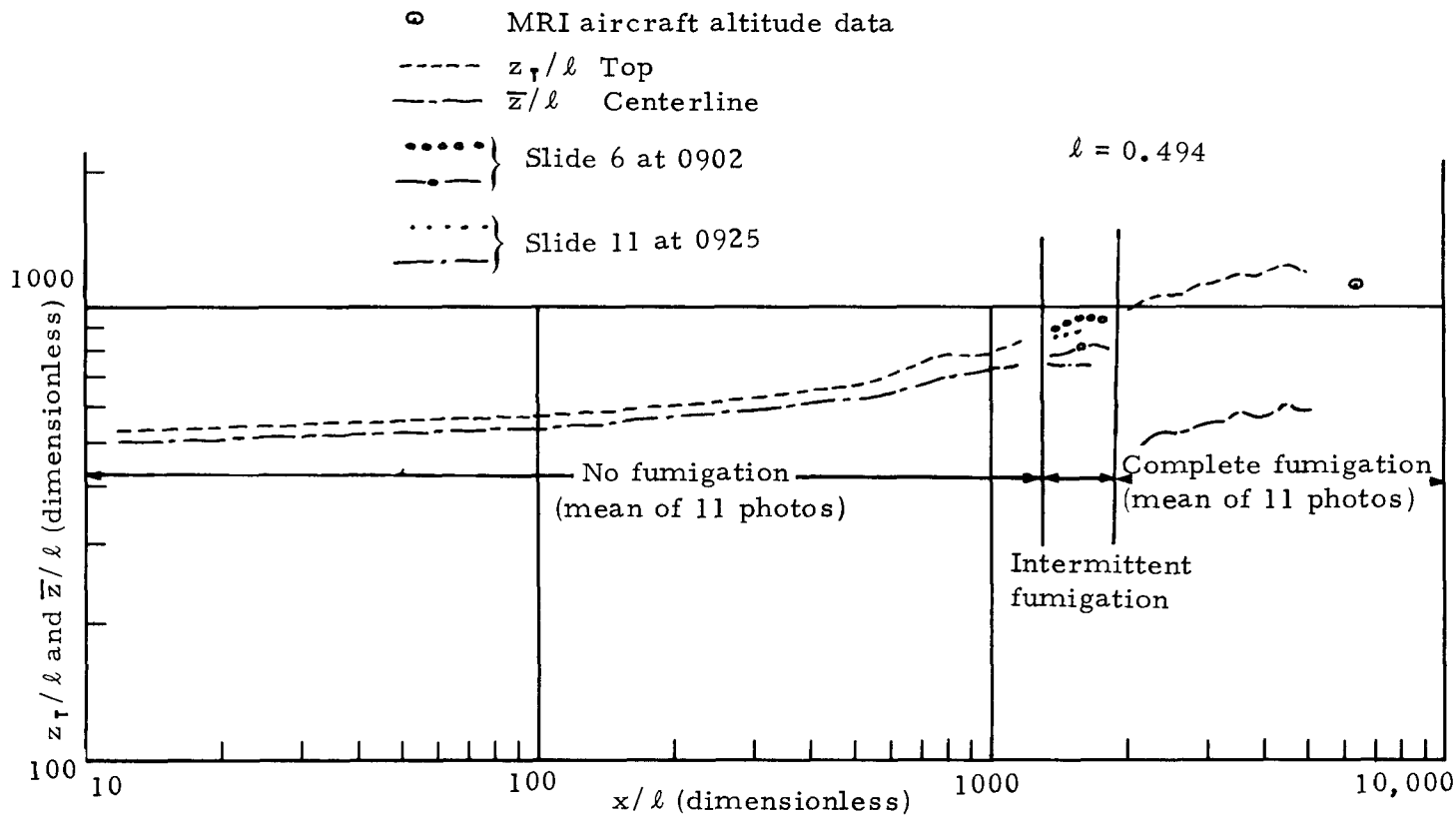

Fig. 24. NON-DIMENSIONAL PLUME RISE (TOP AND MEAN CENTERLINE) FOR PHOTO PERIOD NUMBER 7

if the distances are expressed in dimensionless form and where Δh is the height above the top of the stack, and a, n are empirical constants. Slawson and Csanady (1967), among others, suggested that:

$$\Delta h = 2.3\, \ell^{1/3} x^{2/3} \tag{13}$$

or

$$\frac{\Delta h}{\ell} = 2.3 \left(\frac{x}{\ell}\right)^{2/3}$$

in dimensionless form was appropriate for near-neutral conditions where ℓ is the length scale of buoyancy. Murthy (1968) suggested that the value of n should be reduced in the case of vertical wind shears (velocity shears) in accordance with the following:

$$n = \frac{2}{3(1+p)} \tag{14}$$

where p is the exponent on the wind profile power law:

$$\frac{u}{u_0} = \left(\frac{z}{z_0}\right)^p \tag{15}$$

Keystone data were analyzed in two separate regions: no fumigation, and continuous fumigation. Data for the no-fumigation region are shown in Figs. 25 and 26 (two separate figures being used for clarity). Non-dimensional heights of the plume centerline above the stack are plotted against non-dimensional downwind distances. The first plume height observation has been entered in the plots at a downwind distance of $x/\ell = 1$.

It can be seen in the figures that a straight line through the downwind points does not pass through the initial plume observation point at $x/\ell = 1$. In addition, $\Delta z/\ell$ has finite and non-zero values at $x/\ell = 1$ which can be taken as the stack location for all practical purposes. a and n values (Eq. 12) were calculated from Figs. 25 and 26 as shown in the following table.

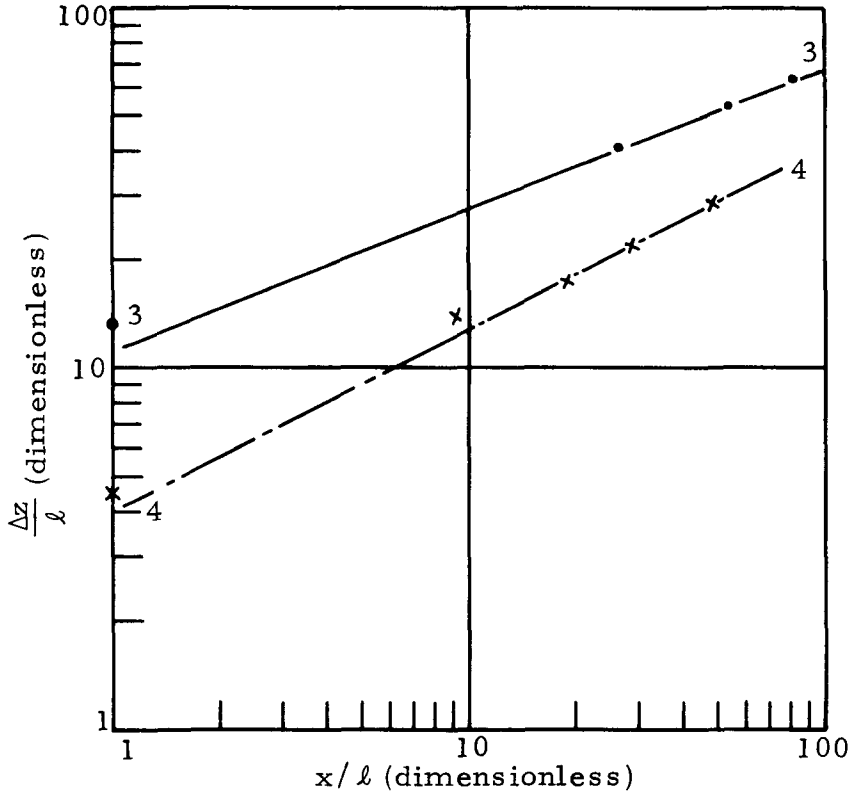

Fig. 25. CENTERLINE GROWTH ABOVE STACK TOP

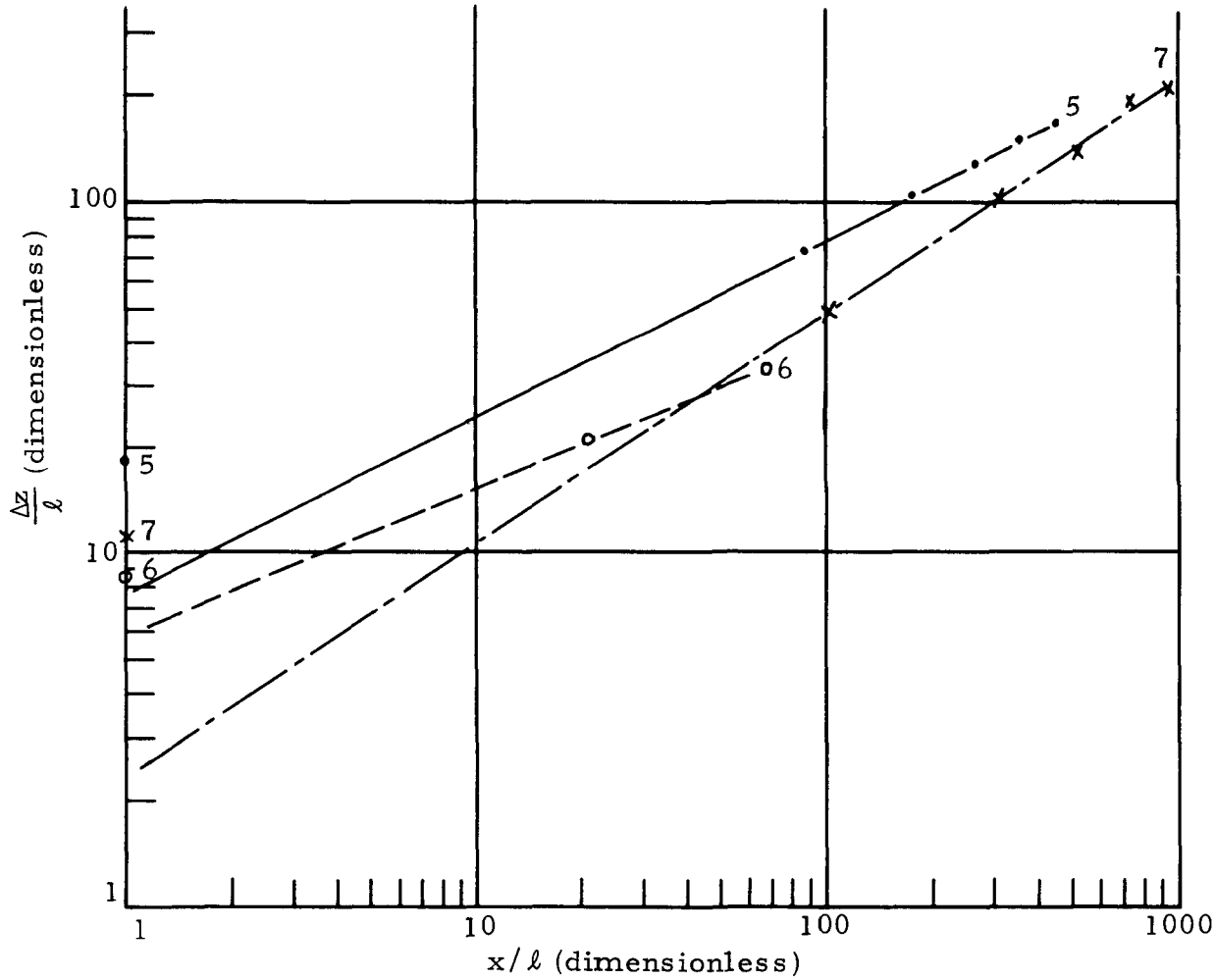

Fig. 26. CENTERLINE GROWTH ABOVE STACK TOP

Table VIII

PLUME RISE PARAMETERS - NO FUMIGATION

Photo Period	a	n	ℓ	$\frac{\Delta h^*}{\ell}$	Δh^*
3	11.0	.388	1.8 m	2.2	4.0m
4	4.1	.477	6.0	0.5	3.0
5	7.6	.506	0.6	11.0	6.6
6	6.0	.405	2.5	2.6	6.5
7	2.4	.656	0.5	8.8	4.4

* Δh refers to vertical distance between first observational point and virtual source of plume as defined by straight-line extension of downwind points (Figs. 25, 26). It is assumed that this distance is a manifestation of the initial stack momentum which is quickly dissipated by mixing, after which the buoyancy effects dominate.

Table VIII shows that n values for the five photo periods are generally less than the 0.67 value suggested by Slawson and Csanady (1967).

An attempt was made to calculate wind shear values for the various photo periods shown so that Murthy's modification of the 2/3 power law could be evaluated. Exponents α and β in the following power laws were calculated from the wind profile data:

$$u(z_2) = u(z_1)\left(\frac{z_2}{z_1}\right)^{\alpha} \tag{16}$$

$$\theta(z_2) = \theta(z_1)\left(\frac{z_2}{z_1}\right)^{\beta} \tag{17}$$

where u is the pibal wind speed, θ is the wind direction and the two heights z_1 and z_2 are 100 and 600 meters above ground. Rate of change of speed and direction were also calculated as follows:

$$Q = \frac{\Delta \bar{u}}{\Delta z} \quad \text{between } z_1 \text{ and } z_2$$

$$\Psi = \frac{\Delta \theta}{\Delta z} \quad \text{between } z_1 \text{ and } z_2.$$

Table IX shows the results of the calculations.

Table IX

WIND PROFILE SHEAR PARAMETERS
CORRESPONDING TO PLUME RISE DATA

Photo Period	Date 1968	Pibal Launch Time	α dimension-less	β dimension-less	Q per sec	Ψ deg. per meter
3	Oct. 17	0930	1.9	3.5	0.012	0.158
		1000	1.3	1.2	0.013	0.048
		1030	0.8	8.1	0.015	0.074
4	Oct. 17	1200	29.4	6.3	0.001	0.082
		1230	16.6	10.9	0.001	0.050
5	Oct. 18	0830	1.3	3.5	0.012	0.152
		0900	1.2	4.0	0.017	0.120
		0930	1.3	5.0	0.016	0.102
6	Oct. 20	1230	0.6	6.0	0.011	0.144
7	Oct. 21	0830	10.9	19.8	0.003	0.056
		0900	0.9	19.8	0.017	0.060
		0930	12.7	24.8	0.010	0.048

Values of the power law exponents are unusually large and variable in Table IX and it was concluded that insufficient data existed for the application of Murthy's suggestion. Such large values may be the result of the hollow in which the Keystone plant is located which reduces the low level wind values and either increases or leaves unmodified the wind at higher altitudes. The data in the table indicate that large shear values in both speed and direction are likely to occur at the site and it is not unreasonable to expect, on this basis, that the n-values in Table VIII would come out to be less than 0.67.

Now we turn to centerline plume growth in the regime of complete fumigation. As noted before, z/ℓ data were plotted as a function of downwind distance x/ℓ. Here, height of the centerline was arbitrarily defined as one-half of the distance from the ground to the plume top. At such large downwind distances, the plume resembles a ground point-source cloud, with base limited by the ground surface but with the top able to grow upward due to diffusion. For this reason, z/ℓ was measured, in this case, with reference to the base of the stack rather than the stack top. This permitted comparison of the growth with standard point source data at large downwind distances.

Table X shows the values of n calculated from the region of complete fumigation (x/ℓ between 1000 and 7000):

Table X

PLUME RISE PARAMETERS - COMPLETE FUMIGATION

Photo Period	Time	n	Centerline Height at 2 km (above stack height)
3	0945	.120	350m
4	1208	.207	530
5	0927	.117	280
6	1300	.439	500
7	0902	.246	290

In contrast to the data shown in Table X, corresponding power law growth values from standard diffusion estimates (σ_z) are n = 1.07, 0.92 and 0.62 for stability categories B, C and D, respectively. The low values of n in Table X indicate that the plume (except in Period 6) had reached nearly to the top of the mixing layer and that an asymptotic value for the top height was being approached. Considerable upward growth still existed in Period 6 at the large downwind distance. The effect of time of day is clearly seen in the table where the centerline height for the two mid-day periods far exceeds the early morning heights.

We now consider the interrelation between turbulence (and larger scale convective motions) and the diffusing plume. The simplest approach is to note that soundings of the turbulence meter can quickly delineate the general regions of turbulent mixing. ϵ profiles for the cases here typically show high values, corresponding to good mixing, near the ground, decreasing to low values at some elevation of the order of 700 - 1500 m above the ground. Clearly, such soundings show the level to which mixing can diffuse material rapidly. The height of the "lid" increases from early morning to afternoon.

Table XI shows the depth of the mixing layer obtained from ϵ profiles compared to the observed top of the smoke plume at some distance downwind of the plant.

Table XI

MIXING LAYER DEPTHS (MSL)

Photo Period	Time	Top Cloud	Downwind Distance	Top Mixing Layer (ϵ)	Avg. ϵ
3	0930-1030	1000 m	2 km	800 m	50 cm^2/sec^3
4	1200-1400	1600	2	1350	6
6	1300-1400	1500	2	1000 (at 1037)	3
		2000	5		
7	0840-0945	950	2	700 (at 0856)	15
				800 (at 1040)	

Table XI shows that the mixing layer depth derived from the ϵ profile is slightly lower than the top of the smoke plume. This is to be expected with a huge, buoyant plume. The variations in depth are satisfactorily portrayed. It should be noted that the plume measurements for Photo Period 6 were taken three to four hours after the sounding data at which time it might be expected that the mixing layer would have increased beyond the depth shown by the ϵ profile.

There are several ways in which ϵ data may be used to help predict diffusion beyond the simple box-model discussed above. The first involves diffusion in the inertial subrange.

$$\sigma_r^2 = c\epsilon t^3 \qquad (18)$$

where σ_r is some characteristic dimension of the plume cross-section, c is a dimensionless constant of order unity, and t represents a time beginning when the expanding cloud is very much smaller than when it is subsequently observed. See MacCready (1964b) for background on applicability. Although it is not rigorous, this predictive technique may be helpful in the non-fumigation stage. It is unsuitable for later stages, for then vertical meandering will cause a difference between absolute diffusion (long-time averaging) and the relative diffusion for which Eq. (18) can fit; and also the cloud will be getting large compared to inertial subrange scales. In the present program, ϵ was not measured in the plume in the main non-fumigation region and so the technique is inapplicable. In order to grow a cloud to 200 m diameter in 30 seconds, as is the case at the Keystone Power Plant, Eq. (18) shows ϵ would be several thousand cm^2 sec^3, which constitutes extreme turbulence for airplane flight. To examine the points further, note that Hoult, Fay, and Forney (1968) have shown that atmospheric environmental turbulence is relatively unimportant

compared to the plume turbulence for plumes from high stacks reaching up to their equilibrium heights. This was found valid to distances ten times the stack height, hence here beyond 2 km and beyond the typical non-fumigation regime. In summary, turbulent observations appropriate to the early plume must be made in the plume.

The other techniques for applying ϵ to vertical diffusion prediction involve calculating, empirically, the diffusing capability for large eddies from the ϵ value which pertains to small eddies. There are two approaches. For one, we obtain the value of σ_{300} where this is the "sigma meter" value for vertical turbulence for eddies smaller than 300 seconds A relationship between σ_{300} and diffusion categories can then be used, as given by Slade (1965), or direct formulas can be applied, as reviewed by Pasquill (1962). One can estimate σ_{300} by a two-stage procedure.

$$\sigma_{30} = 5.02\ U_0^{-2/3}\ \epsilon^{1/3} \tag{19}$$

where σ_{30} pertains to eddies below 30 seconds, and U_0 is the wind speed. This inertial subrange equation comes from MacCready and Jex (1964). Then

$$\sigma_{300} = \sigma_{30} \times \left(\frac{300}{30}\right)^{1/5} \tag{20}$$

which is the so-called "1/5th power law" assumed by Cramer, et al. (1964).

The second approach is given by Hanna (1968):

$$K_z = 0.06\ \epsilon^{1/3}\ k_m^{-4/3} \tag{21}$$

where ϵ is given in m^2/sec^3, k_m is the wave number of maximum turbulent energy in units of m^{-1}, and K_z is the vertical exchange coefficient. The two terms in Eq. (21) express the concept that the diffusive power of the atmosphere is a fraction of the magnitude of turbulent energy (ϵ) and a measure of the scale of the turbulent motions (k_m). The UITS measures a portion of the required information, i.e., ϵ. Hanna (1968) has developed a nomogram for the estimation of k_m, based on stability (R:), height above ground, and wind speed. Use of Eq. (21), together with Hanna's nomogram for k_m yields K_z estimates which can be used in a standard diffusion equation

$$\sigma_z^2 = 2\,K\,t. \tag{22}$$

When the two preceding methods (σ_{300} and K_z) are used to calculate the vertical spread of a point source for the first one or two km, the predictions turn out to be much smaller (by factors of 2 to 4) than the observed vertical spreads. This is logical, because a) the "initial" vertical spread

needs to be taken into account, and b) the initial spread is dominated by the plume turbulence rather than by environmental turbulence. The σ_{300} and K_z computations are not given here because it can be seen they are not really applicable. They would be expected to be applicable beyond several kilometers, but for the cases studied this is into the fumigation and the box model areas. When the base of the plume is at the ground and the top is limited by an inversion, the vertical diffusion process within the layer is of only secondary concern and is unobservable by the photographic method.

During the evaluation, we employed another way of deriving k_m for Hanna's K_z formula. This was to note the variations of the $\epsilon^{1/3}$ trace at one-second intervals and get a time (and hence space) scale from the autocorrelation curve. The results were comparable to (but slightly larger than) the k_m predictions by Hanna's method. Novikov and Stewart (1964) have investigated ϵ fluctuation spectra as indications of intermittency, and found they do not follow the same spectral relationships as do the normal turbulent motions. Thus, using this method to obtain k_m must be approached with caution. Hanna's method of K_z calculation, coupled to the estimation of k_m by the ϵ fluctuations does constitute an intriguing technique for deriving possibly meaningful data on the diffusing capability of the air from simple airborne measurements. This sort of method does seem to have worked quantitatively on another MRI study of shoreline diffusion, but, as noted earlier, the K_z method does not seem to be really useful in the present program.

The discussion so far has pertained to vertical plume rise and diffusion, since the available data are the photographic cross-sections. Turning briefly to the horizontal spread of the cloud, we must first note that photographic data are not available. Also, although observers' notes and particle deposits on the Moving Slide Impactor give some indication of plume width during crosswind traverses, such data are crude. Some such data are shown in the next section. The best data available are those few detailed cross-sections obtained with the lidar which are presented in the SRI report. As to theory, the airborne turbulence measurements are not able to give information on the directional shears which do the main broadening of the plume. Thus, we cannot say anything quantitative about the horizontal spread of the smoke. In a quantitative sense, for Photo Period 3, we find a rather strong directional shear at plume level and also find a wide plume, ten times as wide as it is deep. For Photo Period 7, there is less directional shear, and much less lateral spread.

VIII. PRELIMINARY COMPARISON OF MODEL PREDICTIONS AND OBSERVATIONS

The ultimate value of the plume rise and diffusion data is to provide a means for calculating downwind concentrations. Validation of the concentration model would permit simulation of a range of environment and stack conditions and, hopefully, frequency of occurrence of various concentration levels.

Most of the attempts to relate calculated and observed concentrations have made use, to some extent, of calculated values of various of the parameters required in the model calculations. Data obtained in the Keystone program permitted use of observed data on stack conditions, meteorological environment, and plume behavior in the model calculations. Stack data, plume size, and height as well as meteorological conditions were all measured and available for use.

Högström (1968) gives the downwind concentration as:

$$\chi = \frac{Q \exp(-y^2/2\sigma_y^2)}{2\pi\sigma_y\sigma_z\bar{u}} \left\{ \exp\left[-\frac{(z-h)^2}{2\sigma_z^2} \right] + \exp\left[-\frac{(z+h)^2}{2\sigma_z^2} \right] \right\} \qquad (23)$$

where χ = concentration (units/m^3)
Q = rate of emission (units/sec)
y = horizontal crosswind coordinate (m)
z = vertical coordinate (m)
h = height above ground of plume centerline (m)
$\bar{u}$ = wind speed (m/sec) at level h
σ_y = plume standard deviation (m) in horizontal crosswind direction
σ_z = plume standard deviation (m) in vertical direction

The Högström model has been programmed in its complete form for computational use. One day (17 October) was selected for comparison of observed and calculated SO_2 concentrations on the basis of data quality. Time did not permit additional comparisons.

Observational data for Photo Periods 3 and 4 have been used to calculate downwind concentrations from Eq. (23). Data used in the calculations are shown in Figs. 27 and 28. Plume altitudes were determined in two ways, from photographic-aircraft data and from extrapolation of ground photographic data. σ_z and σ_y data for stability condition B are shown in the figures for comparison. In the case of Photo Period 3, condition B approximates the σ_y observed data but the effect of the restricted mixing layer limits the value of σ_z beyond 1 km. For Photo Period 4 the growth of σ_y is larger than condition B but, again, the limited vertical extent of the mixing layer limits the growth of σ_z. It was observed, in several of the trials,

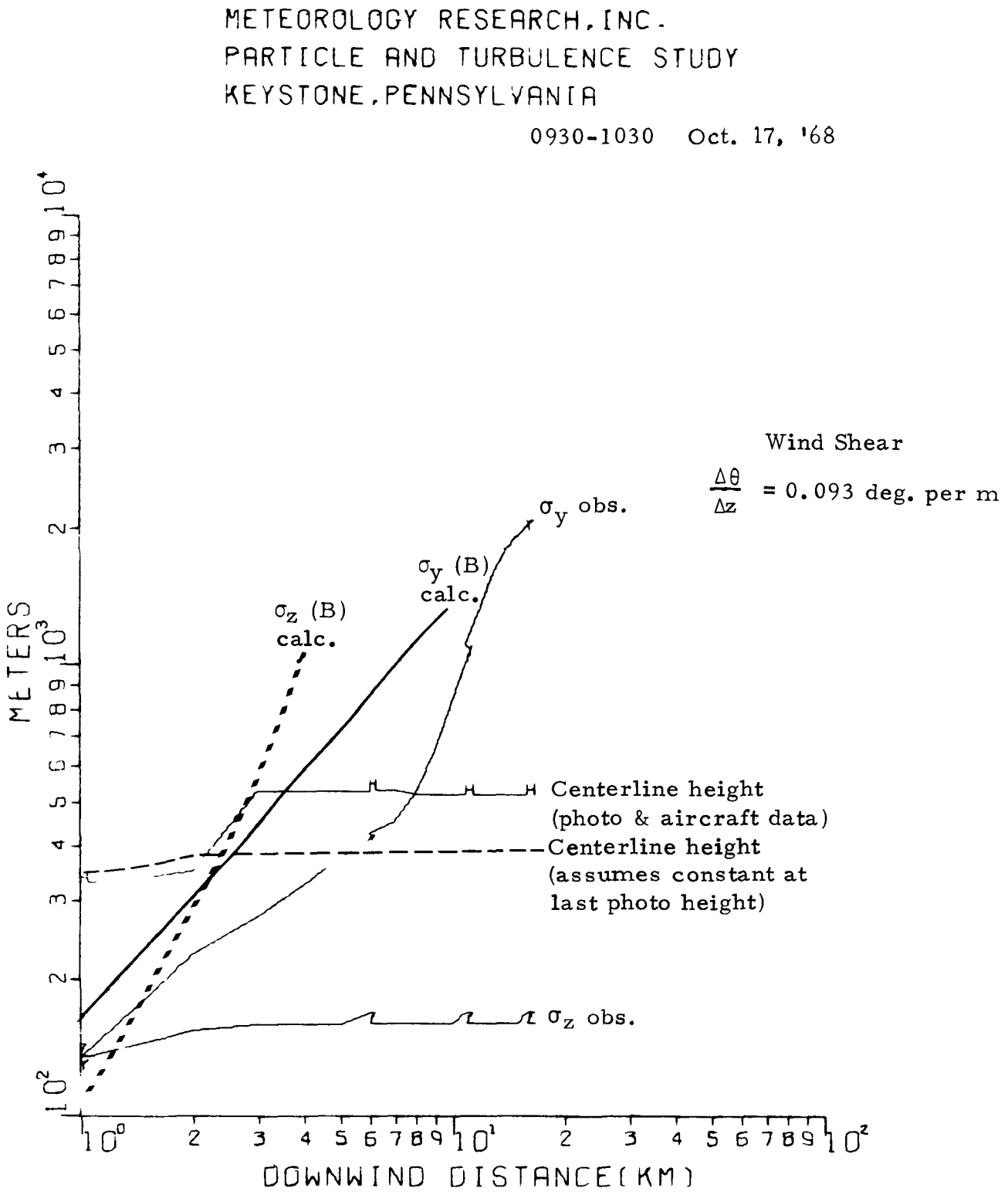

Fig. 27. CLOUD GROWTH CHARACTERISTICS, PHOTO PERIOD NO. 3

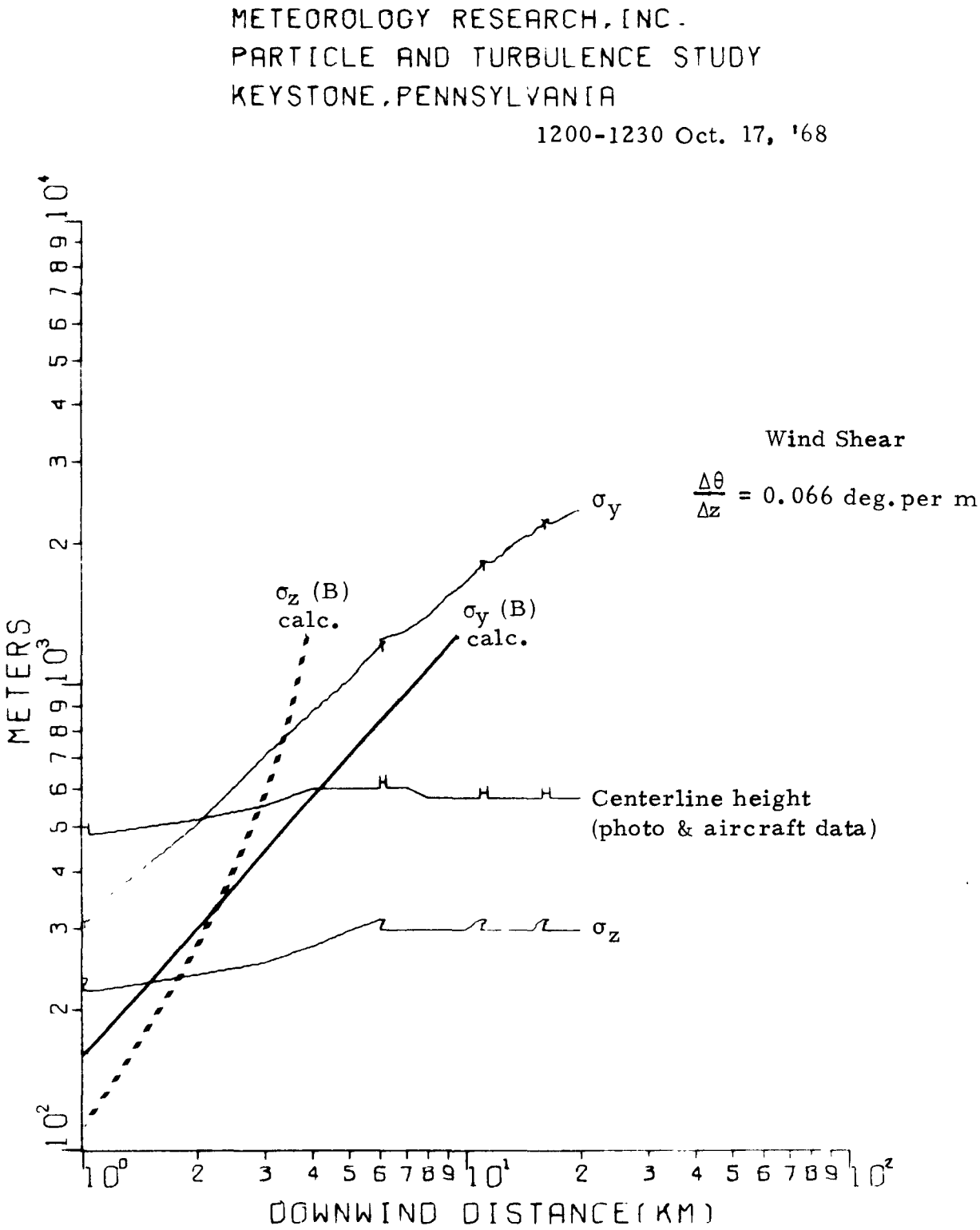

Fig. 28. CLOUD GROWTH CHARACTERISTICS, PHOTO PERIOD NO. 4

that σ_y was considerably increased by directional wind shear. This was particularly noticeable in aircraft traverses when one edge of the plume was quite sharp and distinct while the other was quite diffuse.

Predicted SO_2 concentration data are compared with helicopter observations in Figs. 29 and 30. Observed SO_2 concentration data peak in the neighborhood of 3-5 km downwind which falls in the fumigation zone. For this reason, observed peak concentrations are not modeled well by the calculations from Eq. (23). This is particularly true in the morning period (Fig. 29) where the normal diffusion equation substantially underpredicts concentrations at 3-5 km. Eq. (23) gives the right order of magnitude for the SO_2 concentration when the atmospheric mixing properties are relatively large (Fig. 30).

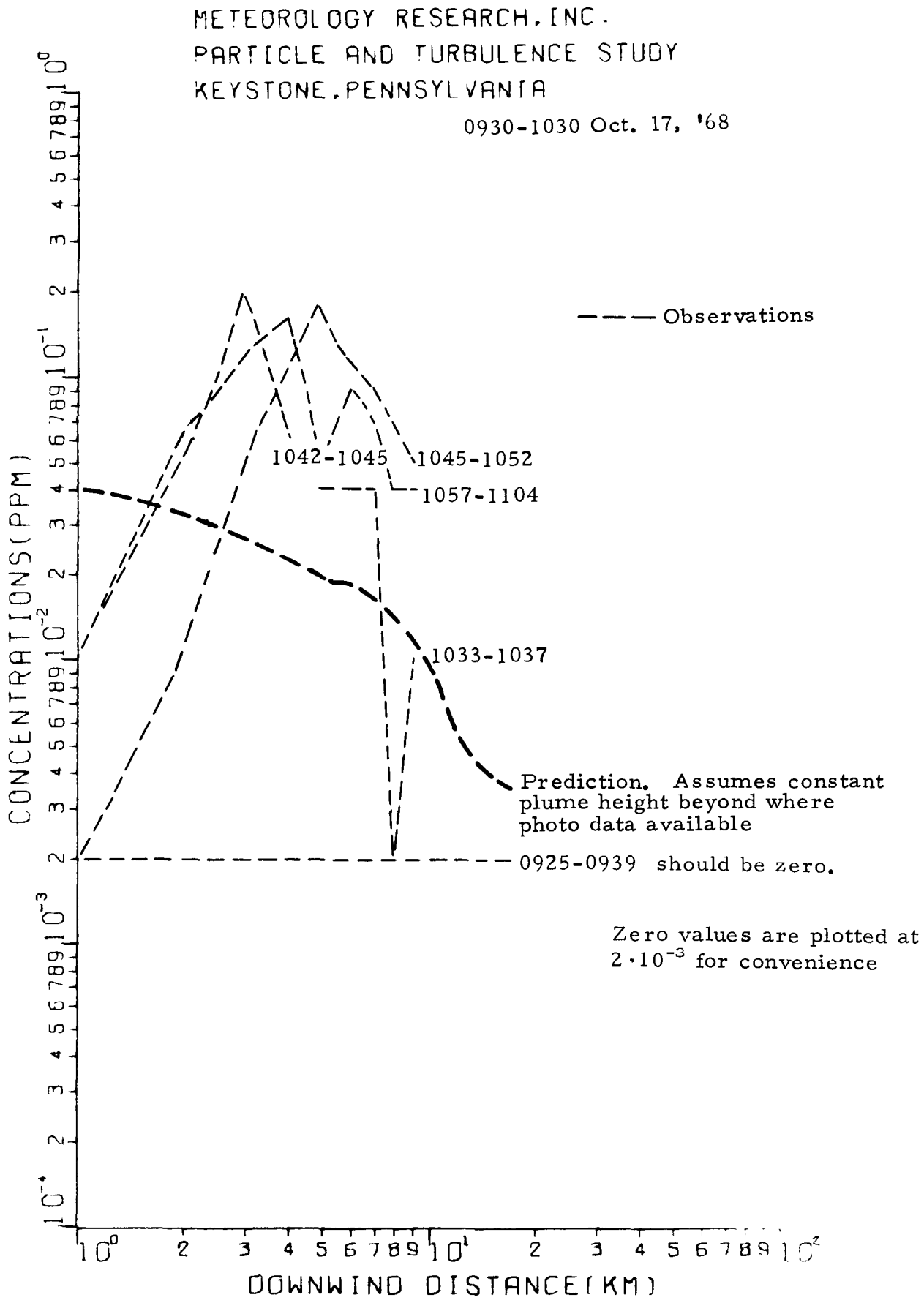

Fig. 29. SO_2 GROUND LEVEL CONCENTRATIONS, PHOTO PERIOD NO. 3

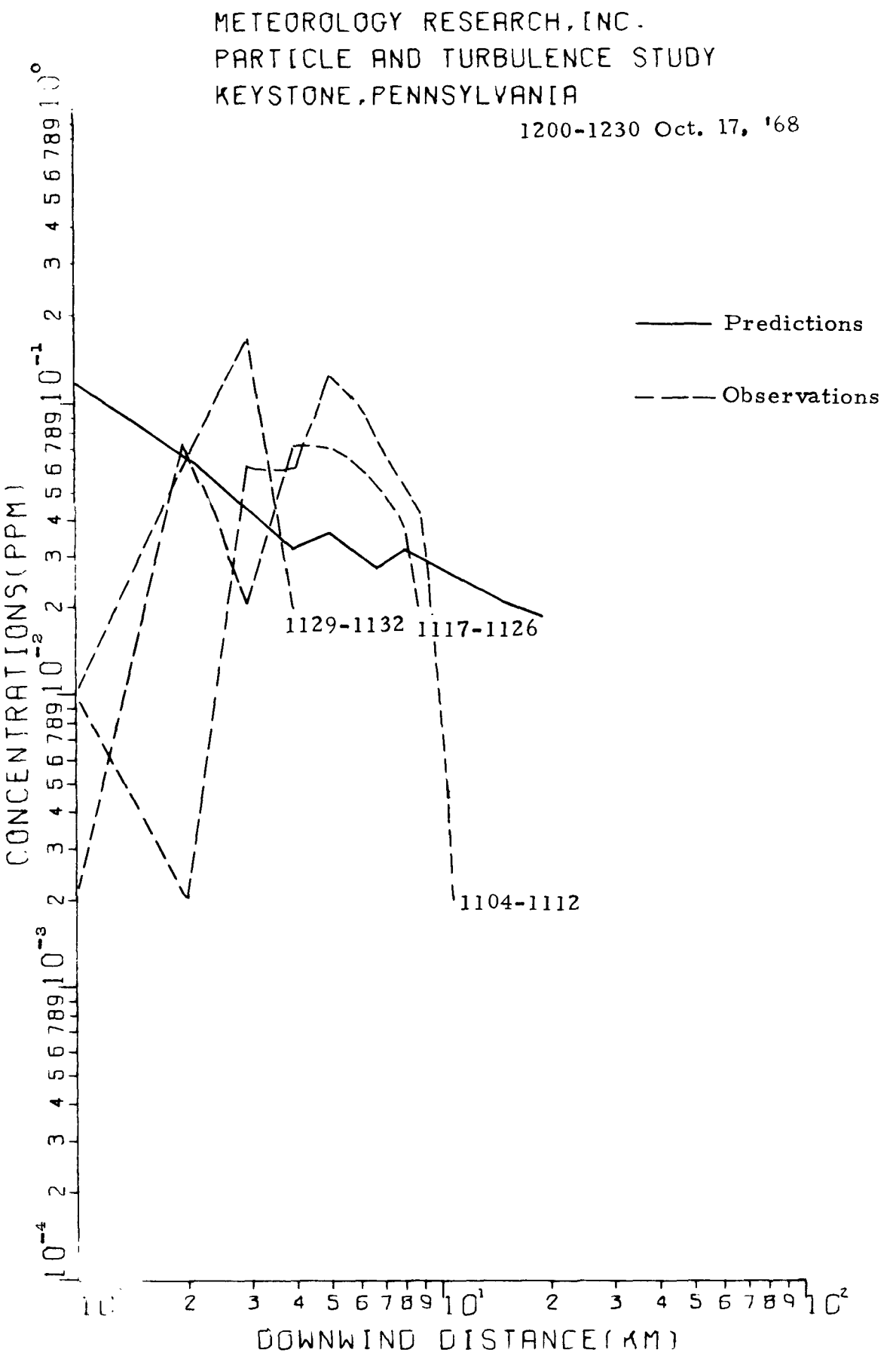

Fig. 30. SO_2 GROUND LEVEL CONCENTRATIONS, PHOTO PERIOD NO. 4

IX. CONCLUSIONS AND RECOMMENDATIONS

This program has demonstrated the use of the airborne UITS for handling various of field programs in diffusion. The instrument was used to map the environmental turbulence field, and in particular ascertain the top of the mixing layer. It was used also (1) to derive vertical exchange coefficients to explain the vertical transport of the plume in final stages of development, (2) to provide data for estimating τ_o and z_o, and (3) to help monitor and explain the decay of the turbulence in the initial plume. For all three of these items the use of the UITS seems valid but the experimental setup did not permit one to get a definitive test of the technique. For the first two items there were not adequate other data against which to make comparisons, and for both the second and third items the flight trajectories used with the UITS did not let one obtain turbulence information adequate for a resolution of the problem.

The technique of doing plume height and characteristics analyses from 35 mm slides from a single camera is demonstrated to be effective. Collecting particulates with the MSI to help delineate across-plume particulate characteristics also proved useful. Finally, the methods employed to handle all the data by digital computer techniques have been shown to be valuable. Hindsight clearly shows how the field experiment could have been improved. There were gaps in the data because of equipment malfunction; not having the Integrating Nephelometer was particularly troublesome. The evaluation techniques for the particulates could have been far more effective if the knowledge acquired by the end of the program had been available at the start -- but such is the case in almost all programs. Flight trajectories could have been designed to be more effective in answering particular questions, considering the constraints of flight coordination with other aircraft and balloons.

The main technical conclusions are given in the appropriate sections throughout the report. Certainly more can be done with the data than was possible within the limited scope of this program, but the total data from the aircraft and ground cameras probably do not warrant extensive further evaluation. A complete field program can be based on the long term compilation of gross data, or on a case study method whereby a few events are observed with such extensive instrumentation that all the dominant mechanisms are quantitatively delineated. This program involved the case study method but was too limited in time and scope to provide the complete data which would be necessary for getting definitive answers. The problem of lateral diffusion is especially interesting. The data available here on turbulence (from aircraft and sounding balloons), from the SRI lidars, and from aircraft traverses with the Moving Slide Impactor may be adequate to apply to a study of

this subject. The Nephelometer cross-section data, if available, would have been very helpful for this, as would $\epsilon^{1/3}$ readings in the early portion of the plume.

The LAPPES field program, with NAPCA, SRI, Sign-X, and MRI all cooperating, constitutes a good example of the benefits of cooperative work. The benefits far outweigh the difficulties involved in the coordination and the problems of conflicting responsibilities.

Various special recommendations are given in the appropriate chapters of this report. The overall recommendations are that:

(1) the present data not be evaluated more thoroughly by itself, although it constitutes an appropriate supplement for the other data on the program for general studies.

(2) an equivalent program be developed for plume studies in another region, presumably a coastal area. This program would draw on all the experience gained in the LAPPES program so far. It should be very carefully planned. It should strongly emphasize the case study approach, bringing together whatever techniques are required for adequately describing the time-varying environment and plume to considerable distances.

(3) The UITS applications which are introduced here deserve further evaluation on simple field experiments designed specifically for that purpose. All the applications described are deemed promising. Of special importance is the use of the UITS to obtain total vertical exchange coefficient data by combining direct $\epsilon^{1/3}$ measurements with a scale factor derived from $\epsilon^{1/3}$ variability. This study should take advantage of a thoroughly instrumented aircraft for complete turbulence measurements (several are available) for providing definitive comparison data. The program would work most effectively if dovetailed into an area-diffusion experiment.

REFERENCES

Briggs, G. A., 1969: Plume rise. Prepared for Nuclear Safety Information Center, Oak Ridge National Laboratory, by U. S. omic Energy Commission, Div. of Technical Information, 81 pp.

Charlson, R. J., N. C. Ahlquist, H. Selvidge, and P. B. MacCready, Jr., 1969: Monitoring of atmospheric aerosol parameters with the Integrating Nephelometer. J. Air Poll. Control Assoc., 19, 12, 937-942.

Cramer, H. E., G. M. DeSanto, K. R. Dumbauld, P. Morgenstern, and R. N. Swanson, 1964: Meteorological prediction techniques and data system. GCA Rept., Contr. No. DA-42-007-CML-552, 252 pp.

Goetz, A., 1969: A new instrument for the evaluation of environmental aerocolloids. Environ. Sci. and Tech., 3, 2, 154-160.

Halitsky, J., 1961: Single-camera measurements of smoke plumes. Intern. J. Air and Water Poll., 4, 314, 185-198.

Hanna, S., 1968: A method of estimating vertical eddy transport in the planetary boundary layer using characteristics of the vertical velocity spectrum. J. Atmos. Sci., 25, 1026-1033.

Hess, G. D., and H. A. Panofsky, 1966: The budget of turbulent energy near the ground. Quart. J. Roy. Meteor. Soc., 92, 277-280.

Högström, U., 1968: A statistical approach to the air pollution problem of chimney emission. Atmos. Environ., 2, 251-271.

Hoult, D. P., J. A. Fay, and L. J. Forney, 1968: A theory of plume rise compared with field observations. Publ. No. 68-2, Fluid Mechanics Lb., Dept. of Mechanical Engineering, Massachusetts Inst. of Technology

Johnson, W. B., Jr., and E. E. Uthe, 1969: Lidar study of stack plumes. Final Rept. for NAPCA, Stanford Research Inst., Menlo Park, Calif. Contr. No. PH 22-68-33, 116 pp.

MacCready, P. B., Jr., 1964a: Standardization of gustiness values from aircraft. J. Appl. Meteor., 3, 4, 439-449.

MacCready, P. B., Jr., 1964b: Comments on diffusion in the inertial subrange. Proc. Conf. on Diffusion of Toxic Materials into the Atmosphere and the Underlying Theory, 23-24 March, USAERDA, White Sands, New Mexico, pp. 79-88. Reprinted in Atmospheric diffusion in the inertial subrange, Phase I, by P. B. MacCready, Jr., B. L. Niemann, and L. O. Myrup, Interim Rept. to Public Health Service, Atmospheric Research Group Rept. 67 IR-478.

MacCready, P. B., Jr., and H. R. Jex, 1964: Turbulent energy measurements by vanes. Quart. J. Roy. Meteor. Soc., 90, 384, 198-203.

MacCready, P. B., Jr., and C. J. Todd, 1964: Continuous particle sampler. J. Appl. Meteor., 3, 4, 450-460.

MacCready, P. B., Jr., 1966: Operational application of a universal turbulence measuring system. Paper pres. AMS/AIAA Conf. on Aerospace Meteorology, Los Angeles, California, March 28-31, 13 pp.

Murthy, C. R., 1968: Wind tunnel modelling of chimney plumes. Rept. 68-78, Canada Centre for Inland Waters, Burlington, Ontario, 50pp.

Novikov, E. A., and R. W. Stewart, 1964: The intermittency of turbulence and the spectrum of energy dissipation fluctuations, Izv. Akad. Nauk SSSR, Ser. Geofis., 408-413.

Pasquill, F., 1962: Atmospheric Diffusion. D. VanNostrand Co., Lib. of Cong. Card No. 61-13476, 297 pp.

Proudfit, B. W., 1969: Plume rise from Keystone Plant. Final Rept. by Sign-X Laboratories, Inc., Essex, Connecticut, Contr. No. PH 86-68-94.

Scorer, R. S., 1968: The determination of stack height. Atmos. Environ., 2, 3, 225-226.

Slade, D. H., 1965: Dispersion estimates from pollutant releases of a few seconds to 8 hours in duration. Tech. Note 2-ARL-1, Air Resources Lab., ESSA, U. S. Dept. of Commerce, Washington, D.C., 23 pp.

Slade, D. H., 1969: Wind measurement on a tall tower in rough and inhomogeneous terrain. J. Appl. Meteor., 8, 293-297.

Slawson, P. R., and G. T. Csanady, 1967: On the mean path of buoyant, bent-over chimney plumes. J. Fluid Mech., 28, Part 2, 311-322.

Slawson, P. R., 1967: Observations of the mean path of buoyant bent-over plumes from large industrial stacks. Ph. D. thesis, University of Waterloo, Waterloo, Ontario, Canada. 117 pp.

Swinbank, W. C., 1964: The exponential wind profile. Quart. J. Roy. Meteor. Soc., 90, 119-135.

Tennessee Valley Authority, 1968: Full-scale study of plume rise at large electric generating stations.

Veress, S. A., 1969: Study of the three-dimensional extensionof polluted air. Final Tech. Rept., Univ. of Washington to Natl. Center for Air Pollution Control, Bureau of Disease Prevention & Environmental Control, PHS Cont. AP-00661-01.

Wasko, P. E., and H. Moses, 1961: Photogrammetric technique for studying atmospheric diffusion. Photogrammetric Eng., March, 92-98.

Appendix A

QUANTITATIVE PLUME DATA FROM GROUND PHOTOGRAPHS

by

Margaret C. Day

Introduction

During the October 1968 field program at the Keystone Power Plant, a large number of data-gathering activities were conducted simultaneously by several groups. One of the MRI activities was to make sequential photographs of the plumes from a camera set on the ground well off to the side. The main goal of the photographic work was to obtain data on the plume rise and plume characteristics, to serve as a framework for the interpretation of data from the aircraft, and to serve for the verification or upgrading of plume motion predictive equations.

Another aim of the photographic experiment was to gain experience with the usefulness of technique in the general area of plume studies, so that design of future experiments could be aided. As with any observational technique, there are both good and bad features of the photographic method. On the good side, observations are inexpensive and simple to make, and the series of photographs contain a tremendous amount of information on the spatial and time-varying properties of the plume. One limitation which is troublesome in many instances is that the plume being studied must contain enough particulates to make it visible, and the background conditions and lighting must also be such as to make the plume stand out. Another limitation is that each photograph gives only integrated two-dimensional information about the plume. Nevertheless, by carefully choosing the geometry of the setup, the derived data on plume dimensions and location can be very useful. The camera technique is basically good for delineating plume edges, not for directly indicating concentrations, but the edge statistics are often quite helpful in permitting the analyst to derive information on concentrations.

The main body of this report and this appendix demonstrate that very useful data can be derived from the photographic method, even with rather simple techniques. The value on other projects can be even greater if more refined techniques are employed -- the greater use of automation in data reduction, better optimizing of contrast factors, stereo photogrammetry, etc. The advanced techniques and equipment of photogrammetry, now extensively used in other fields, would make very significant contributions to air pollution research and control.

This appendix examines the methods used on this project to derive data, and gives illustrations of the resulting data. Figure 1 is a flow chart showing the steps involved. Subsequent sections of this appendix give explanations for each block on Fig. 1.

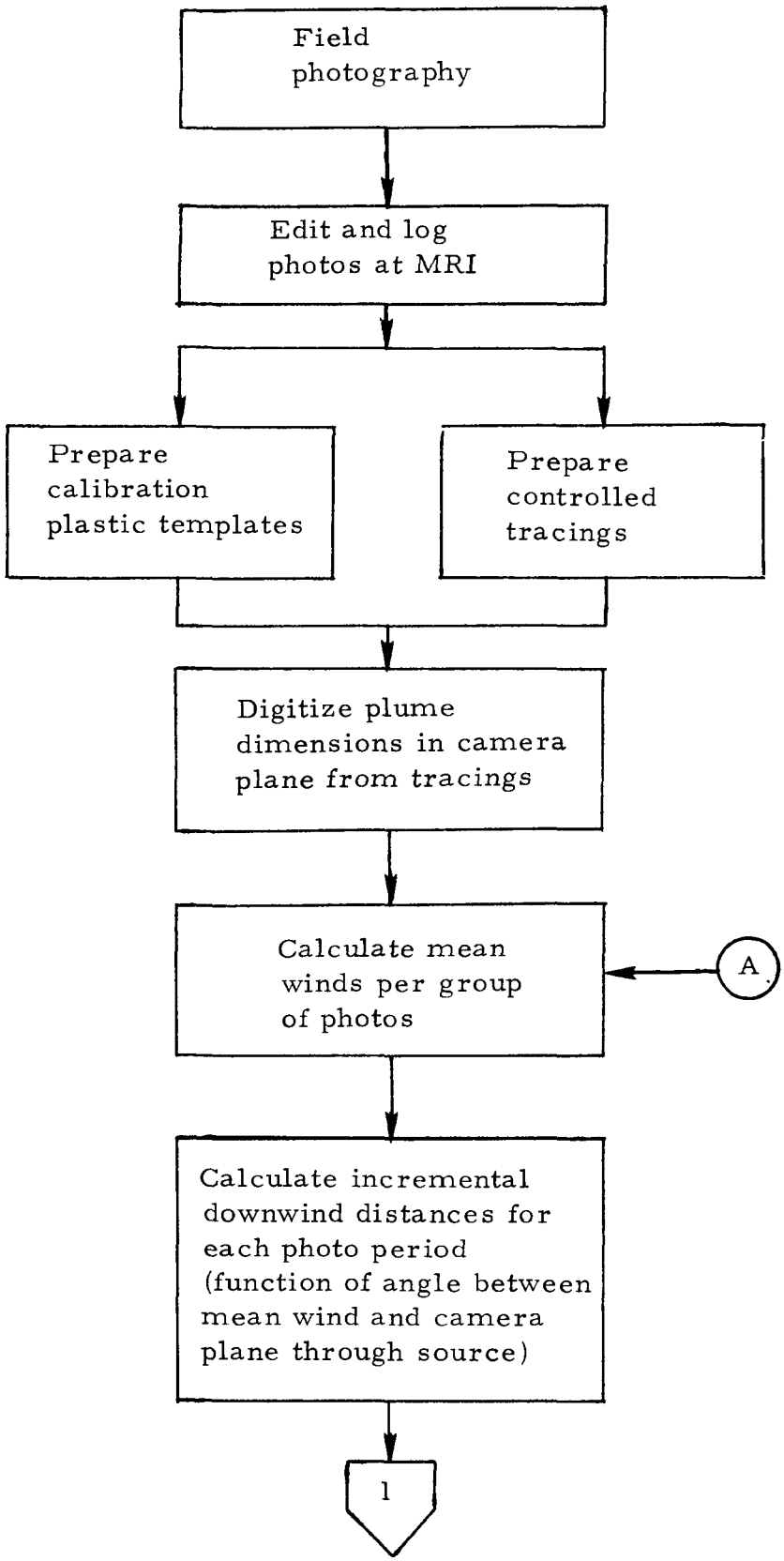

Fig. 1a. ANALYSIS OF GROUND PHOTOS. SYSTEM FLOW CHART

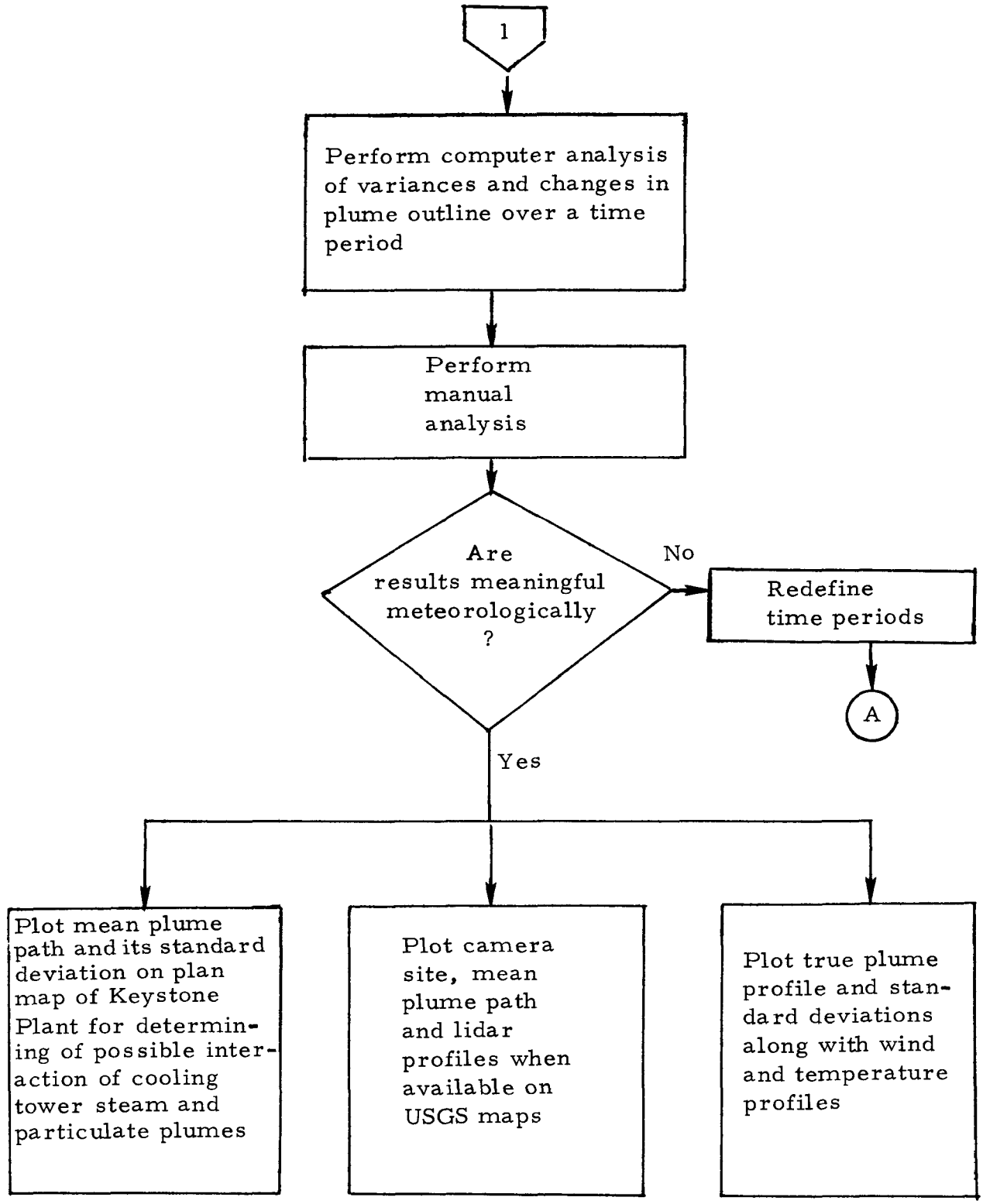

Fig. 1b. SYSTEM FLOW CHART (Continued)

Field Photography

The ground photography was done with an Argus C-4 35-mm camera, having a 50-mm lens. Kodachrome II film was used, with an ultraviolet filter. Picture series were made, with one frame every 2-3 minutes when the atmosphere was unstable and every 3-5 minutes under stable conditions.

It has been demonstrated by the Tennessee Valley Authority (1968)*, Scorer (1968), Halitsky (1961), Wasko and Moses (1961), Slawson (1967), and others that oblique ground photos can be used for retrieval of quantitative data when proper controls are applied. The following were considered in choice of camera setup for the ground photography:

(1) A camera site which would put the camera axis as nearly normal as feasible to the plume and far enough away to give a high probability that the true top of the plume is seen (note that aircraft observations were sometimes used to establish top conditions more accurately).

(2) The camera site, along with visible features seen in the camera's view, would be accurately identifiable on a large-scale U. S. G. S. map.

Figures 2 through 8 summarize the camera locations, winds, and other data for all the series.

Editing of Photos

Raw film was developed without cutting film strips to retain their sequence and preserve detail to the edge of every frame. These were edited and logged using a 35-mm projector modified by MRI to accept film strips.

All of the photographs were found to be of excellent quality. During two of the periods, there were high, thin altocumulus clouds behind the plume, but the plume dimensions were discernible due to its different nature. Higher resolution of the difference could be obtained in future work with the use of a double camera mount for stereo-measurement when background clutter becomes a problem. The success of this study demonstrates that consideration should be given to future photographic studies using engineered camera arrangements and automated stereo-reduction equipment. The desired transport and diffusion information could be obtained quickly and cheaply.

*References are collected at the end of the main body of the report.

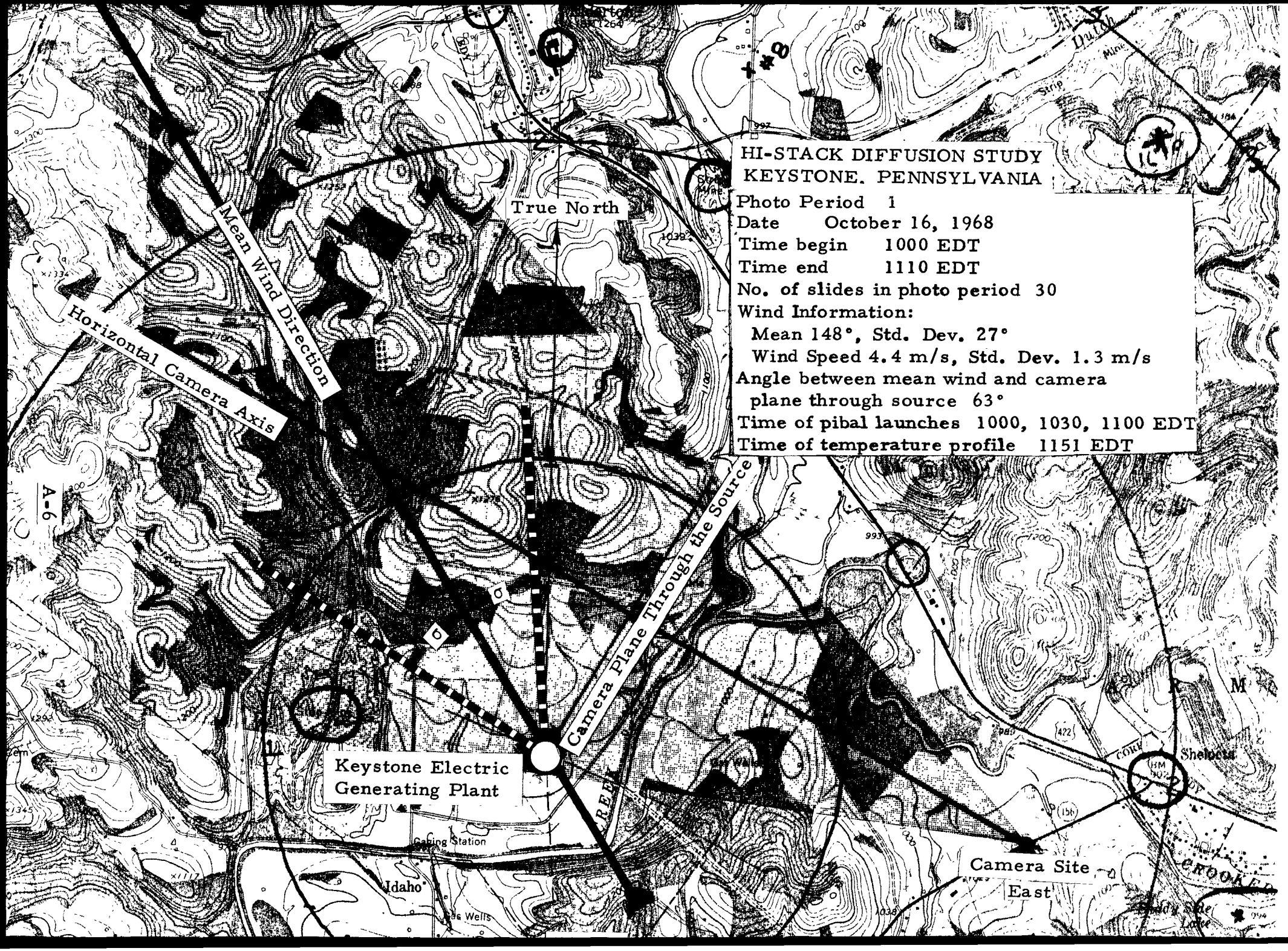
HI-STACK DIFFUSION STUDY
KEYSTONE. PENNSYLVANIA
Photo Period 1
Date October 16, 1968
Time begin 1000 EDT
Time end 1110 EDT
No. of slides in photo period 30
Wind Information:
Mean 148°, Std. Dev. 27°
Wind Speed 4.4 m/s, Std. Dev. 1.3 m/s
Angle between mean wind and camera plane through source 63°
Time of pibal launches 1000, 1030, 1100 EDT
Time of temperature profile 1151 EDT
True North
Mean Wind Direction
Horizontal Camera Axis
Camera Plane Through the Source
Keystone Electric Generating Plant
Camera Site
East
A-6

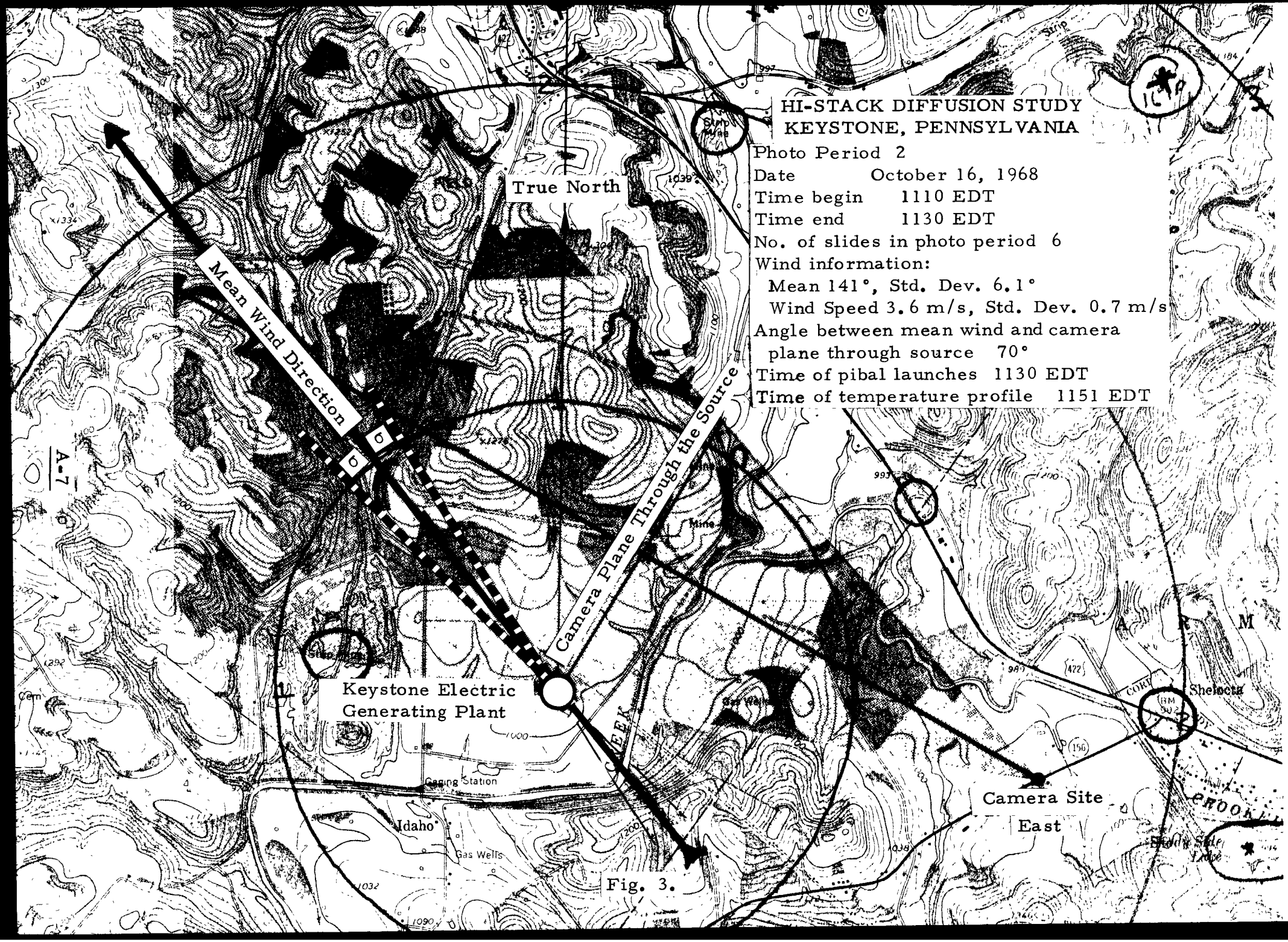
HI-STACK DIFFUSION STUDY
KEYSTONE, PENNSYLVANIA
Photo Period 2
Date October 16, 1968
Time begin 1110 EDT
Time end 1130 EDT
No. of slides in photo period 6
Wind information:
Mean 141°, Std. Dev. 6.1°
Wind Speed 3.6 m/s, Std. Dev. 0.7 m/s
Angle between mean wind and camera plane through source 70°
Time of pibal launches 1130 EDT
Time of temperature profile 1151 EDT
True North
Mean Wind Direction
Camera Plane Through the Source
Keystone Electric Generating Plant
Camera Site East
A-7

Fig. 3.

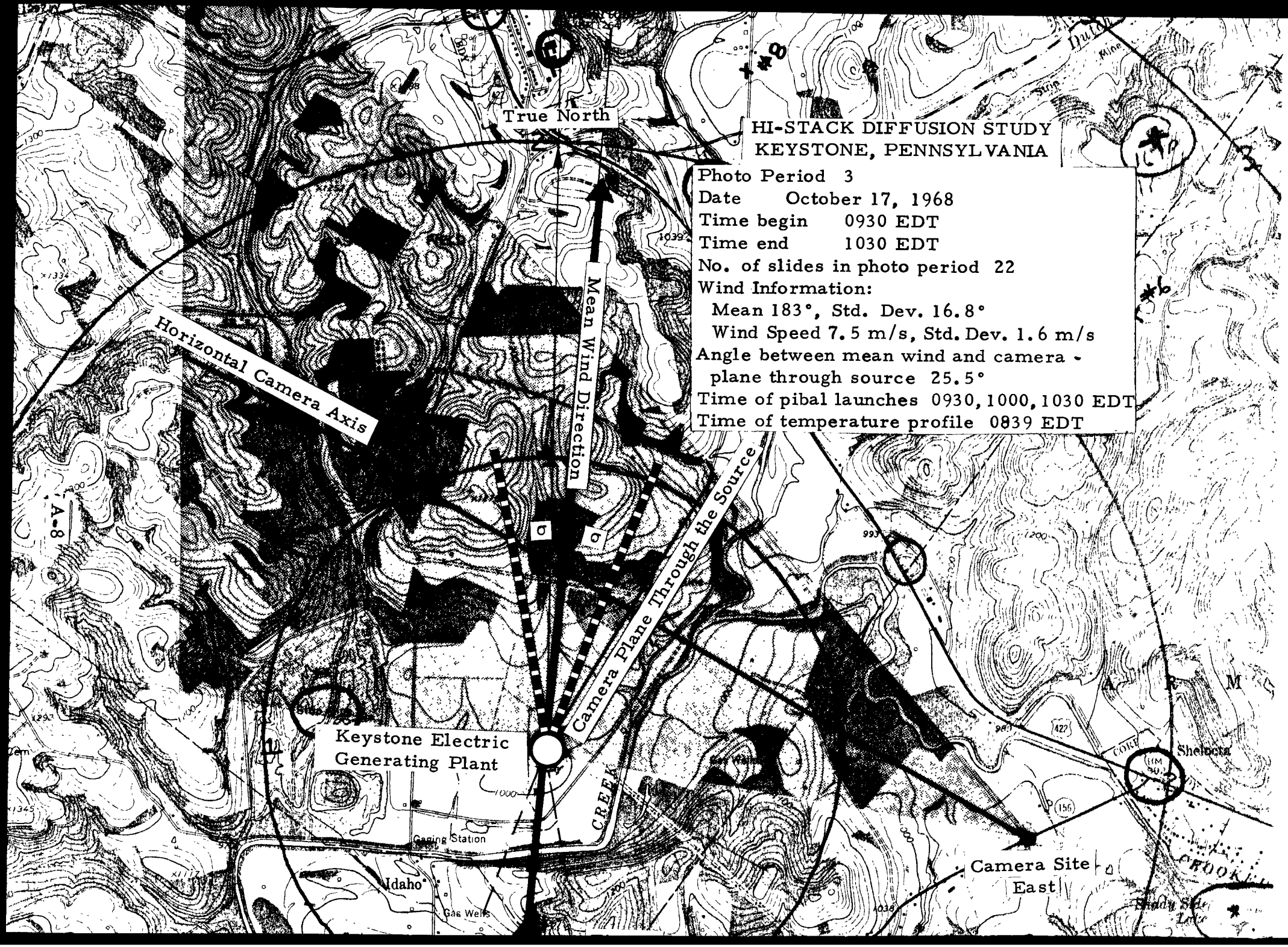
True North
Mean Wind Direction
Horizontal Camera Axis
Camera Plane Through the Source
σ
σ
Keystone Electric
Generating Plant
Camera Site
East
Idaho
Gas Wells
Gasing Station
Sheloeta
CREEK
CROOK
A-8
HI-STACK DIFFUSION STUDY
KEYSTONE, PENNSYLVANIA
Photo Period 3
Date October 17, 1968
Time begin 0930 EDT
Time end 1030 EDT
No. of slides in photo period 22
Wind Information:
Mean 183°, Std. Dev. 16.8°
Wind Speed 7.5 m/s, Std. Dev. 1.6 m/s
Angle between mean wind and camera - plane through source 25.5°
Time of pibal launches 0930, 1000, 1030 EDT
Time of temperature profile 0839 EDT

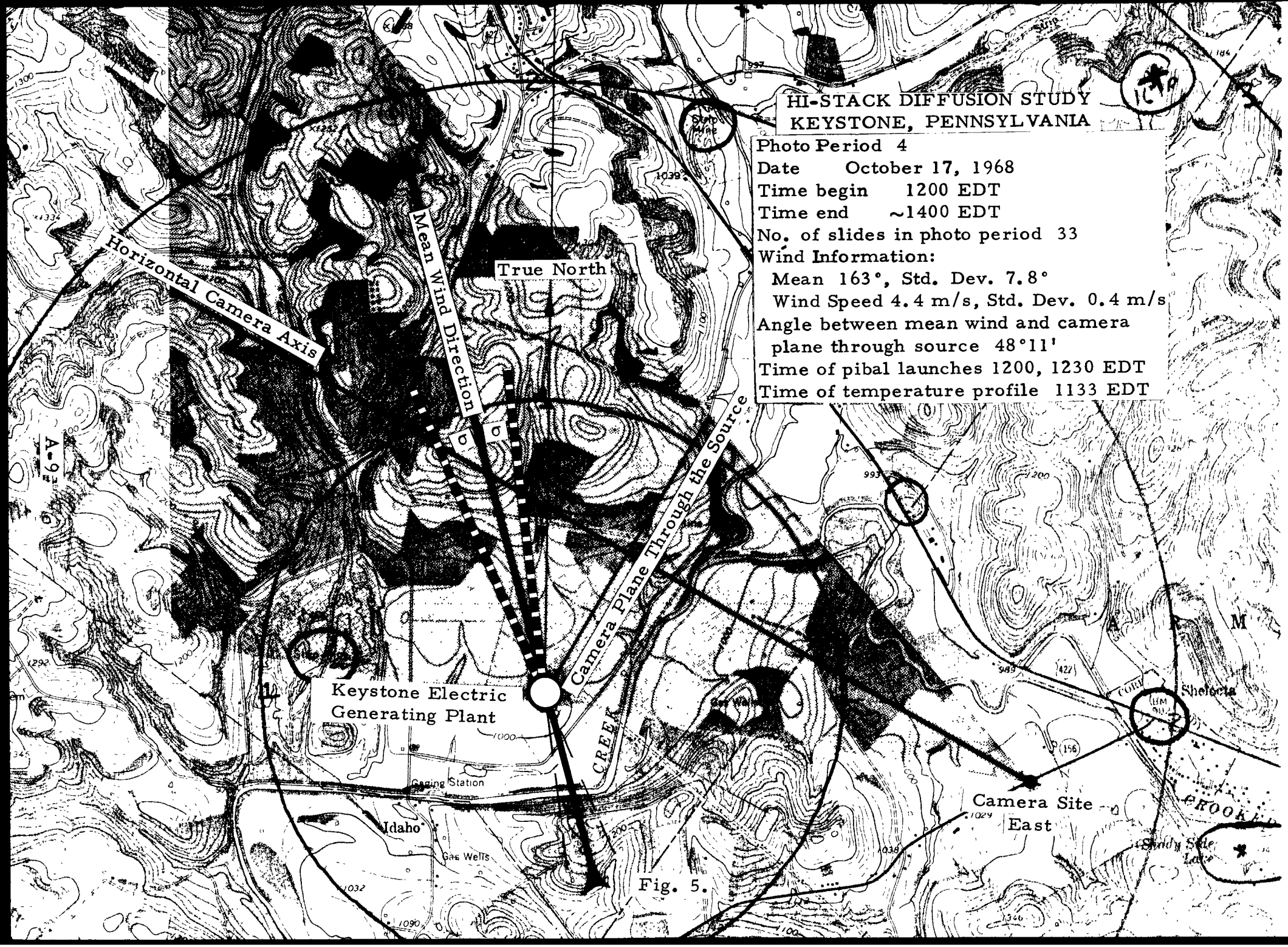
HI-STACK DIFFUSION STUDY
KEYSTONE, PENNSYLVANIA
Photo Period 4
Date October 17, 1968
Time begin 1200 EDT
Time end ~1400 EDT
No. of slides in photo period 33
Wind Information:
Mean 163°, Std. Dev. 7.8°
Wind Speed 4.4 m/s, Std. Dev. 0.4 m/s
Angle between mean wind and camera plane through source 48°11'
Time of pibal launches 1200, 1230 EDT
Time of temperature profile 1133 EDT
Horizontal Camera Axis
Mean Wind Direction
True North
Camera Plane Through the Source
Keystone Electric Generating Plant
Camera Site East
Idaho
Gas Wells
Gaging Station
Shelocta
CREEK
BROOK
A-9
6

Fig. 5.

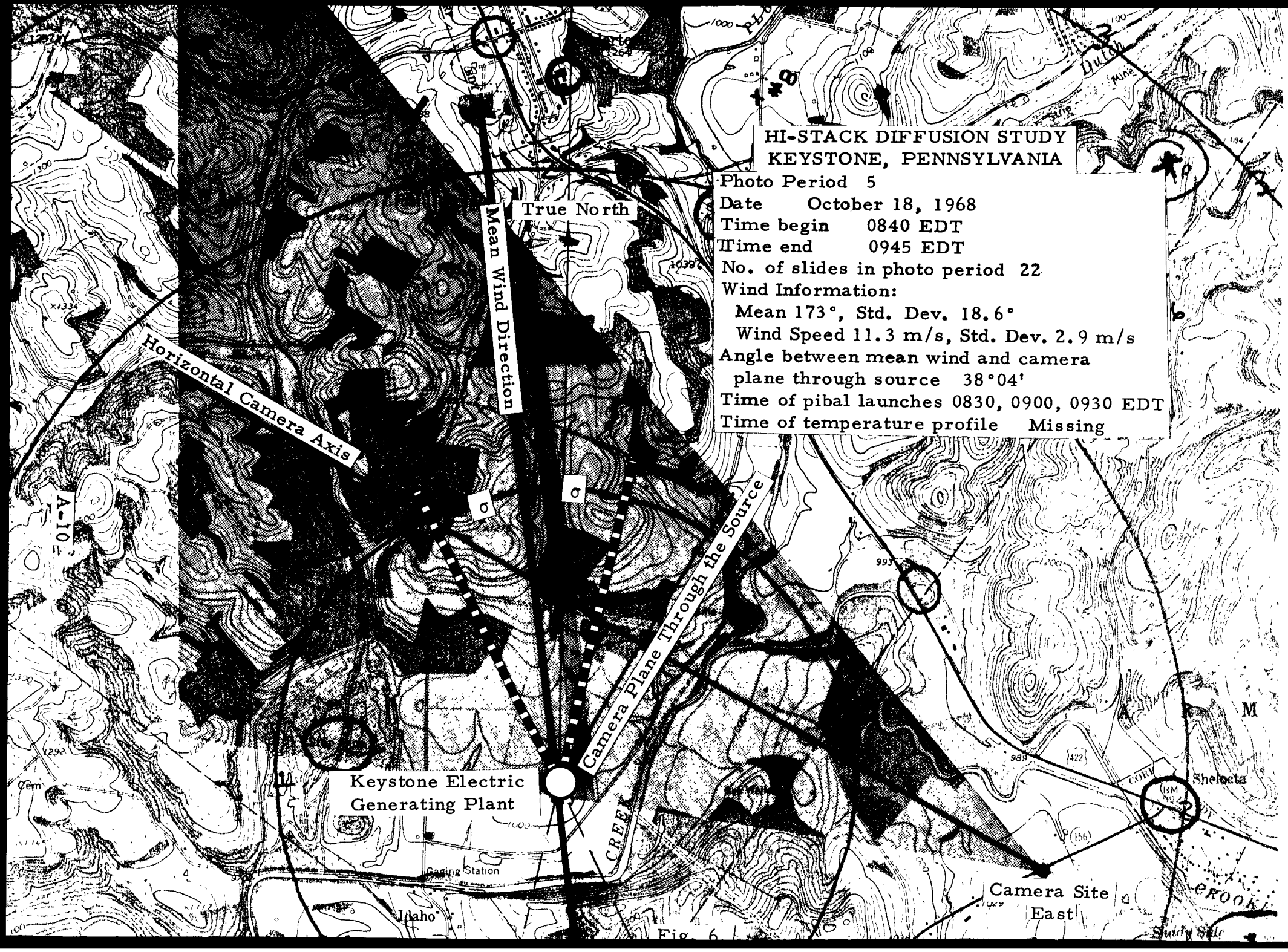
HI-STACK DIFFUSION STUDY
KEYSTONE, PENNSYLVANIA
Photo Period 5
Date October 18, 1968
Time begin 0840 EDT
Time end 0945 EDT
No. of slides in photo period 22
Wind Information:
Mean 173°, Std. Dev. 18.6°
Wind Speed 11.3 m/s, Std. Dev. 2.9 m/s
Angle between mean wind and camera plane through source 38°04'
Time of pibal launches 0830, 0900, 0930 EDT
Time of temperature profile Missing
True North
Mean Wind Direction
Horizontal Camera Axis
Camera Plane Through the Source
σ
σ
Keystone Electric Generating Plant
Camera Site East
Gaging Station
Idaho
Sheloeta
A-10

Fig. 6

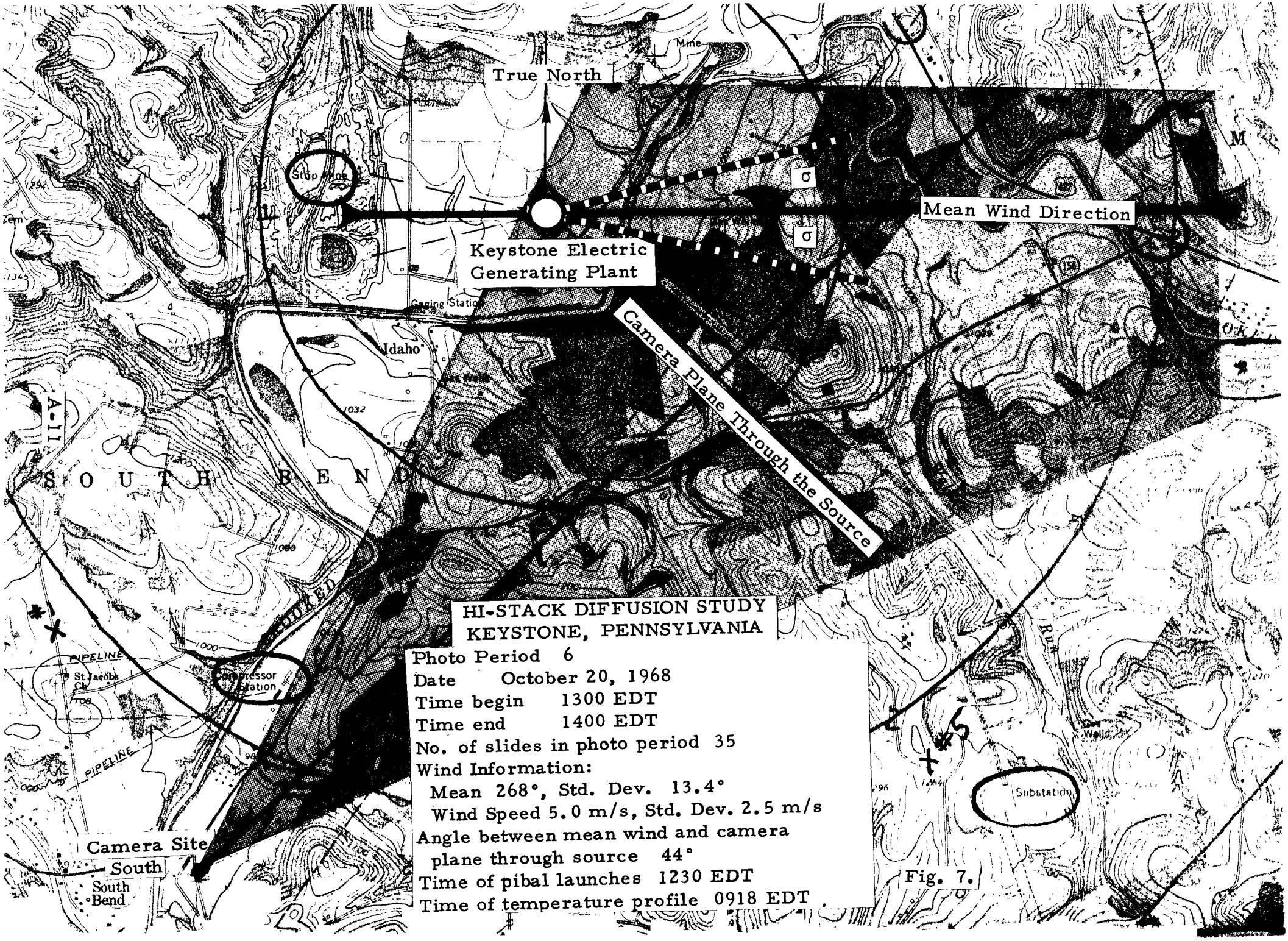
True North
Mean Wind Direction
σ
σ
Keystone Electric
Generating Plant
Camera Plane Through the Source
Camera Site
South
South
Bend
HI-STACK DIFFUSION STUDY
KEYSTONE, PENNSYLVANIA
Photo Period 6
Date October 20, 1968
Time begin 1300 EDT
Time end 1400 EDT
No. of slides in photo period 35
Wind Information:
Mean 268°, Std. Dev. 13.4°
Wind Speed 5.0 m/s, Std. Dev. 2.5 m/s
Angle between mean wind and camera
plane through source 44°
Time of pibal launches 1230 EDT
Time of temperature profile 0918 EDT

Fig. 7.

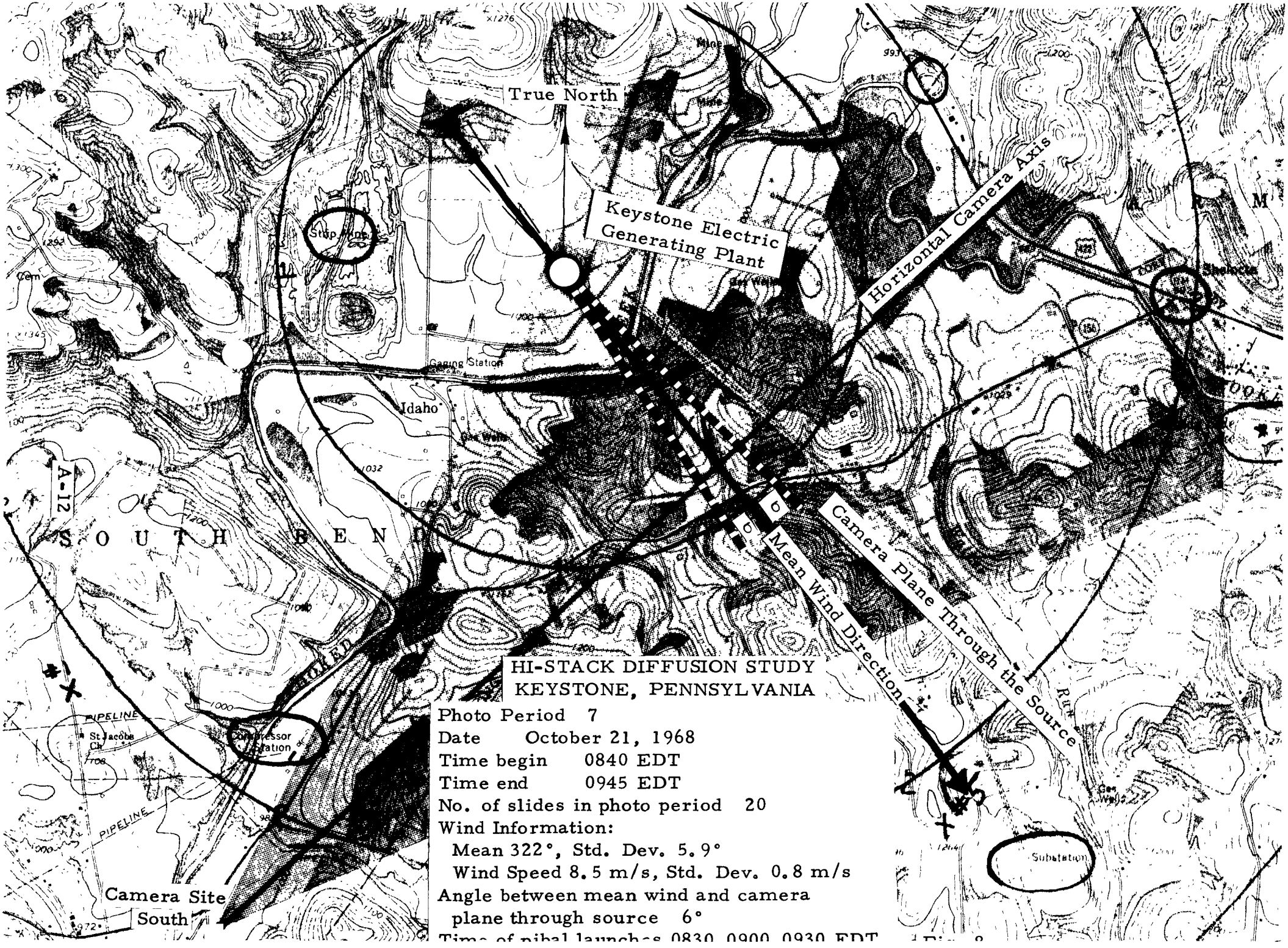
True North
Keystone Electric Generating Plant
Horizontal Camera Axis
Camera Plane Through the Source
Mean Wind Direction
Camera Site
South
SOUTH BEND
Idaho
Gaging Station
Compressor Station
PIPELINE
St Jacobs Ch
Substation
A-12
HI-STACK DIFFUSION STUDY
KEYSTONE, PENNSYLVANIA
Photo Period 7
Date October 21, 1968
Time begin 0840 EDT
Time end 0945 EDT
No. of slides in photo period 20
Wind Information:
Mean 322°, Std. Dev. 5.9°
Wind Speed 8.5 m/s, Std. Dev. 0.8 m/s
Angle between mean wind and camera plane through source 6°
Time of pibal launches 0830, 0900, 0930 EDT

During this initial qualitative editing, the effects of the steam from the cooling towers became apparent. At times, it was noted that the steam seemed to be rising through the plume, causing creation of small cumulus clouds which separated themselves from the plume and continued to rise because of their own buoyancy. It was decided to include analysis of the relative paths of the two plumes as one goal of quantitative reduction procedures. The study of the merging of the plumes is especially important with respect to evaluating particle data relative to direct collection and to the lidar. The high humidities should affect hygroscopic particles. Since the operative coolers and the stack are roughly in an E-W line, from Figs. 2 to 8 it can be seen that October 20 should represent such a day. Data on this subject are examined more completely in the main report.

Preparation of Calibration Templates

A goal of ±10 meters of accuracy for top and bottom plume boundaries was set as needed for valid delineation of plume behavior over distance.

A 5 x 7 black and white print was made of selected typical examples of the photos. These were used for photo interpretation and accurate identification of known features: roads, railroads, terrain details. A power line became identifiable on the 1:24,000 U.S.G.S. map. Relative position, height, and dimensions of the Keystone stacks and cooling towers were used to confirm calculated distances on the camera plane through the source.

Exploratory work on these photos was feasible because only two camera sites were used over the seven photographing periods. Each additional camera site compounds the calculations formidably when calibrations are calculated by hand, as they were in this case, with an Olivetti-Programa 101 Desk Computer as the only aid. The method is now straightforward and clearly defined; therefore, it could easily be computerized to allow a freer choice of camera sites for future work.

Vertical calibration:

See Fig. 9.
Parameter accuracy:

- Stack dimensions are published and surveyor accurate.
- Measurements from 1:24,000 U.S.G.S map:
    1. Horizontal - measured in kilometers from map scale. 100 percent confidence at ±50 meters.
    2. Vertical - (20-foot contour intervals) 100 percent confidence at ±3 meters.

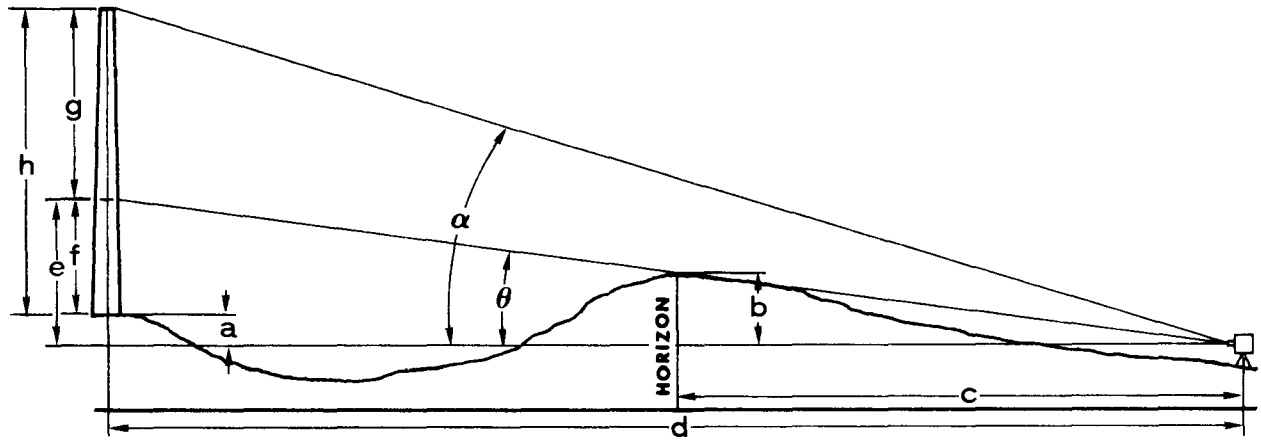

Keystone Calculations	Camera Site East	Camera Site South
Stack height (h)	244 m	244 m
Camera elevation	320 m MSL	297 m MSL
Horizon elevation	335 m MSL	335 m MSL
Stack base	308 m MSL	308 m MSL
b	15 m MSL	38 m
c	1360 m MSL	2370 m
tan θ (b/c)	0.011029	0.016033
Distance from camera to stacks (d)	2540 m	3870 m
e (d tan θ)	28 m	62 m
a	-12 m camera above stack base	+11 m camera below stack base
f (e - a)	40 m	51 m
Visible stack height (g)	204 m	193 m
tan $\alpha \left(\frac{g+e}{d}\right)$	0.09133	0.06589
α	5°13'	3°46'

Fig. 9. VERTICAL CALIBRATION FACTORS AND GEOMETRY

- Elevation of stack base MSL known exactly.
- Elevation of camera site interpolated from map contours.
- Elevation and relative distance of horizon between camera and stacks established after drawing an engineer's terrain profile along the line of sight from camera to stacks.

The angle, α, to the top of the stack could be calculated from known parameters. Using this as an anchor point, the template-inches/vertical degree were assumed to be related linearly to the tangent of each even vertical angle. Parallax at the edge of the photo was not considered because the plume was near stack top at the source edge and plume boundaries were seldom measured to the downwind side of the photo. The camera was set up to place the stack top almost at the vertical center of the photo where vertical parallax is absent or negligible. Until parallax is considered, there will be a small but increasing error in measurements on the downwind half of the photo.

Horizontal calibration:

See Fig. 10.

The camera has a known horizontal angle of ~40°, accuracy of which never had to be determined because horizontal distances were never measured to either the right or left edge of the photo. Known features such as the stacks, a horizon power pole, terrain features, and landmarks were used to determine the location of the vertical center line of the field of view. All horizontal measurements were made either to the right or left of this line. The known distance from the stacks to this vertical plane was then divided into convenient increments (Camera site East: Δ_o = 50 meters, Camera site South: Δ_o = 100 meters) with Δ_o remaining constant downwind from the vertical center line. The horizontal distances were calibrated in absolute distances because only two camera sites were used and only two plastic templates were required and a further mathematical conversion could be avoided. For the case where many camera sites are used, the calibration would be done in degrees right and left of center to create a universal template and conversion to absolute distances would be part of the computer program. These would be, of course, a function of distance of the camera from the source and would require that more be known about the camera angle and lens parallax.

A grid was photographed with the camera used in this study. It was found that lens distortion was minimal, well within the accuracy of the other parameters. The apparent tilt of the stacks near the edge of the photo was confirmed as giving an accurate measure of this. The vertical lines were allowed to converge by this small amount and otherwise; for expediency,

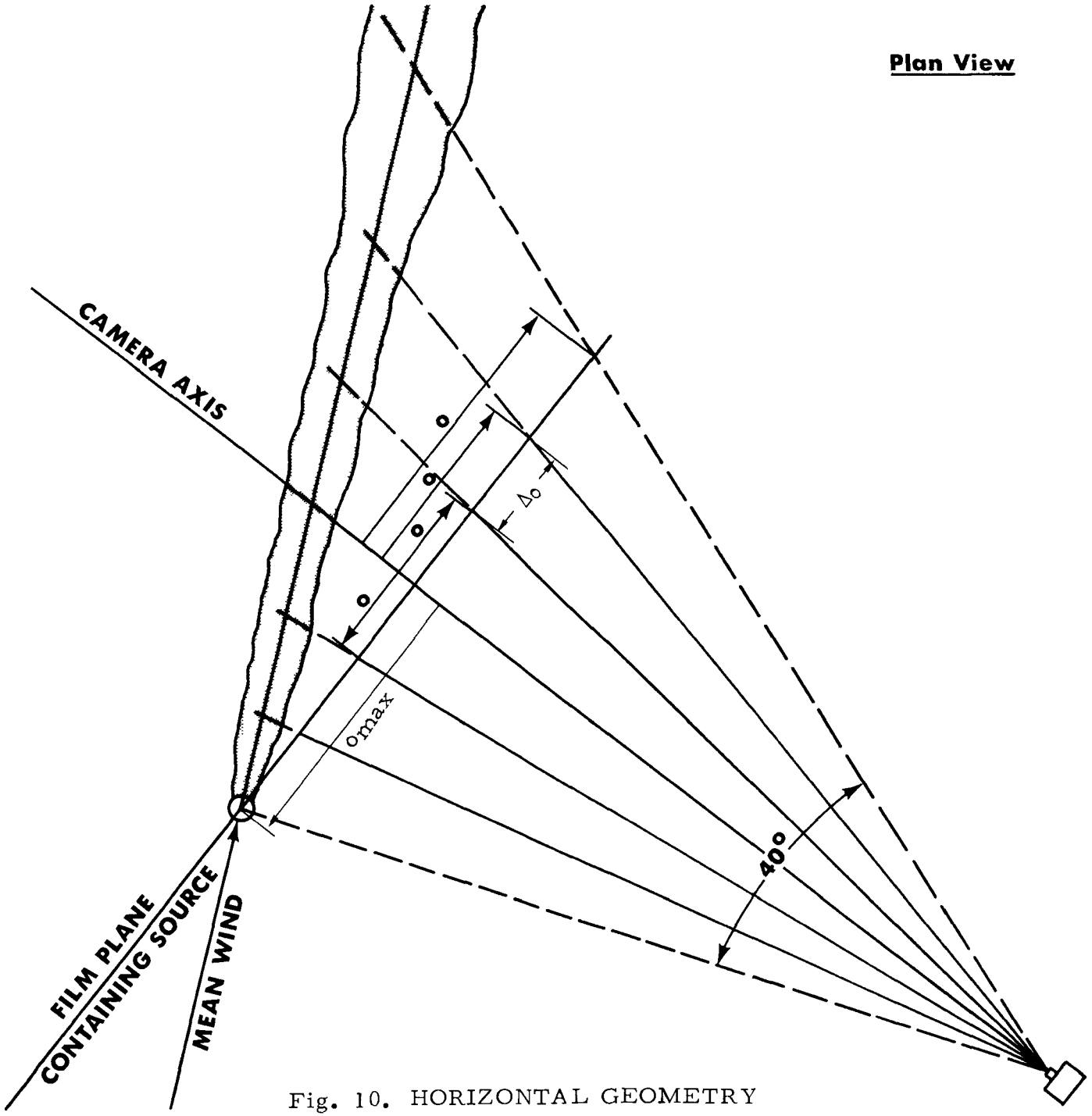

Fig. 10. HORIZONTAL GEOMETRY

no other correction was applied for lens distortion. A careful quality control was applied to the templates. It was found that they would give an accuracy of ±3 meters at the mean distances to be considered. Encouraged by this success, the work was continued. Preparation of final templates was delayed until the projector setup was known and its geometry established. Scales were chosen which would allow the easiest reading of incremental plume dimensions. It was found that preparation of final templates using the constant projector-screen relationship eliminated the need for a complex examination of real-life-to-camera plane-to-film-to-projector-to-screen relationships (Halitsky, 1961).

Controlled Tracings

See Figs. 11 through 15. These are examples of the cases for a variety of circumstances. More complete presentations are in the data volumes and main body of this report.

The photo package contains 170 35-mm color slides divided into seven photographing periods. Each slide was projected onto a screen from a constant projector setup. For this study, an individual tracing was made of the visible plume top and bottom for each slide. The behavior of the winds had not yet been analyzed; therefore, it was not known what the final time-grouping would be. Note was taken of

(1) High-confidence sharp plume dimensions (no guesses were attempted when the outline could not be seen clearly).

(2) Conditions of fumigation when smoke was clearly being transported to the ground; therefore, no bottom outline was visible except its path from the stack to the ground.

(3) Trajectory of the steam plume from the cooling towers and the outline of its apparent mingling with the plume.

(4) Any abrupt change of plume behavior during each series.

(5) Location of known features (stack, roads, power poles, even clumps of trees or buildings), to allow proper registration of the plastic template on each tracing.

A possible great saving of time should be considered for a new study of this kind. The work of preparing these tracings could be eliminated if a universal template were used on the projection screen whereby the dimensions of the plume could be digitized directly from the projected slide. The more laborious method of the tracings was used for this study to obtain a hard copy of the data for analysis.

The case when vertical plume profile well defined for entire width of photo.

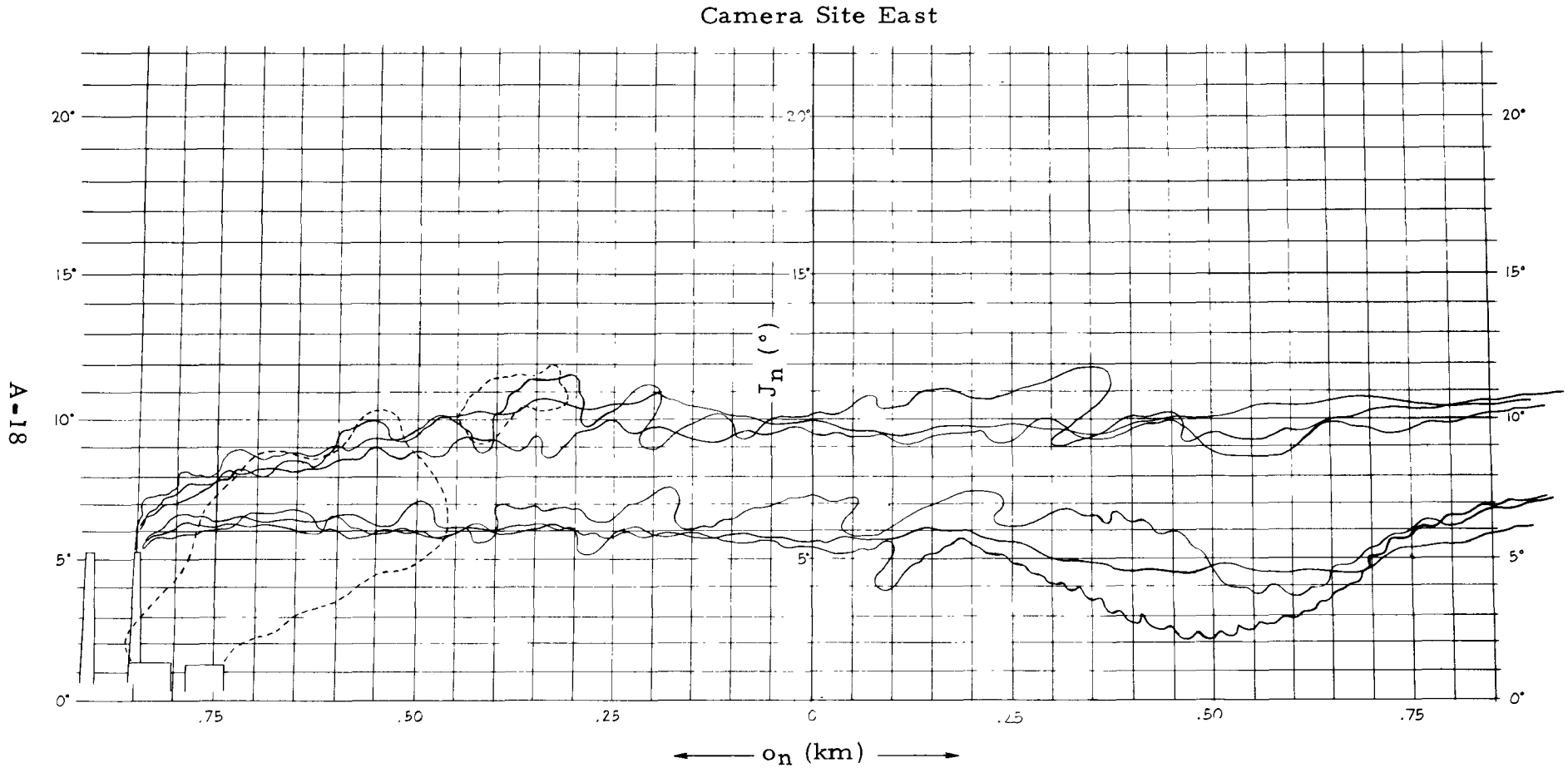

Fig. 11. PLUME PROFILE AS SEEN IN THE CAMERA PLANE THROUGH THE SOURCE

The case when the path of the effluent to the ground is well defined.

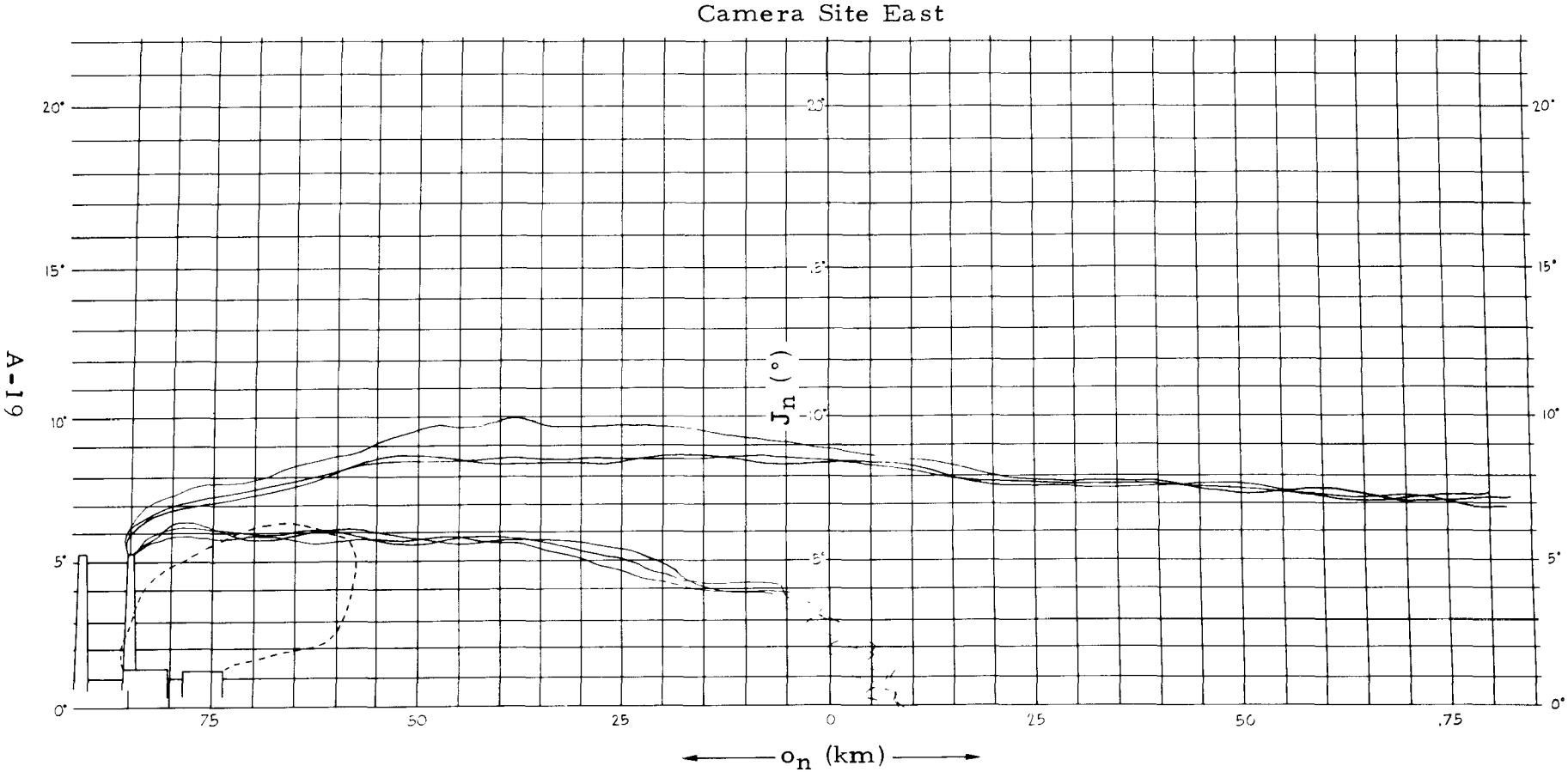

Fig. 12. PLUME PROFILE AS SEEN IN THE CAMERA PLANE THROUGH THE SOURCE

The case when plume boundaries become too indistinct for visual measurement.

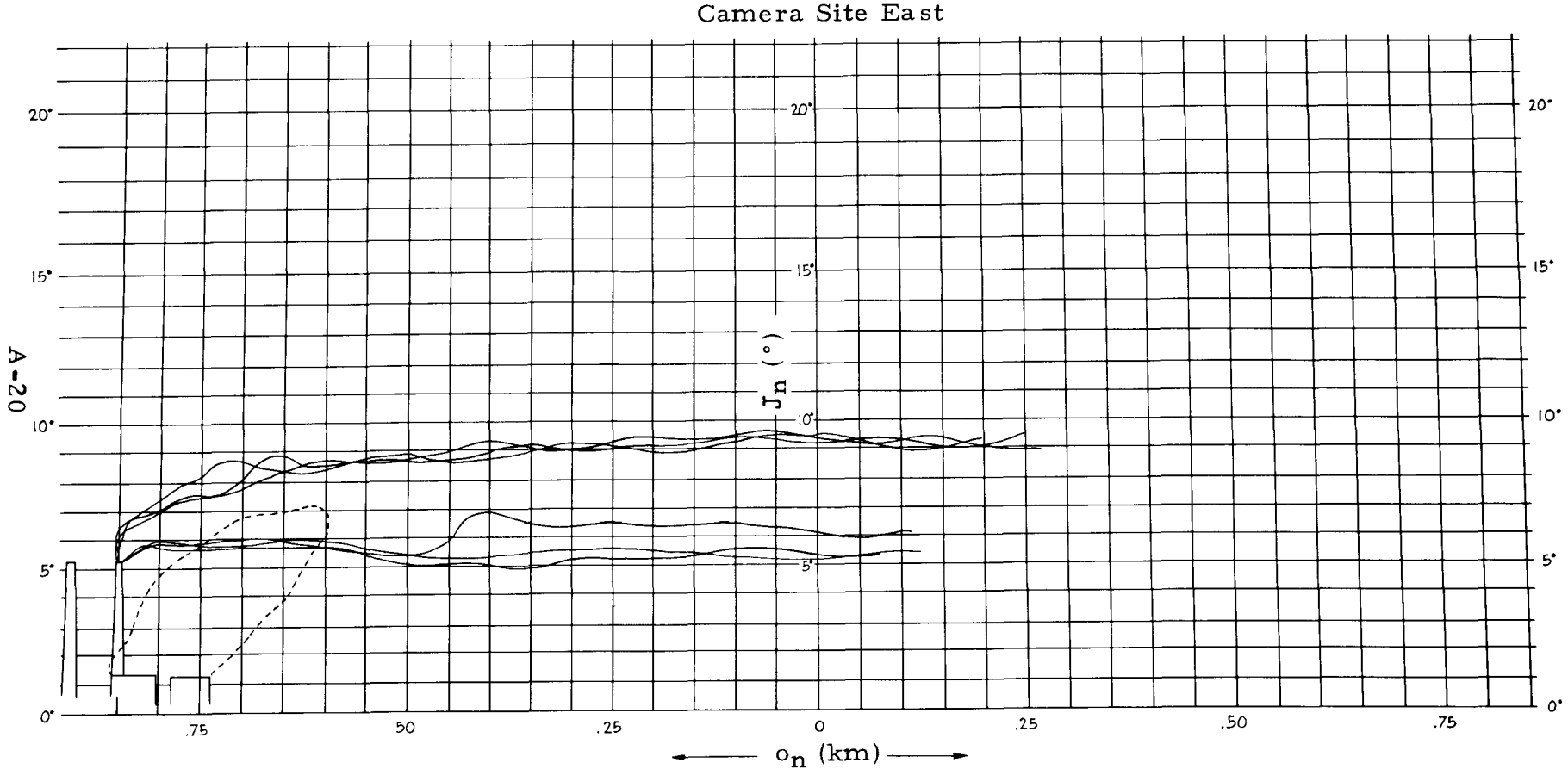

Fig. 13. PLUME PROFILE AS SEEN IN THE CAMERA PLANE THROUGH THE SOURCE

The case when extreme looping at top is clearly visible and the lower part of plume is impossible to define due to dilution.

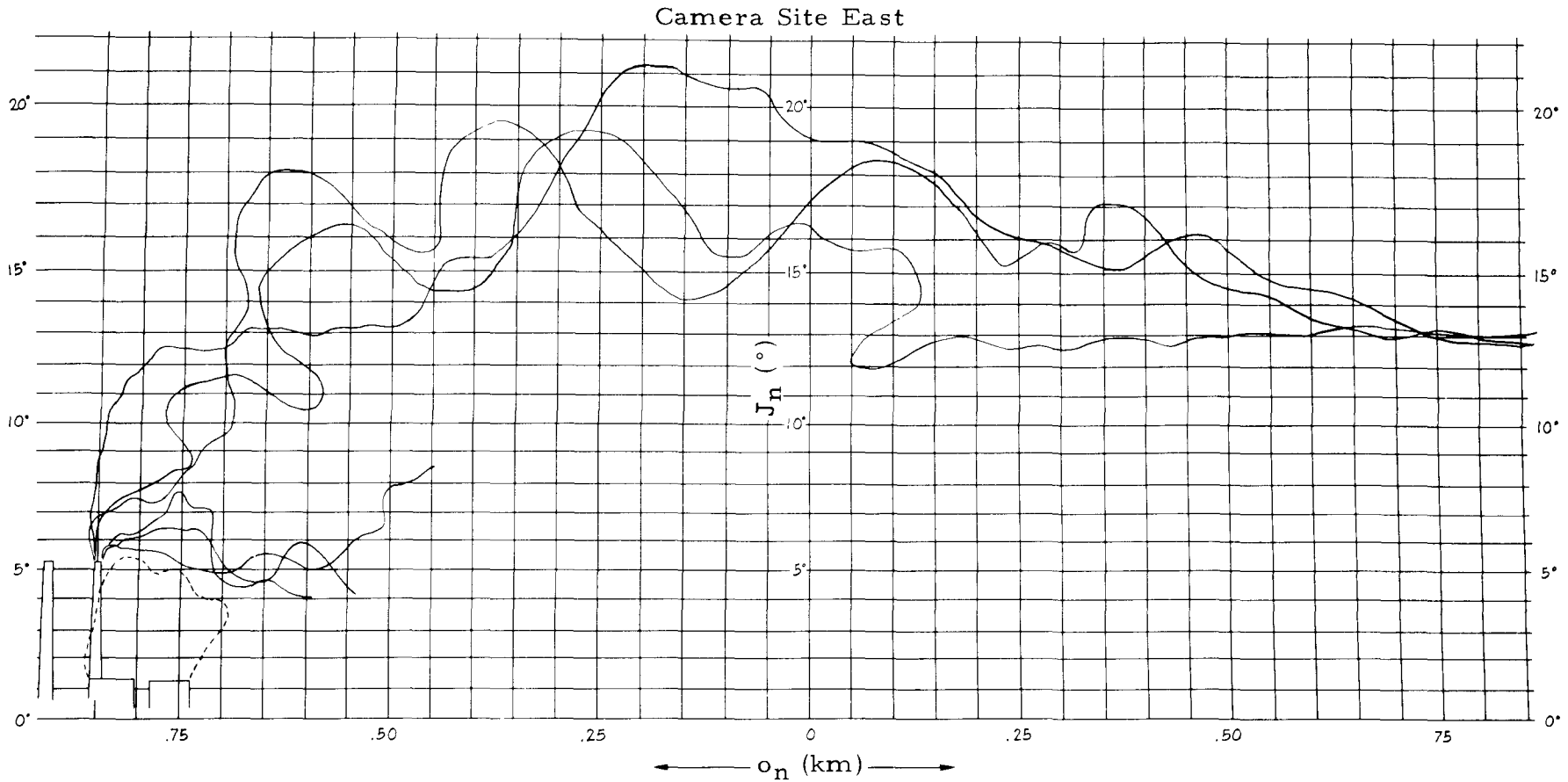

Fig. 14. PLUME PROFILE AS SEEN IN THE CAMERA PLANE THROUGH THE SOURCE

The case when the steam from the cooling towers appears to be merging with the plume and obscuring the lower boundary.

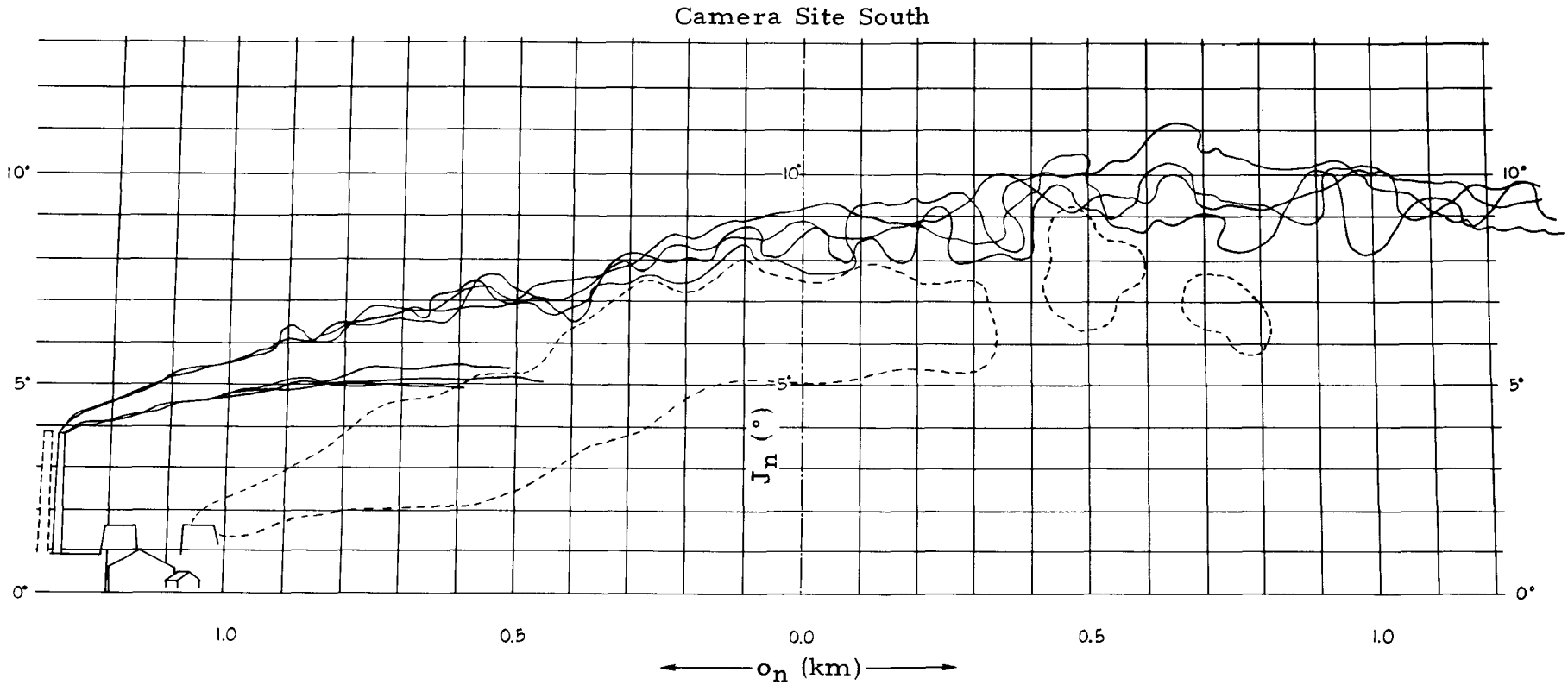

Fig. 15. PLUME PROFILE AS SEEN IN THE CAMERA PLANE THROUGH THE SOURCE

Digitization Vertical Profile of Plume

A data form was prepared for each camera site keyed to the known horizontal distance in the camera plane from the vertical photo center to each vertical line of the templates (the distances "o" - Fig. 10).

A vertical angle accurate to the nearest 0.5° was read to the plume top and plume bottom at each horizontal increment. These data were transcribed onto the data form. Appropriate data flags were used to denote when one plume edge could not be seen (always the bottom edge in this study) or when fumigation was occurring. The possibility of both occurring was not accepted. Fumigation was not defined if it could not be clearly detected visually.

The "o" values along with vertical angles from the data form were then key-punched for input to a FORTRAN IV computer program designed to calculate the true dimensions of the plume profile. These were held until wind analysis was made (see Flow Chart, Fig. 1).

Calculation of Mean Wind per Photo Period

See Fig. 16.

It can easily be seen that θ, the angle between the camera plane and the path of the smoke to be measured, is critical to calculation of acceptable plume dimensions.

Every 30 minutes during this field program, pilot balloons (pibals) were being launched from the base of the stack and tracked by two theodolites. The raw theodolite readings were processed through a standard double theodolite pibal computer program. Wind vectors were calculated and listed at the end of every 30 seconds of flight, then interpolated and listed for every 50 meters of altitude. This computer program calculates and lists error factors, rho and delta, which show the relative disagreement between readings of the theodolites. Analysis of these allows detection of wind speed or direction values attributable to incorrect theodolite readings instead of atmospheric behavior. Close study was made of all pibal data associated with the photographing periods. All questionable data were eliminated. Pibal data finally used for this study are listed in Tables I through VII.

A starting point for this work was Single-Camera Measurement of Smoke Plumes by James Halitsky, 1961. Mr. Halitsky's section, Experimental Procedure, describes clearly the obvious effects of wind fluctuations over altitude and time on the transport of stack effluent and its position relative to the camera plane. In recognition of the fact that

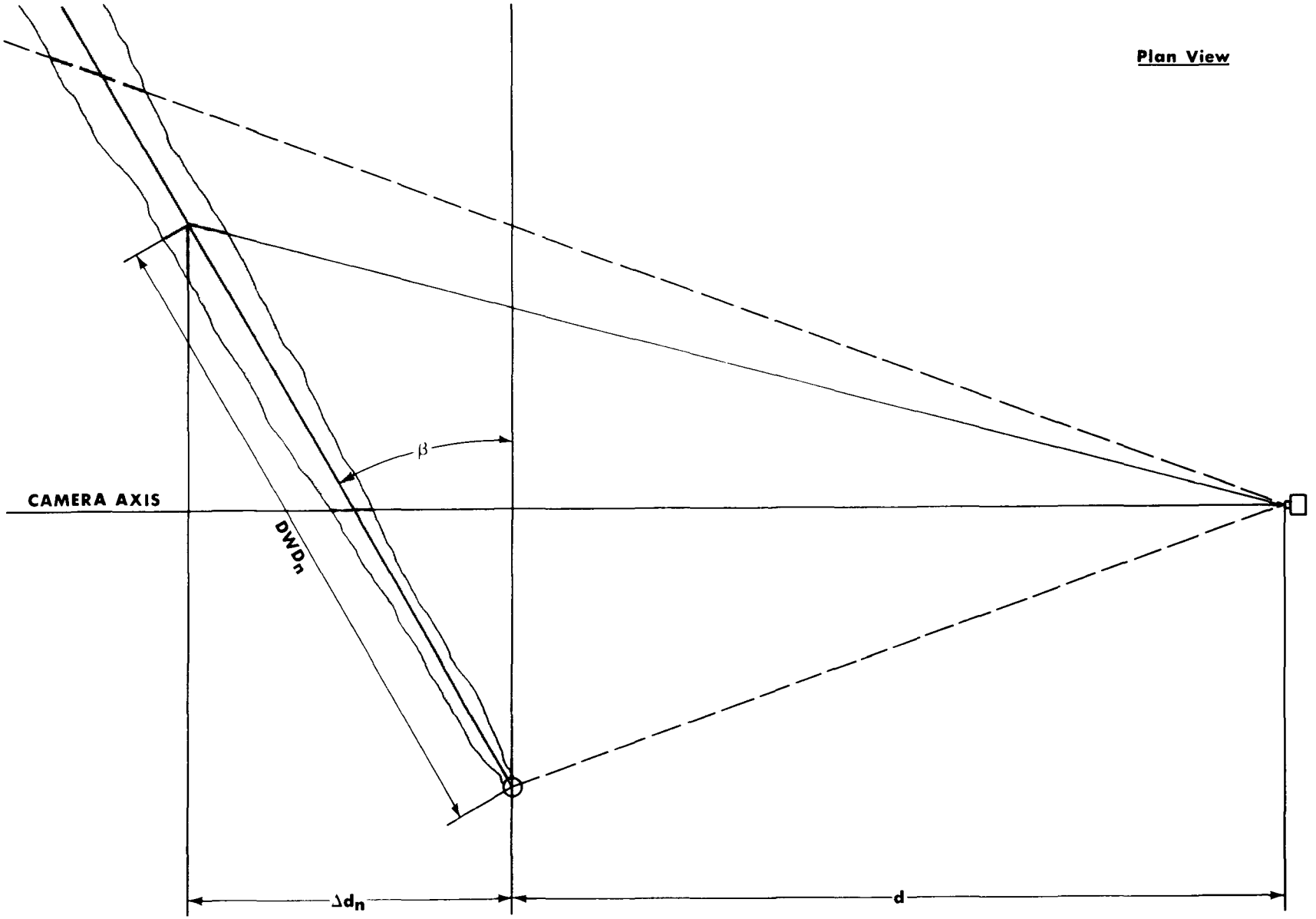

Fig. 16. HORIZONTAL GEOMETRY RELATIVE TO WIND

Table I

KEYSTONE MEAN WINDS
PIBAL DATA

October 16, 1968

Height m	1000 EDT WS m/s	1000 EDT WD Azi	1030 EDT WS m/s	1030 EDT WD Azi	1100 EDT WS m/s	1100 EDT WD Azi	Mean WS m/s	Mean WD Azi
50	0.8	92°	1.1	79°	1.7	87°	1.2	86°
100	1.9	91	2.1	90	2.0	101	2.0	94
150	2.7	100	2.4	106	2.2	119	2.4	108
200	3.3	117	3.3	122	2.5	132	3.0	134
250	3.9	144	3.5	132	3.0	136	3.5	137
300	3.5	150	4.1	146	3.6	135	3.7	144
350	3.8	157	5.1	157	5.3	147	4.7	154
400	4.8	167	6.1	164	5.7	153	5.5	161
450	6.5	176	6.0	175	6.1	158	6.2	170
500	7.4	183	6.5	184	7.0	162	7.0	176
550	5.6	199	6.2	190	6.9	178	6.2	189
600	6.0	189	5.0	189	6.7	180	5.9	186
650	5.2	180	4.4	176	5.7	177	5.1	178
700	4.5	172	3.4	157	4.6	166	4.2	165
750	4.2	168	3.4	144	4.3	155	4.0	156
800	3.5	163	4.0	137	4.0	145	3.8	148
850	2.9	155	3.2	127	3.8	127	3.3	136
900	2.4	145	3.3	114	4.1	124	3.3	128
950	2.0	120	3.8	110	4.6	120	3.5	117
1000	2.2	109	3.8	110	4.0	102	3.3	107
1050	2.3	115	2.8	104	4.2	103	3.1	107
1100	1.8	111			3.8	101	2.8	106

Mean 4.4 m/s Std. Dev. 1.3 m/s

Mean 148° Std. Dev. 27°

Table II

KEYSTONE MEAN WINDS
PIBAL DATA

October 16, 1968

Height m	1130 EDT WS m/s	WD Azi
50	3.0	157°
100	4.4	154
150	4.4	153
200	4.3	151
250	4.0	146
300	3.6	139
350	3.3	133
400	3.2	134
450	3.1	134
500	2.9	137
550	2.7	141
600	2.8	144
650	3.6	142
700	4.1	143
750	4.2	145
800	5.2	154

Mean 3.56 m/s Std. Dev. 0.722 m/s

Mean 141° Std. Dev. 6.1°

Table III

KEYSTONE MEAN WINDS
PIBAL DATA

October 17, 1968

Height	0930 EDT		1000 EDT		1030 EDT		Mean	
	WS	WD	WS	WD	WS	WD	WS	WD
m	m/s	Azi	m/s	Azi	m/s	Azi	m/s	Azi
50	0.8	95°	1.2	131°	0.8	154°	0.9	127°
100	1.9	115	2.0	147	1.5	155	1.8	139
150	2.8	126	2.7	160	1.6	156	2.4	147
200	4.1	140	4.2	162	1.8	156	3.4	153
250	6.2	152	4.6	158	2.5	149	4.4	153
300	6.9	160	5.1	153	3.4	144	5.1	152
350	7.9	164	5.9	150	3.7	161	5.8	158
400	8.5	171	6.1	153	4.5	183	6.4	169
450	8.9	179	6.6	159	5.9	179	7.1	172
500	9.2	185	7.5	166	6.8	186	7.8	179
550	9.4	189	8.3	172	7.3	188	8.3	183
600	9.8	192	9.1	179	7.9	191	8.9	187
650	10.4	192	9.9	189	8.6	195	9.6	192
700	9.6	195	10.1	194	8.7	197	9.5	195
750	9.1	197	10.1	196	8.4	197	9.2	197
800	9.0	197	9.6	195	8.0	195	8.9	196
850	7.2	195	7.8	192	7.4	194	7.5	194
900	7.4	192	5.1	200	6.0	199	6.2	197
950	8.3	193	5.9	203	7.0	199	7.1	198
1000	8.2	198	7.2	203	8.3	198	7.9	200

Mean 7.5 m/s Std. Dev. 1.6 m/s

Mean 183° Std. Dev. 16.8°

Table IV

KEYSTONE MEAN WINDS
PIBAL DATA

October 17, 1968

Height m	1200 EDT WS m/s	1200 EDT WD Azi	1230 EDT WS m/s	1230 EDT WD Azi	Mean WS m/s	Mean WD Azi
50	2.5	125°	2.7	131°	2.6	128°
100	4.3	139	4.2	134	4.25	136
150	4.7	140	4.0	138	4.35	139
200	4.6	136	4.6	154	4.6	145
250	4.4	138	3.9	158	4.15	148
300	4.5	151	4.9	151	4.7	151
350	4.2	157				
400	4.0	162				
450	4.3	160				
500	4.8	165				
550	4.8	165				
600	4.4	166				
650	4.2	160				
700	3.9	159				
750	4.3	164				
800	4.2	171				
850	4.6	174				
900	5.2	175				

Mean 4.4 m/s Std. Dev. 0.36 m/s

Mean 163° Std. Dev. 7.8°

Table V

KEYSTONE MEAN WINDS
PIBAL DATA

October 18, 1968

Height	0830 EDT		0900 EDT		0930 EDT		Mean	
	WS	WD	WS	WD	WS	WD	WS	WD
m	m/s	Azi	m/s	Azi	m/s	Azi	m/s	Azi
50	1.4	86°	1.5	90°	0.8	98°	1.2	91°
100	3.3	102	2.6	104	2.1	121	2.7	109
150	4.7	114	3.5	120	3.5	133	3.9	122
200	5.9	125	4.6	136	4.8	142	5.1	134
250	7.2	136	5.7	146	5.7	146	6.2	143
300	8.1	144	6.9	151	6.4	150	7.1	148
350	8.4	150	8.1	156	7.0	153	7.8	153
400	8.6	153	8.9	156	7.8	156	8.4	155
450	9.3	152	9.9	154	9.2	159	9.5	155
500			10.3	160	9.2	163	9.8	162
550			10.1	165	10.8	165	10.4	165
600			10.3	170	12.2	166	11.2	168
650			11.9	173	12.8	167	12.3	170
700			12.6	177	11.4	174	12.0	175
750			13.1	182	13.7	175	13.4	178
800			12.4	191	16.7	176	14.5	183
850			13.0	192	13.8	188	13.4	190
900			14.0	190	16.4	187	15.2	188
950			11.6	200	18.1	188	14.8	194
1000			11.7	198	19.3	188	15.5	193
1050			9.4	204	11.3	203	10.3	203
1100			10.3	204	14.6	195	12.4	200
1150					18.1	190		
1200					7.6	205		
1250					9.4	195		

Mean 11.3 m/s Std. Dev. 2.9 m/s

Mean 173.5° Std. Dev. 18.6°

Table VI

KEYSTONE MEAN WINDS
PIBAL DATA

October 20, 1968

Height m	1230 EDT WS m/s	WD Azi
50	2.2	310°
100	3.0	309
150	3.0	307
200	2.6	284
250	2.2	262
300	2.1	248
350	2.6	248
400	3.1	251
450	3.6	264
500	4.2	273
550	5.1	275
600	6.0	275
650	7.0	275
700	7.1	274
750	8.1	282
800	9.5	289

Mean 5.0 m/s Std. Dev. 2.5 m/s

Mean 268° Std. Dev. 13.4°

Table VII

KEYSTONE MEAN WINDS
PIBAL DATA

October 21, 1968

Height	0830 EDT		0900 EDT		0930 EDT		Mean	
	WS	WD	WS	WD	WS	WD	WS	WD
m	m/s	Azi	m/s	Azi	m/s	Azi	m/s	Azi
50	2.7	284°	1.5	278°	1.7	288°	2.0	283°
100	4.7	288	3.3	286	3.1	295	3.7	289
150	6.3	294	5.0	291	4.5	304	5.2	296
200	7.8	300	6.1	296	6.1	310	6.7	302
250	8.4	305	6.8	308	7.4	314	7.5	309
300	8.7	309	9.2	305	7.9	316	8.6	310
350	8.7	312	10.5	305	7.5	316	8.9	311
400	8.4	317	8.2	312	7.6	317	8.0	315
450	8.5	323	8.3	318	7.9	318	8.2	320
500	9.0	326	8.6	322	7.4	318	8.3	322
550	9.2	329	8.5	324	7.1	319	8.3	324
600	7.5	331	7.7	323	7.5	322	7.6	325
650	8.4	326	8.4	322	8.1	325	8.3	324
700	9.6	322	8.4	325	8.7	327	8.9	325
750	8.6	322	8.4	326	8.1	329	8.4	326
800	9.4	321	8.1	326	8.5	329	8.7	325
850	8.1	322	8.8	326	8.8	329	8.6	326
900	7.3	324	10.0	325	9.1	327	8.8	325
950	8.9	323	11.6	324	10.2	326	10.2	326
1000	10.9	323	8.1	328	9.8	326	9.6	326
1050	5.8	326	6.2	328	9.6	326	7.2	327
1100	10.5	323	8.8	326	9.8	327	9.7	325
1150	11.3	323	9.1	326	8.3	325	9.6	324
1200			7.2	328			7.2	328

Mean 8.5 m/s Std. Dev. 0.8 m/s

Mean 322° Std. Dev. 5.9°

Table VIII

LOG OF MEAN WIND PER PHOTO PERIOD

Photo Period	Date 1968	Time	Pibal Launch Times	Mean Wind Speed m/s	Mean Wind Std. Dev. m/s	Mean Wind Direction TN Azi.	Mean Wind Std. Dev.
1	Oct. 16	1000-1110	1000 1030 1100	4.4	1.3	148°	27.0°
	(Smoke blowing nearly parallel to camera axis, no confidence in plume profile)						
2	Oct. 16	1110-1130	1130	3.6	0.7	141	6.1
3	Oct. 17	0930-1030	0930 1000 1030	7.5	1.6	183	16.8
4	Oct. 17	1200-1230	1200 1230	4.4	0.36	163	7.8
5	Oct. 18	0840-0925	0830 0900 0930	11.3	2.9	173	18.6
6	Oct. 20	1300-1400	1230	5.0	2.5	268	13.4
7	Oct. 21	0840-0925	0830 0900 0930	8.5	0.8	322	5.9
	(Plume blowing closer to camera than source plane)						

these fluctuations could introduce error, careful consideration was given to Mr. Halitsky's section, Evaluation of Errors. His calculation of errors was based upon a single ground-level wind direction recorder. Since Keystone stack is 244 meters high and effluent is known to be transported to >1000 meters above the ground, a four-dimensional study was indicated for true photographic error analysis. Such a temporal and spatial experiment could lead to higher order and more significant photographic measurement of plume transport and diffusion.

Since the work herein described was still at the feasibility stage, it was decided to repeat Mr. Halitsky's assumption of a mean wind speed and direction for each photographing period. Immediately, it was obvious that the accuracy of the true vertical dimensions of the plume profile is critically dependent upon the calculation of the mean wind vector. Since pibal data were grouped over time periods, it was necessary to ascertain that pibal data were grouped into time periods during which atmospheric conditions were relatively constant. This partially explains the iterative loop "A" in the system flow chart (Fig. 1). The transitional periods of atmospheric change are not instantaneous and it is during these periods that plume behavior is most unpredictable. The photogrammetric technique along with high-order wind data and ground sampling could yield new insights into diffusion of effluent during transition for a small cost. Predictive plume models are, at present, confined primarily to constant, known atmospheric conditions. The models would benefit from knowledge of the probabilities of ground pollution during highly transient meteorological conditions.

From the pibal data, mean wind speed and direction along with their standard deviations (Table VIII) were calculated for each photo period covering the atmosphere from stack top to estimated plume top. No winds below stack top were used in calculation of mean wind but they are displayed for each photo period along with temperature and plume profiles, as we will see later. It should be noted that because winds well aloft were finally considered important and a storm front passed over the area during the days of this field work, some sizable standard deviations resulted. This was applied as a confidence factor. Also, pibal data do not yield the vertical wind vector (z and sigma z) for inclusion. Accurate high-quality field measures of the z component could serve as a basis for interesting future work as it is considered by meteorologists to be an important diffusion factor.

Incremental True Downwind Distances

(See Fig. 17 for graphic definition of variables.)

When a mean wind plane is established for a given time-series of photographs, the angle, β, can be calculated and the translation of

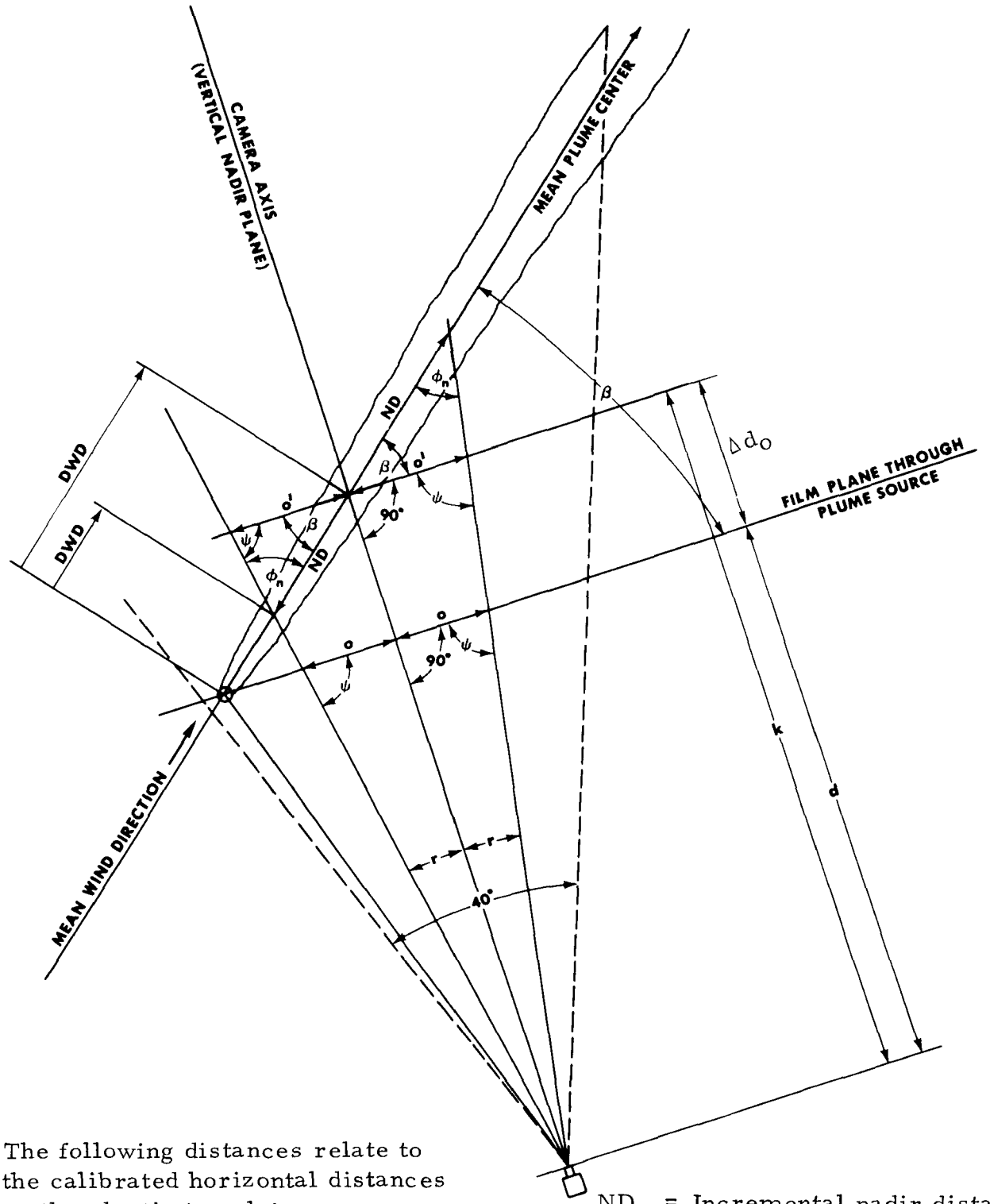

The following distances relate to the calibrated horizontal distances on the plastic templates:

$r = r_n$
$o = o_n$
$o' = o'_n$
$\psi = \psi_n$
$DWD = DWD_n$
$ND = ND_n$

Other values are constant for each photo period.

ND_n = Incremental nadir distance in mean wind plane

ND_{max} = DWD from stack to nadir plane

o_{max} = Horizontal distance from the camera axis to the stacks in the film plane through plume source

DWD_{max} = Longest visible DWD per photo period

Fig. 17. HORIZONTAL PHOTOGRAMMETRIC GEOMETRY

horizontal distances in the camera plane through the source as measured by the plastic template to actual downwind distances (DWD_n) is a simple trigonometric calculation. All azimuth angles are referenced to true north (TN) for consistency*.

Procedure for calculation of true incremental downwind distances

1. $$\tan \psi_n = \frac{d}{o_n} \quad \text{and} \quad \tan r_n = \frac{o_n}{d} \tag{1,2}$$

2. $$o'_n = k \tan r_n \tag{3}$$

To calculate ND_n from the vertical nadir plane in the upwind direction:

3A. Since $$\Phi_n = 180° - (\psi_n + \beta) \tag{4}$$

and $$\sin \Phi_n = \sin [180° - (\psi_n + \beta)]$$

and $$\sin \Phi_n = \sin (180° - \Phi_n)$$

then $$\sin (180° - \Phi_n) = \sin [180° - (\psi_n + \beta)]$$

and $$\sin \Phi_n = \sin (\psi_n + \beta)$$

therefore $$\sin \Phi_n = \sin \psi_n \cos \beta + \cos \psi_n \sin \beta \,. \tag{5}$$

To calculate ND_n for incremental distances from the vertical nadir plane in the downwind direction:

3B. Formula (4) above becomes

$$\Phi_n = 180° - [\beta + (180° - \psi_n)]$$

then $$\sin \Phi_n = \sin (\psi_n - \beta)$$

therefore $$\sin \Phi_n = \sin \psi_n \cos \beta - \cos \psi_n \sin \beta \,. \tag{6}$$

NOTE: 3A and 3B apply to the geometry as shown in Fig. 17. It must be remembered that for the case when the mean wind is transporting

*It should be noted that lidar geometry is referenced to magnetic north. There are six degrees of magnetic declination at Keystone, Pennsylvania.

the plume closer to the camera site than the film plane through the source rather than away from it, as was the case in photo period #7, these formulas must be used in reverse order. (6) applies to upwind half and (5) applies to downwind half of photo.

4. By the Law of Sines, then:

$$\frac{ND_n}{\sin \psi_n} :: \frac{o'_n}{\sin \Phi_n}$$

$$\therefore \quad ND_n = \frac{o'_n \sin \psi_n}{\sin \Phi_n} \tag{7}$$

5. True incremental downwind distances from the stacks to the center of the photo are computed:

$$DWD_n = ND_{max} - ND_n$$

6. True incremental downwind distances from the center of the photo to the last downwind calibration:

$$DWD_n = ND_{max} + ND_n$$

The calculated true downwind distances were key-punched to be used as input to a computer program in the next step of the analysis. In all, the loop "A" in the system flow chart, Fig. 1, was iterated three times. The above DWD 's were recalculated each time as the time periods were redefined. Forms were designed for rapid recalculation. Many of the values remained constant, only those dependent on the angle β changed, thus great flexibility in looking at the effects of the time factor on the mean wind plane was possible.

The necessity for this iteration loop could easily be eliminated in future work if three things were done (Slawson, 1967):

(1) Detailed observer's notes kept by a meteorologist at the camera station.

(2) Complete and accurate four-dimensional measurements of atmospheric parameters, temperature, wind speed and direction, pressure, humidity, etc., from the ground to at least a predetermined distance above the top of the plume at frequent intervals.

(3) All data precisely keyed to time and location.

Computer Calculation and Statistical Analysis of Plume Profile

See Figs. 18, 19, 20, and 21 for typical output.

Calculation of the incremental vertical plume profile per photo period was the final mathematical operation needed. Since there were 170 digitized tracings each containing as many as 35 increments and it was planned to redefine the time periods for repeated runs if the results were not meaningful meteorologically, a simple computer program was written for economy.

Inputs:

d in meters, one for each camera site.
sin β, one for each time period.
DWD_n, one set for each time period.
o in meters
Elevation angles from digitization of tracings (J_n, Fig. 16) } one set for each photo

The following calculations were made and listed (Fig. 22) for each photo during a series. (See Table IX)

$$\Delta d_n = DWD_n \sin \beta$$

$$D+DD_n = d + \Delta d_n$$

Each increment has two values for q_n, q_{top} is the height of the visible plume top, and q_{bottom} is the height of the visible base of the plume above the camera elevation at the same true downwind distance (DWD_n)

$$q_n = D + DD_n \tan J_n$$

These incremental plume dimensions are listed by the computer in both feet and meters. A "999" flag was used when a part of the plume outline could not be detected on the photos and data were ended when both plume dimensions faded. The key for visible fumigation was use of a very small angle based on the mean angle to the horizon for each camera site, 0.1° for Site East and 2.0° for Site South.

Input data as well as processed results are listed in the output of the computer program. All of the q_{top} and q_{bottom} values were saved on magnetic tape. This was used as input to a second phase of the computer program which, when instructed how to group the photos, computes a

ARL PROJECT 18013B-53 PLUME PHOTOGRAPHY
PHOTO PERIOD 5, SIN B = .72090 31 TH SLIDE THIS PERIOD.

N	D*D	D+DD	TOP	BOTTOM	METERS Q TOP	METERS Q BOTTOM	FEET Q TOP	FEET Q BOTTOM
1	0	3700.0	4.5	4.0	291	259	955	849
2	53	3738.2	5.0	4.5	327	294	1073	965
3	165	3818.9	6.0	4.5	401	301	1317	986
4	282	3903.3	6.0	4.5	410	307	1346	1008
5	404	3990.5	6.0	4.0	414	279	1376	916
6	530	4082.1	6.0	2.0	429	143	1408	468
7	663	4178.0	6.0	2.0	439	146	1441	479
8	802	4278.2	7.0	2.0	525	149	1723	490
9	948	4383.4	7.0	2.0	536	153	1766	502
10	1102	4494.4	7.5	2.0	592	157	1941	515
11	1265	4611.9	7.5	2.0	607	161	1992	528
12	1435	4734.5	7.5	2.0	623	165	2045	542
13	1614	4863.5	7.5	2.0	640	170	2101	557
14	1803	4999.6	7.5	2.0	658	175	2160	573
15	2003	5144.0	8.5	2.0	769	180	2522	589
16	2215	5296.8	9.0	2.0	839	185	2752	607
17	2441	5459.7	9.0	2.0	865	191	2837	626
18	2683	5634.2	9.0	2.0	892	197	2928	646
19	2938	5818.0	9.5	2.0	974	203	3194	667
20	3210	6014.1	9.5	2.0	1006	210	3302	689
21	3503	6225.3	9.5	2.0	1042	217	3418	713
22	3815	6450.2	9.0	2.0	1022	225	3352	739
23	4152	6693.2	9.0	2.0	1060	234	3478	767
24	4514	6954.1	9.0	2.0	1101	243	3614	797
25	4907	7237.5	9.0	2.0	1146	253	3761	829
26	5335	7546.0	9.0	2.0	1195	264	3921	865

Camera Site South.
Fumigation visible down to mean horizon of 2.0°

Fig. 18. PLUME GEOMETRY, DIGITAL OUTPUT

SRI PROJECT 18013R-53 PLUME PHOTOGRAPHY
PHOTO PERIOD 3, SIN B = .48390 7 TH SLIDE THIS PERIOD.

N	D/D	D+DD	TOP	BOTTOM	METERS Q TOP	METERS Q BOTTOM	FEET Q TOP	FEET Q BOTTOM
1	0	2380.0	7.0	5.5	292	229	959	752
2	48	2403.2	8.0	7.0	336	295	1108	968
3	98	2427.4	9.0	6.5	384	277	1261	907
4	148	2451.6	10.0	6.0	432	258	1418	845
5	199	2476.3	11.0	6.0	481	260	1579	854
6	251	2501.5	11.0	6.0	486	263	1595	863
7	304	2527.1	10.5	6.0	466	266	1537	871
8	359	2553.7	10.0	6.5	450	291	1477	955
9	414	2580.3	11.0	7.0	502	317	1646	1039
10	471	2607.9	11.0	6.0	507	274	1663	899
11	528	2636.5	11.5	4.5	536	207	1759	681
12	587	2664.0	12.5	3.5	591	257	1938	842
13	648	2693.6	13.0	6.0	622	283	2040	929
14	711	2724.1	12.5	5.0	604	238	1981	782
15	773	2754.1	13.0	5.5	636	265	2086	870
16	837	2785.0	13.0	5.0	643	244	2109	799
17	904	2817.4	12.5	5.0	625	246	2049	809
18	971	2849.9	12.5	4.5	632	224	2073	736
19	1040	2883.3	12.5	3.5	639	176	2097	579
20	1111	2917.6	12.5	1.5	647	76	2122	251
21	1184	2952.9	11.0	.1	574	5	1883	17
22	1257	2988.3	11.5	.1	608	5	1995	17
23	1333	3025.0	12.0	.1	643	5	2110	17
24	1411	3062.8	12.0	.1	651	5	2136	18
25	1492	3102.0	12.0	.1	659	5	2163	18
26	1573	3141.2	12.5	.1	696	5	2285	18
27	1657	3181.8	12.5	.1	705	6	2314	18
28	1744	3223.9	12.5	.1	715	6	2345	18
29	1833	3267.0	12.5	.1	724	6	2376	19
30	1924	3311.0	12.5	.1	734	6	2408	19
31	2018	3356.5	13.0	.1	775	6	2542	19
32	2114	3403.0	13.0	.1	786	6	2578	19
33	2213	3450.9	14.0	.1	869	6	2823	20
34	2315	3500.2	14.0	.1	873	6	2863	20
35	2420	3551.0	14.0	.1	885	6	2905	20

Camera site East
Fumigation visible down to mean horizon of 0.1°

Fig. 19. PLUME GEOMETRY, DIGITAL OUTPUT

MRI PROJECT 18013-53 PLUME PHOTOGRAPHY
PHOTO PERIOD 3, SIN B = .44390 1 IN SLIDE THIS PERIOD.

N	DWD	D+DD	TOP	BOTTOM	METERS Q TOP	METERS Q BOTTOM	FEET Q TOP	FEET Q BOTTOM
1	0	2380.0	6.5	5.5	271	229	890	752
2	48	2403.2	7.0	6.0	295	253	968	829
3	98	2427.4	8.0	6.0	341	255	1119	837
4	148	2451.6	8.0	6.0	345	258	1130	845
5	199	2476.3	8.5	6.0	370	260	1214	854
6	251	2501.5	8.5	6.0	374	263	1227	863
7	304	2527.1	9.0	6.0	400	266	1313	871
8	359	2553.7	9.0	6.0	404	268	1327	881
9	414	2580.3	9.5	6.0	432	271	1417	890
10	471	2607.9	9.0	6.5	413	297	1355	975
11	528	2635.5	10.0	6.5	465	300	1525	985
12	587	2664.0	10.0	6.5	470	304	1541	996
13	648	2693.6	10.5	7.0	499	331	1638	1085
14	711	2724.1	10.0	8.0	480	383	1576	1256
15	773	2754.1	10.5	6.0	510	289	1675	950
16	837	2785.0	10.5	6.5	516	317	1693	1041
17	904	2817.4	11.0	7.0	548	346	1797	1135
18	971	2849.9	11.0	7.5	554	375	1817	1231
19	1040	2883.3	11.0	7.5	560	380	1839	1245
20	1111	2917.6	11.0	6.5	567	332	1861	1091
21	1184	2952.9	11.0	7.5	574	389	1883	1275
22	1257	2988.3	11.5	8.0	608	420	1995	1378
23	1333	3025.0	11.0	6.5	588	345	1929	1131
24	1411	3062.8	11.0	7.0	595	376	1953	1234
25	1492	3102.0	10.5	7.0	575	381	1886	1250
26	1573	3141.2	10.5	7.0	582	386	1910	1265
27	1657	3181.8	10.5	6.5	590	363	1935	1189
28	1744	3223.9	12.0	6.5	685	367	2248	1205
29	1833	3267.0	12.0	6.0	694	343	2278	1127
30	1924	3311.0	11.5	6.0	674	348	2210	1142
31	2018	3356.5	11.0	6.0	652	353	2141	1157
32	2114	3403.0	11.0	6.0	661	358	2170	1173
33	2213	3450.9	11.0	7.0	671	424	2201	1390
34	2315	3500.2	11.5	7.5	712	461	2336	1512
35	2420	3551.0	12.0	8.0	755	499	2476	1637

Top and Bottom profiles of plume visible at each horizontal increment

Fig. 20. PLUME GEOMETRY, DIGITAL OUTPUT

SRI PROJECT 180134-53 PLUME PHOTOGRAPHY
PHOTO PERIOD 5, SIN B = .63020 10 TH SLIDE THIS PERIOD.

N	DWD	D+DD	TOP	BOTTOM	METERS Q TOP	METERS Q BOTTOM	FEET Q TOP	FEET Q BOTTOM
1	0	2380.0	6.5	5.5	271	229	890	752
2	52	2412.8	7.5	6.0	318	254	1042	832
3	105	2446.2	8.0	6.0	344	257	1128	844
4	158	2479.6	8.5	6.5	371	283	1216	927
5	213	2514.2	9.0	6.0	398	264	1306	867
6	269	2549.5	9.0	6.0	404	268	1325	879
7	327	2586.1	9.0	6.0	410	272	1344	892
8	387	2623.9	8.5	6.0	392	276	1287	905
9	448	2662.3	9.0	6.0	422	280	1383	918
10	512	2702.7	9.0	5.5	428	260	1404	854
11	578	2744.3	9.5	5.5	457	264	1507	867
12	644	2785.8	10.0	5.5	491	268	1612	880
13	714	2830.0	10.0	5.0	499	248	1637	812
14	785	2874.7	10.0	5.0	507	252	1663	825
15	860	2922.0	10.0	99.9	515	0	1690	0
16	933	2968.0	10.5	99.9	550	0	1805	0
17	1015	3019.7	10.0	99.9	532	0	1747	0
18	1096	3070.7	9.5	99.9	514	0	1686	0
19	1179	3123.0	9.5	99.9	523	0	1715	0
20	1270	3180.4	9.5	99.9	532	0	1746	0
21	1357	3235.2	9.0	99.9	512	0	1681	0
22	1452	3295.1	9.0	99.9	522	0	1712	0
23	1549	3356.2	9.0	99.9	532	0	1744	0
24	1651	3420.5	9.0	99.9	542	0	1777	0
25	1755	3486.0	9.0	99.9	552	0	1811	0
26	1865	3555.3	9.0	99.9	563	0	1847	0
27	1978	3626.5	9.0	99.9	574	0	1884	0
28	2097	3701.5	9.0	99.9	586	0	1923	0
29	2219	3778.4	9.0	99.9	598	0	1963	0
30	2349	3860.3	9.0	99.9	611	0	2006	0

SAMPLE

Lower boundary of plume not visible

Fig. 21. PLUME GEOMETRY, DIGITAL OUTPUT

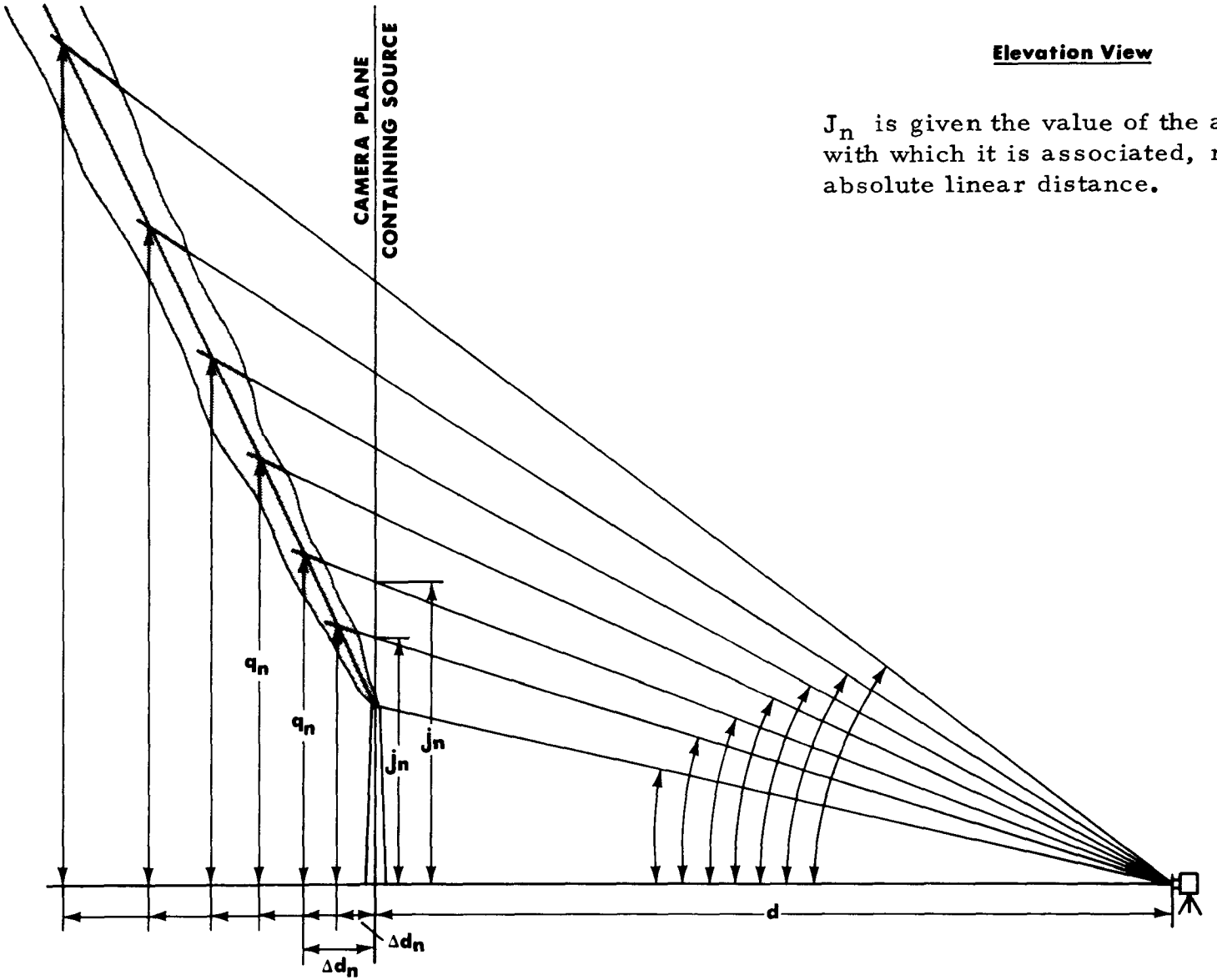

Elevation View

J_n is given the value of the angle with which it is associated, not absolute linear distance.

Fig. 22. ELEVATION GEOMETRY

temporal mean q_{top} and mean q_{bottom} along with their standard deviations over a series of pictures at each downwind distance (DWD). These were studied and, when necessary, plotted next to the wind and temperature profiles. Then, it could quickly be determined whether the wind data had been grouped into periods of definable meteorological conditions or whether a transition such as stable to unstable had occurred which would cause wild standard deviations in the plume outline introducing an intolerable error in measurement of the transport and diffusion of stack effluent.

Table IX

VALUE OF VARIABLES FOR EACH PHOTO PERIOD

	1968						
	Oct. 16 1000 to 1110 EDT	Oct. 16 1110 to 1130 EDT	Oct. 17 0930 to 1030 EDT	Oct. 17 1200 to 1400 EDT	Oct. 18 0840 to 0945 EDT	Oct. 20 1300 to 1400 EDT	Oct. 21 0840 to 0945 EDT
	Period 1	Period 2	Period 3	Period 4	Period 5	Period 6	Period 7
Constants per photo period:							
d	2380 m	2380 m	2380 m	2380 m	2380 m	3700 m	3700 m
Δd_o	1500 m	2100 m	470 m	950 m	690 m	1300 m	-150 m*
σ_{max}	850 m	850 m	850 m	850 m	850 m	1250 m	1250 m
β	63°	70°	28°56'	48°11'	39°04'	46°07'	6°51'
$k(d+\Delta d_o)$			2850 m	3330 m	3070 m	5000 m	3550 m
Calculated							
tan β	Standard deviation of winds and β considered too large for confidence (See Figs. 2 and 3)	β too large, smoke blowing almost parallel to camera axis.	0.55294	1.11765	0.81176	1.0400	-0.1200
cos β			0.87511	0.66677	0.7764	0.6930	-0.99288
sin β			0.48390	0.74526	0.6302	0.7209	-0.11913**
ND_{max}			971 m	1274 m	1096 m	1803 m	1266 m
DWD_{max}			2420 m	4242 M	3084 m	5335 m	2388 m

*Negative sign, establishes relation of wind to camera.

**Negative sign used only for computer calculation of plume profile. Absolute values used for computing DWD_n.

NOTE: See Figs. 2 through 8 for relative positions of plume and camera for each photo period and Table 8 for mean winds.

Data Displays

This photogrammetric analysis was undertaken primarily to provide graphic displays of true plume behavior for meteorological analysis of the stack effluent diffusion. It was hoped that plots could be drawn from which the calculations of computer plume models could be confirmed or denied. There was need to know the mean plume center line, mean plume rise, evidences of "overshoot" in the profile, and determine confidence in this calculated mean center line.

The data output from the computer statistical analysis was plotted at a large scale (1" = 100 m). These working plots were simply photo-reduced for inclusion in this report (Fig. 23 is a representative example). Display of the mean plume top and its incremental standard deviations was straightforward. Behavior of the bottom profile required a subjective analysis of each calculated profile in a time period. Each plot is annotated with information considered germane to the profile displayed. The standard deviations of the visible base of the plume were individually studied because the real-life diffusion became obscured over some time periods through grouping of data. Standard deviation of the movement of the plume base is displayed on these plots only to the point where all effluent could be confirmed as being airborne, a short distance downwind of the stacks in most cases (see computer output, Figs. 18 through 21). Beyond this point, individual profiles are shown and identified as to time in order to retain the nature of the movement.

Due to the limitations of photography used for this study, it is not expected to attain a high degree of correlation between instantaneous plume base and values for low or ground level sampling of pollutants. If the field photography were improved and with better coordination of field activities, a good correlation of these values should be attainable.

Locations of lidar profiles were not plotted on camera geometry base maps (Figs. 2 through 8) because of time limitations. This set of figures illustrates why the data for photo periods #1 and #2 on October 16, 1968, was not considered reliable enough for inclusion. The smoke was blowing almost away from the camera and the angle between the plume and the camera plane became too great for photogrammetric confidence.

MRI has been studying the photographic-microdensitometer method for measurement of airborne matter as designed by Dr. Sander Veress, University of Washington (1969). Through the use of well-controlled photography, i.e., film, developing, lens, camera, light polarization, etc., Dr. Veress has been able to achieve 0.89 correlation with visibility measurements of the nephelometer and define the dimensions of layers of polluted air far more accurately than visible detections. The value of this method is currently being explored by researchers in several aspects

Photo Period 3, October 17, 1968, 0930-1030 EDT, Camera Site East

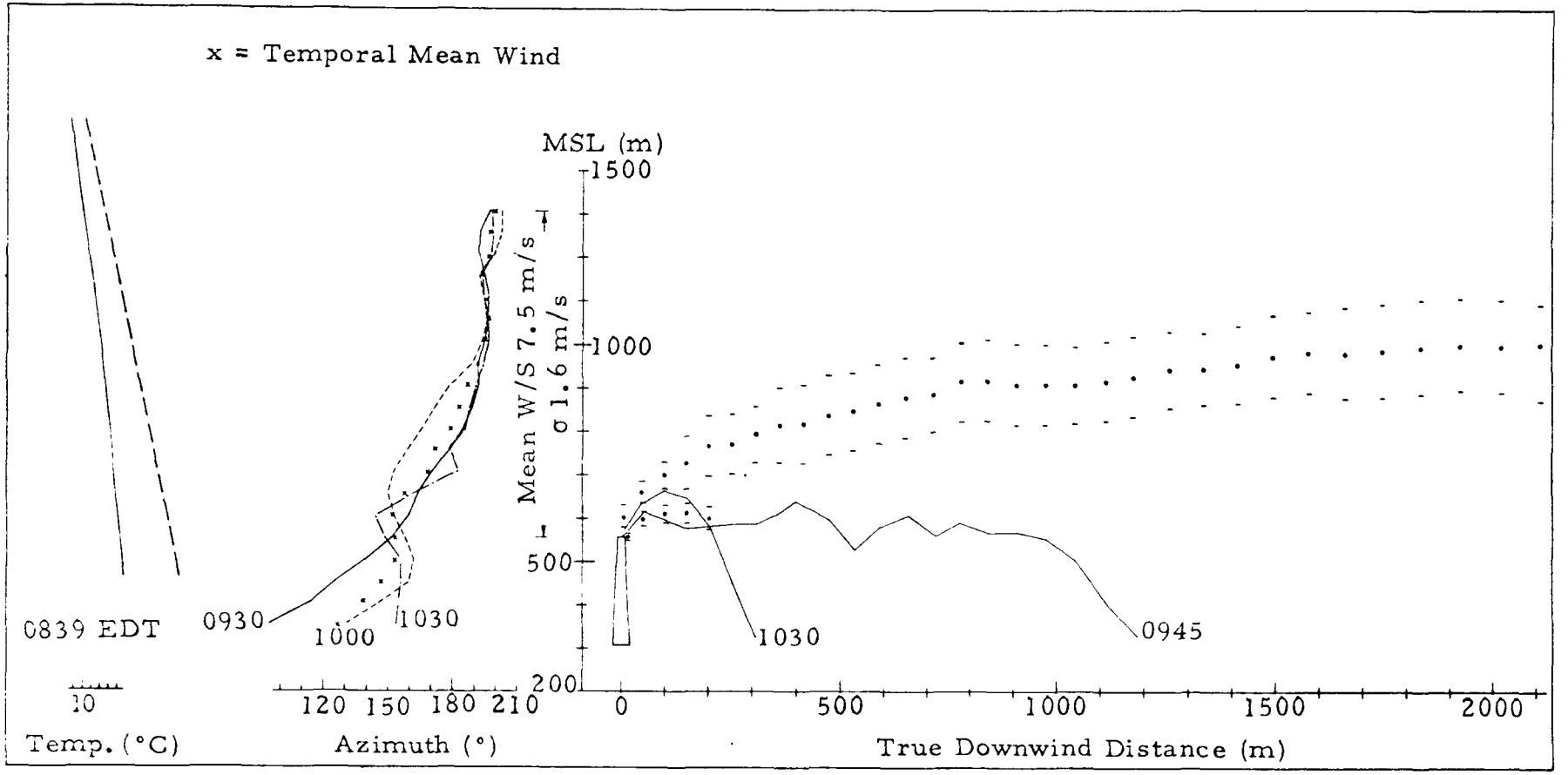

Fig. 23. EXAMPLE OF TRUE PLUME PROFILE AND ENVIRONMENT CHARACTERISTICS

of remote sensing (Journal of Photogrammetric Engineering, October 1969). Results seem to indicate that it may soon be possible to produce pollution concentration maps and profiles of high quality inexpensively with photography alone.

Appendix B

INDEX TO TYPE AND DATE OF DATA RUNS

The 110 distinct portions of the data acquisition missions of the airplane are put into consistent categories, labeled by a code number.

INDEX

TYPE AND DATE OF DATA RUN BY SEQUENCE NUMBER

Code
#

H = data plotted horizontally as a function of distance flown.
V = data plotted vertically as a function of altitude.

01-H Across the plume, 2 miles downwind of Keystone stacks. Eight sections of precipitators off.

Oct. 15	1, 2, 3, 4, 5, 6
Oct. 16	17, 18, 28, 30
Oct. 17	37, 38, 39, 40, 41, 42
Oct. 20	75, 76, 77, 78, 79, 80
Oct. 21	89, 90, 91

51-H Two miles downwind of Keystone stacks. Precipitators on for 20 minutes before this series.

Oct. 22	95, 96, 97, 98, 99, 100, 101, 102

02-H Across plume, 5 miles downwind of Keystone stacks. Eight section of precipitators off.

Oct. 15	7, 8, 9
Oct. 16	15, 16, 31, 32, 33
Oct. 17	43, 44, 45, 46, 47, 48, 57, 58, 59, 60, 61, 62

03-H Across plume, 10 miles downwind of Keystone stacks. Eight sections of precipitators off.

Oct. 16	13, 14
Oct. 17	49, 50, 51, 52
Oct. 18	67, 68, 69, 70
Oct. 20	81, 82

04-H Along plume downwind from Keystone stacks.

Oct. 15	10
Oct. 16	19
Oct. 18	73

05-H Along plume upwind to Keystone stacks.

Oct. 15	11
Oct. 16	34

Code #		
06-V	Descending straight traverse of plume 2 miles downwind of Keystone stacks.	
	Oct. 16	20
07-V	Descending straight traverse of plume 5 miles downwind of Keystone stacks.	
	Oct. 16	21
08-V	Descending straight traverse of plume 10 miles downwind of Keystone stacks.	
	Oct. 16	22
09-V	Ascending spiral upwind of Keystone stacks.	
	Oct. 17	36, 56
	Oct. 18	72
	Oct. 20	74
	Oct. 21	87, 92
	Oct. 22	94
10-V	Descending spiral upwind of Keystone stacks.	
	Oct. 16	27
11-V	Ascending spiral abeam the stacks at Keystone.	
	Oct. 22	103
12-V	Descending spiral 10 miles downwind of Keystone stacks.	
	Oct. 16	35
	Oct. 22	106
13-V	Ascending spiral 10 miles downwind of Keystone stacks.	
	Oct. 15	12
	Oct. 17	53
	Oct. 18	71
	Oct. 22	105
14-V	Ascending spiral sounding over Conemaugh stacks.	
	Oct. 16	26
	Oct. 20	85

Code #		
15-V	Descending spiral over Homer City.	
	Oct. 16	23
	Oct. 21	88
16-V	Ascending spiral over Homer City.	
	Oct. 20	83
17-V	Straight ascending sounding from Keystone to Homer City.	
	Oct. 17	54
18-H	Particle collecting pass through a puff of Keystone effluent.	
	Oct. 16	29
19-H	Zip-zip through a knee of Keystone plume.	
	Oct. 17	63, 64
20-H	Terrain-following run from Homer City to Conemaugh.	
	Oct. 22	107
21-H	Through pollution over Johnstown.	
	Oct. 22	108
22-H	Ten-mile downwind run toward Conemaugh stacks.	
	Oct. 16	25
23-H	Background at 5000 feet (MSL).	
	Oct. 17	65
	Oct. 22	104
24-H	Background at 6000 feet (MSL).	
	Oct. 17	66
25-H	Background near Keystone.	
	Oct. 16	24

Code #		
26-H	Downwind run from Conemaugh over New Florence.	
	Oct. 17	55
27-H	Straight and level sounding downwind from Homer City stacks.	
	Oct. 20	84
28-H	Ten-mile terrain-following run downwind of Conemaugh stacks.	
	Oct. 20	86
29-H	Straight and level background sounding from Indiana to Homer City.	
	Oct. 21	93
30-H	In plume over lidar.	
	Oct. 22	109, 110

APPENDIX C

STATISTICAL SUMMARY OF MRI AIRCRAFT ALTITUDE AND TURBULENCE DATA

	Sequence Number	Mean Altitude (ft MSL)	Standard Deviation of Altitude (ft)	Mean Ambient Epsilon (cm^2sec^{-3})	Standard Deviation of Ambient Epsilon (cm^2sec^{-3})	Relative Intensity of Ambient Epsilon (*)	Mean In-Plume Epsilon (cm^2sec^{-3})	Standard Deviation of In-Plume Epsilon (cm^2sec^{-3})	Relative Intensity of In-Plume Epsilon (*)
15 Oct. '68	1	2696	9.3	13.4	7.7	0.6	154.3	128.9	0.8
1225-1426				14.9	8.7	0.6			-
EDT	2	2302	3.9	45.1	29.3	0.7	126.5	155.5	1.2
				9.6	3.6	0.4			-
	3	2872	3.9	15.7	8.8	0.6	31.2	18.7	0.6
				13.6	10.7	0.8			-
	4	3392	4.7			-	18.3	10.2	0.6
	5	3343	5.2	8.1	3.8	0.5	13.5	11.3	0.8
	6	3373	4.0	1.5	1.6	1.1	16.1	10.7	0.7
	7	2697	4.9	30.9	6.2	0.2	35.3	31.0	0.9
				16.0	12.8	0.8			-
	8	2415	6.6	23.9	17.3	0.7	25.6	17.9	0.7
				30.2	35.1	1.2			-
	9	2671	6.4	44.5	40.5	0.9	35.2	33.6	1.0
	10	2493	9.4	32.4	18.8	0.6	36.7	42.7	1.2
				38.7	20.5	0.5			-
	11	1549	5.5	2.6	1.5	0.6	58.1	46.5	0.8
				32.8	25.3	0.8			-
	12	2919	24.7	23.8	13.1	0.6	51.0	45.4	0.9
16 Oct. '68	13	2400	7.4			-	9.2	9.4	1.0
0857-1351	14	2253	8.9	2.3	1.7	0.7	10.9	10.5	1.0
EDT				8.2	7.1	0.9			-
	15	2334	4.1	0.9	0.8	0.9	15.7	13.5	0.9
				0.9	0.7	0.8			-
	16	2331	4.2	0.8	0.4	0.6	13.1	10.8	0.8
				0.2	0.08	0.4			-
	17	2334	5.8	11.4	13.1	1.2	30.8	24.8	0.8
	18	2397	5.0			-	13.1	13.0	1.0
				5.1	6.1	1.2			-

(*) Dimensionless

	Sequence Number	Mean Altitude (ft MSL)	Standard Deviation of Altitude (ft)	Mean Ambient Epsilon ($cm^2 sec^{-3}$)	Standard Deviation of Ambient Epsilon ($cm^2 sec^{-3}$)	Relative Intensity of Ambient Epsilon (*)	Mean In-Plume Epsilon ($cm^2 sec^{-3}$)	Standard Deviation of In-Plume Epsilon ($cm^2 sec^{-3}$)	Relative Intensity of In-Plume Epsilon (*)
	19	2375	6.6	0.2	0.1	0.7	29.0	42.2	1.5
				0.9	1.8	2.0			-
	20	2420	17.6	0.1	0.08	0.8	8.5	8.9	1.0
				0.2	0.4	2.2			-
	21	2273	21.4	0.3	0.3	0.9	8.8	6.0	0.7
				9.8	18.6	1.9			-
	22	2106	17.3	0.1	0	0	10.8	15.8	1.5
	23	2410	25.1	47.0	43.9	0.9			-
	24	2356	17.4	34.2	40.1	1.2			-
	25	2537	9.6	41.9	43.1	1.0			-
	26	2659	25.7	26.2	23.0	0.9			-
	27	3210	32.6	16.4	21.3	1.3			-
	28	3139	5.4	9.6	9.1	0.9	20.2	13.0	0.6
				14.8	13.4	0.9			-
	29	4921	7.3	1.1	2.0	1.8	8.1	7.0	0.9
				0.2	0.2	0.9			-
	30	3349	6.6	3.9	5.6	1.4	10.2	7.7	0.8
				14.2	7.3	0.5			-
	31	3929	6.3	3.1	2.8	0.9	6.6	10.0	1.5
				9.2	16.9	1.8			-
	32	3559	6.2	7.3	5.3	0.7	42.0	47.2	1.1
				22.6	18.2	0.8			-
	33	1850	30.8	0.0	0	0			
	34	900	0	0.0	0	0			
	35	5000	27.4	0.0	0	0			
17 Oct.'68	36	3244	32.3	1.5	2.8	1.8			-
0832-1026	37	2797	4.7	0.1	0.05	0.5	20.4	18.0	0.9
EDT				0.1	0	0			-
	38	2853	4.9	0.2	0.1	0.7	7.1	5.4	0.8
				0.1	0.05	0.5			-

(*) Dimensionless

	Sequence Number	Mean Altitude (ft MSL)	Standard Deviation of Altitude (ft)	Mean Ambient Epsilon ($cm^2 sec^{-3}$)	Standard Deviation of Ambient Epsilon ($cm^2 sec^{-3}$)	Relative Intensity of Ambient Epsilon (*)	Mean In-Plume Epsilon ($cm^2 sec^{-3}$)	Standard Deviation of In-Plume Epsilon ($cm^2 sec^{-3}$)	Relative Intensity of In-Plume Epsilon (*)
	61	900	0	0.1	0	0			-
	62	900	0	0.1	0	0			-
	63	900	0	0.1	0	0			-
	64	900	0	0.1	0	0			-
	65	900	0	0.1	0	0			-
	66	900	0	0.1	0	0			-
18 Oct. '68	67	900	0	0.1	0	0			-
0842-1044	68	900	0	0.1	0	0			-
EDT	69	900	0	0.1	0	0			-
	70	900	0	0.1	0	0			-
	71	3775	50.2	0.1	0	0			-
1134-1245	72	2425	34.3	0.1	0	0			-
EDT	73	900	0	0.1	0	0			-
20 Oct. '68	74	3117	31.7	2.3	5.8	2.5			
0900-1114	75	2309	4.5			-	2.7	4.6	1.7
EDT				0.7	2.5	3.6			-
	76	2300	0			-	2.0	2.6	1.3
				0.1	0	0			-
	77	2332	4.1	0.1	0	0	4.7	5.7	1.2
	78	2328	3.5	0.1	0	0	4.3	5.0	1.2
				0.1	0	0			-
	79	2246	2.8	0.3	0.2	0.7	11.9	14.8	1.2
				0.1	0	0			-
	80	1674	10.1			-	47.5	40.5	0.9
	81	1451	7.8			-	26.7	41.9	1.6
				0.6	0.5	0.9			-
	82	1678	7.8	9.9	2.1	0.2	114.2	92.8	0.8
	83	3016	33.1	9.9	23.4	2.4			-
	84	2425	9.3	49.0	65.8	1.3			-
	85	2986	33.3	5.8	17.3	3.0			-

*Dimensionless

	Sequence Number	Mean Altitude (ft MSL)	Standard Deviation of Altitude (ft)	Mean Ambient Epsilon ($cm^2 sec^{-3}$)	Standard Deviation of Ambient Epsilon ($cm^2 sec^{-3}$)	Relative Intensity of Ambient Epsilon (*)	Mean In-Plume Epsilon ($cm^2 sec^{-3}$)	Standard Deviation of In-Plume Epsilon ($cm^2 sec^{-3}$)	Relative Intensity of In-Plume Epsilon (*)
	39	2628	4.6	0.1	0.06	0.6	13.0	11.9	0.9
				0.3	0.1	0.3			-
	40	2717	3.0	8.3	10.0	1.2	6.5	7.7	1.2
				0.1	0	0			-
	41	2916	4.1			-	2.9	3.3	1.1
	42	2649	4.6	0.1	0	0	8.7	6.1	0.7
	43	2733	4.7	1.3	0	0	1.1	0.9	0.9
	44	2621	4.1			-	1.4	0.9	0.7
				0.3	0.3	1.0			
	45	3542	4.1			-	2.6	4.3	1.6
				0.2	0.3	1.6			
	46	2651	5.7			-	1.5	1.5	1.0
				0.6	0.9	1.5			
	47	2848	5.4	0.1	0	0	0.4	0.3	0.8
				0.1	0.06	0.6			-
	48	2758	5.7	1.2	0.5	0.5	4.0	2.9	0.7
	49	2816	5.7			-	0.3	0.4	1.5
				1.0	0.9	0.9			
	50	2744	4.4	0.1	0.08	0.8	1.3	2.0	1.5
	51	2643	2.8			-	2.5	6.0	2.4
	52	2560	8.7	1.8	3.1	1.7	29.3	34.11	1.2
	53	3385	32.2	24.9	59.3	2.4			-
17 Oct. '68	54	3308	32.3	18.8	38.9	2.1			-
1057-1326	55	2598	7.2	59.9	42.8	0.7			-
EDT	56	3317	32.2	20.3	33.6	1.7			-
	57	3485	5.5			-	39.1	61.1	1.6
	58	1974	6.7			-	65.4	57.0	0.9
	59	3218	10.4	39.0	15.5	0.4	37.8	40.4	1.1
	60	900	0	0.1	0	0			-

(*) Dimensionless

	Sequence Number	Mean Altitude (ft MSL)	Standard Deviation of Altitude (ft)	Mean Ambient Epsilon (cm^2sec^{-3})	Standard Deviation of Ambient Epsilon (cm^2sec^{-3})	Relative Intensity of Ambient Epsilon (*)	Mean In-Plume Epsilon (cm^2sec^{-3})	Standard Deviation of In-Plume Epsilon (cm^2sec^{-3})	Relative Intensity of In-Plume Epsilon (*)
	86	2521	14.3	41.5	52.7	1.3			-
21 Oct.'68	87	3342	32.2	1.3	4.5	3.5			-
0825-0951	88	3214	32.0	4.1	12.0	2.9			-
EDT	89	2826	2.6			-	2.5	2.3	0.9
				0.1	0	0			-
	90	2748	5.4	0.1	0	0	1.8	1.8	1.0
				0.2	0	0			-
	91	2914	3.0			-	4.5	4.7	1.0
				0.3	0.2	0.7			-
1033-1114	92	3246	32.1	9.6	24.9	2.3			-
EDT	93	2733	3.5	35.6	42.3	1.2			-
22 Oct.'68	94	2668	27.1	0.2	0.6	3.2			-
0907-1132	95	2585	9.8			-	0.2	0.4	2.2
EDT	96	2620	6.2			-	0.07	0.1	2.0
	97	2604	6.1	0.02	0	0	0.3	0.4	1.5
				0.02	0	0			
	98	2562	4.0			-	0.3	0.8	2.8
	99	2600	0			-	0.04	0.1	2.5
				0.03	0	0			-
	100	1946	6.6			-	1.2	1.3	1.1
				0.3	0.3	1.0			-
	101	2300	0	0.3	0.2	0.7	0.02	0	0
				0.01	0	0			-
	102	2548	5.2	0.01	0	0	0.02	0	0
				0.004	0	0			-
	103	3688	30.9	0.04	0.08	2.0			-
	104	5193	11.4	0.02	0.03	1.5			-
	105	3628	31.2	0.3	1.9	6.2			-
	106	2813	30.0			-	8.3	22.8	2.8
	107	2344	20.6	17.5	21.9	1.3			
	108	2213	5.3	17.3	37.3	2.2			
1213-1214	109	2857	8.1	54.7	37.6	0.7	23.4	24.4	1.0
EDT	110	2350	0			-	65.5	34.0	0.5

*Dimensionless